Alternatives to Steel Grid Decks—Phase II

Final Report

FDOT Contract No. BDK80 977-06

Amir Mirmiran , Muhammad Azhar Saleem, Pedram Zohrevand
Department of Civil and Environmental Engineering
Florida International University
Miami. Florida

Kevin Mackie, Jun Xia, Yulin Xiao
Department of Civil and Environmental Engineering
University of Central Florida
Orlando, Florida

Submitted to:

Mr. Sam Fallaha
Project Manager
Florida Department of Transportation
Research Center

September 30, 2012

DISCLAIMER

APPROXIMATE CONVERSIONS TO SI UNITS

SYMBOL	WHEN YOU KNOW	MULTIPLY BY	TO FIND	SYMBOL
LENGTH				
in	inches	25.4	millimeters	mm
ft	feet	0.305	meters	m
yd	yards	0.914	meters	m
mi	miles	1.61	kilometers	km

SYMBOL	WHEN YOU KNOW	MULTIPLY BY	TO FIND	SYMBOL
AREA				
in^2	square inches	645.2	square millimeters	mm^2
ft^2	square feet	0.093	square meters	m^2
yd^2	square yard	0.836	square meters	m^2
ac	acres	0.405	hectares	ha
mi^2	square miles	2.59	square kilometers	km^2

SYMBOL	WHEN YOU KNOW	MULTIPLY BY	TO FIND	SYMBOL
VOLUME				
fl oz	fluid ounces	29.57	milliliters	mL
gal	gallons	3.785	liters	L
ft^3	cubic feet	0.028	cubic meters	m^3
yd^3	cubic yards	0.765	cubic meters	m^3
NOTE: volumes greater than 1000 L shall be shown in m^3				

SYMBOL	WHEN YOU KNOW	MULTIPLY BY	TO FIND	SYMBOL
MASS				
oz	ounces	28.35	grams	g
lb	pounds	0.454	kilograms	kg
T	short tons (2000 lb)	0.907	mega grams (or "metric ton")	Mg (or "t")

SYMBOL	WHEN YOU KNOW	MULTIPLY BY	TO FIND	SYMBOL
TEMPERATURE (exact degrees)				
^{o}F	Fahrenheit	5 (F-32)/9 or (F-32)/1.8	Celsius	^{o}C
SYMBOL	**WHEN YOU KNOW**	**MULTIPLY BY**	**TO FIND**	**SYMBOL**
ILLUMINATION				
fc	foot-candles	10.76	lux	lx
fl	foot-Lamberts	3.426	candela/m^2	cd/m^2

SYMBOL	WHEN YOU KNOW	MULTIPLY BY	TO FIND	SYMBOL
FORCE and PRESSURE or STRESS				
lbf	pound force	4.45	newtons	N
kipf	kip force	4448.22	newtons	N
lbf/in^2	poundforce per square inch	6.89	kilopascals	kPa
kipf/ft^2	kip force per square foot	47.88	kilopascals	kPa
kipf/in^2	kip force per square inch	6,894.76	kilopascals	kPa

APPROXIMATE CONVERSIONS TO SI UNITS

SYMBOL	WHEN YOU KNOW	MULTIPLY BY	TO FIND	SYMBOL
LENGTH				
mm	millimeters	0.039	inches	in
m	meters	3.28	feet	ft
m	meters	1.09	yards	yd
km	kilometers	0.621	miles	mi

SYMBOL	WHEN YOU KNOW	MULTIPLY BY	TO FIND	SYMBOL
AREA				
mm^2	square millimeters	0.0016	square inches	in^2
m^2	square meters	10.764	square feet	ft^2
m^2	square meters	1.195	square yards	yd^2
ha	hectares	2.47	acres	ac
km^2	square kilometers	0.386	square miles	mi^2

SYMBOL	WHEN YOU KNOW	MULTIPLY BY	TO FIND	SYMBOL
VOLUME				
mL	milliliters	0.034	fluid ounces	fl oz
L	liters	0.264	gallons	gal
m^3	cubic meters	35.314	cubic feet	ft^3
m^3	cubic meters	1.307	cubic yards	yd^3

SYMBOL	WHEN YOU KNOW	MULTIPLY BY	TO FIND	SYMBOL
MASS				
g	grams	0.035	ounces	oz
kg	kilograms	2.202	pounds	lb
Mg (or "t")	mega grams (or "metric	1.103	short tons (2000	T

	ton")		lb)	

SYMBOL	WHEN YOU KNOW	MULTIPLY BY	TO FIND	SYMBOL
TEMPERATURE (exact degrees)				
°C	Celsius	1.8C+32	Fahrenheit	°F

SYMBOL	WHEN YOU KNOW	MULTIPLY BY	TO FIND	SYMBOL
ILLUMINATION				
lx	lux	0.0929	foot-candles	fc
cd/m^2	candela/m^2	0.2919	foot-Lamberts	fl

SYMBOL	WHEN YOU KNOW	MULTIPLY BY	TO FIND	SYMBOL
FORCE and PRESSURE or STRESS				
N	newtons	0.225	pound force	lbf
kPa	kilopascals	0.145	pound force per square inch	lbf/in^2

Technical Report Documentation Page

1. Report No.	2. Government Accession No.	3. Recipient's Catalog No.

4. Title and Subtitle **Alternatives to Steel Grid Decks—Phase II**	5. Report Date September 30, 2012
	6. Performing Organization Code
7. Author(s) **Amir Mirmiran, Kevin Mackie, Muhammad Azhar Saleem, Jun Xia, Pedram Zohrevand, and Yulin Xiao**	8. Performing Organization Report No.
9. Performing Organization Name and Address FIU, Department of Civil Engineering, 10555 W. Flagler Street, EC 3600, Miami, FL 33174 UCF, Department of Civil and Environmental Engineering, 402 Engineering Building 2, Orlando, FL 32816	10. Work Unit No. (TRAIS)
	11. Contract or Grant No. BDK80 977-06
12. Sponsoring Agency Name and Address The Florida Department of Transportation Research Center 605 Suwannee Street, MS 30 Tallahassee, FL 32399	13. Type of Report and Period Covered Draft Final December 2009 – September 2012
	14. Sponsoring Agency Code

15. Supplementary Notes

16. Abstract

The primary objective of this research project was to investigate alternatives to open grid steel decks. Three alternative deck systems, including aluminum deck, ultra-high performance concrete (UHPC)-high-strength steel (HSS) deck, and UHPC-fiber-reinforced polymer (FRP) tube deck, were developed and studied in the first phase of this research project. The UHPC-HSS deck showed a great potential to serve as a viable alternative. However, more studies were needed on its components and system design before it was deemed ready to be implemented. Accordingly, this phase of the project covered all the studies needed for the design and implementation of the UHPC-HSS deck system. Also, suitability of an FRP bridge deck system as an alternative to open grid steel decks was evaluated.

The UHPC-HSS deck was experimentally investigated at both the component and system levels. Studies included the deck-to-girder connection test for shear and uplift forces, deck-to-deck connection test, multi-unit specimen tests to determine the lateral distribution of live loads, full-scale test for fatigue loading and residual strength, and pullout and beam tests to evaluate the development length. The deck-to-girder and the deck-to-deck connections both proved to be adequate for the loading conditions expected from the HS20 truck and wind forces. Tests for the live load distribution showed that most of the load is taken by the ribs under or immediately next to the load. The deck panels and connections successfully endured two million cycles of repeated loading and had a residual strength beyond their target design load. It was shown that the development length of HSS rebars in UHPC can be reasonably predicted by ACI 408R-03.

The dowel action of longitudinal steel reinforcement in UHPC and the uniaxial fatigue behavior of UHPC specimens were also evaluated through both experimental and analytical studies. It was shown that the dowel action would contribute considerably to the shear resistance in reinforced UHPC structures.

In another part of this research, an FRP deck system was tested under static and fatigue loading. The FRP deck withstood two million cycles of AASHTO-specified repeated loading with no sign of damage or failure, while its deflection under service load significantly exceeded the deflection limit suggested by AASHTO LRFD.

17. Key Word Movable Bridges, Lightweight Decks, Ultra-high Performance Concrete, FRP	18. Distribution Statement Document is available to the US public through, The NTIS, Springfield, VA 22161

19. Security Classif. (of this report) Unclassified	20. Security Classif. (of this page) Unclassified	21. No. of Pages	22. Price

Technical Report Documentation Page Form DOT F 1700.7 (8-72) Reproduction of completed page authorized

ACKNOWLEDGEMENTS

The authors would like to thank Florida Department of Transportation (FDOT) Structures Lab in Tallahassee and the FDOT State Materials Office in Gainesville for their diligent support in fatigue testing and the materials testing. Special thanks are also due to the Project Manager, Mr. Sam Fallaha, for his continued support and technical contributions to the project.

The authors would also like to take this opportunity and recognize the Late Mr. Marc Ansley, the initial Project Manager on this project.

Finally, the authors would like to acknowledge MMFX Technologies of Irvine, CA, and Lafarge North America for providing materials for this project, and the Structural Composites Inc. of Melbourne, FL, for providing the FRP bridge deck for testing.

EXECUTIVE SUMMARY

Florida has the largest inventory of movable bridges in the U.S., with a total of 152, of which 91% are bascule, 7% swing, and 2% lift bridges. Most of the movable bridges use open grid steel decks, which are typically supported by steel stringers with 4-ft spacing. On average, these decks weigh less than 25 lb/ft^2. Poor skid resistance and rideability, costly maintenance, and high noise levels and vibrations are the main disadvantages of open grid steel decks.

The primary objective of this research project was to investigate alternatives to the open grid steel decks. These alternatives must have a solid riding surface with good rideability, weigh less than 25 lb/ft^2, meet AASHTO load requirements, and have low noise levels. Three alternative deck systems, including aluminum deck, ultra-high performance concrete (UHPC)-high-strength steel (HSS) deck, and UHPC-fiber-reinforced polymer (FRP) tube deck, were developed and studied in the first phase of this research project. The aluminum deck was shown to be a feasible alternative to open grid steel deck and ready for implementation. The UHPC-HSS deck showed a great potential to serve as a viable alternative. However, more studies were needed on its components and system design before it would be ready for implementation. Preliminary experimental studies on the third system, UHPC-FRP tube deck, indicated that more studies would be required to improve its design. Based on the results achieved from the first phase of this project, the second phase was conducted to cover all the studies needed for the design and implementation of the UHPC-HSS deck system and to evaluate an all-FRP bridge deck system as an alternative to open grid steel decks.

The UHPC-HSS deck was experimentally investigated at both the component and system levels. Studies included the deck-to-girder connection test for shear and uplift forces, deck-to-deck connection test, multi-unit specimen tests to determine the lateral distribution of live loads, and full-scale test for fatigue loading and residual strength. The loadings were based on AASHTO Load and Resistance Factor Design, LRFD, (LRFD; AASHTO 2005). The deck-to-girder and the deck-to-deck connections both proved to be adequate for the loading conditions expected from the HS20 truck and wind forces. Tests for the live load distribution showed that most of the load is taken by the ribs under or immediately next to the load. The deck panels and connections successfully endured two million cycles of repeated loading and had a residual strength beyond their target design load.

Since the UHPC bridge deck has been developed with #3 and #7 rebars, the development length of these two rebars in UHPC was evaluated using both pullout and beam tests. It was shown that the development lengths calculated based on the equations provided by the ACI 408R-03 agree reasonably well with the experimental results.

The dowel action of longitudinal steel reinforcement in UHPC and the uniaxial fatigue behavior of UHPC specimens were also evaluated through both experimental and analytical studies. It was shown that the dowel action contributes considerably to the shear resistance of reinforced UHPC members.

In another part of this research, an FRP deck product made by Structural Composites Inc. of Melbourne, FL, was tested under static and fatigue loading. The FRP deck withstood two million cycles of AASHTO-specified repeated loading with no sign of damage or failure, and its residual strength reached three times the target design load. However, the deflection of this FRP deck under service load significantly exceeded the deflection limit suggested by AASHTO LRFD.

TABLE OF CONTENTS

LIST OF TABLES

LIST OF FIGURES

Chapter-1

Introduction

1.1 Problem Statement

According to the most recent national bridge inventory in 2008, Florida has the largest inventory of movable bridges, with a total of 152, of which 91% are bascule, 7% swing and 2% lift bridges. Over 50% of the movable bridges in Florida are located in the Miami and Fort Lauderdale areas along the Intracoastal Waterway (FHWA 2008). Most of the movable bridges use open grid steel decks (Figure 1.1), which are typically supported by steel stringers with 4 ft spacing. On average, these decks weigh less than 25 lb/ft^2, while some can weigh as little as 14 lb/ft^2.

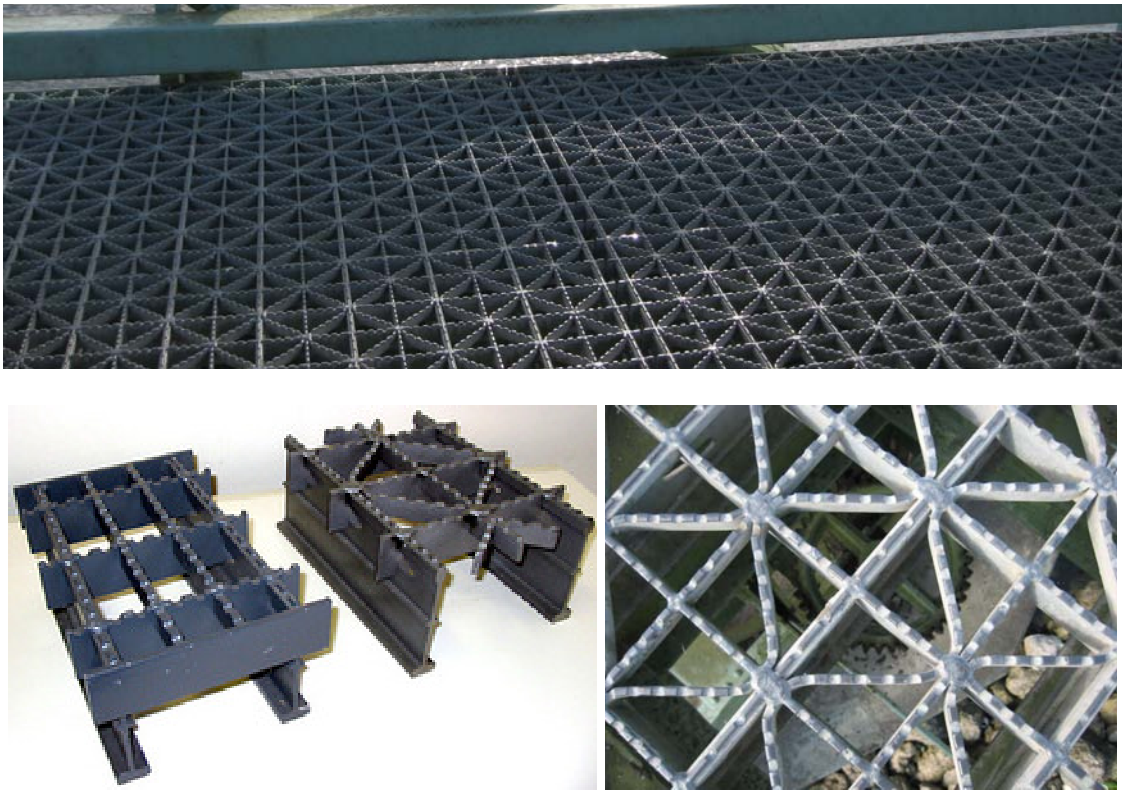

Figure 1.1 Open Steel Grating for Bridge Decks

Movable bridges are mostly made of open grid steel decks, which suffer from poor skid resistance and rideability; costly maintenance; and high noise levels and vibrations. As these bridge decks polish over time, their skid resistance may deteriorate to unacceptable levels, which, without an active maintenance, may lead to poor rideability. Noise is another potential concern in some urban areas. Baseline acoustic testing by Florida Atlantic University (Takkasila and Reddy 1996) measured noise levels radiating from these bridge decks at levels that may cause public concern.

For these reasons related to safety and environmental quality, research is needed into alternatives for open grid steel deck systems that could address the rideability concerns while meeting the strict weight limits on these types of bridges. Accordingly, three alternative deck systems with solid riding surface and a weight less than 25 lb/ft^2 were developed and studied in the first phase of this research project (Mirmiran et al. 2009). The three deck systems included SAPA aluminum deck by SAPA Group of Sweden, ultra-high performance concrete (UHPC)-high-strength steel (HSS) deck, and UHPC-fiber-reinforced polymer (FRP) tube deck. A detailed experimental and analytical evaluation of the system indicated that SAPA aluminum deck is a feasible alternative to open grid steel deck and ready for implementation. UHPC-HSS deck is the second alternative system developed as a part of the first phase of this project. Comprehensive experimental and analytical studies on the system were carried out to establish its suitability. The results showed that the UHPC-HSS deck has a great potential to serve as an alternative system. However, further studies are needed on the components and system design of the UHPC-HSS deck before it is ready to be implemented. UHPC-FRP tube deck was the third system that was studied in the first phase. Preliminary experimental studies on this system showed its potential as an alternative to conventional open steel grid decks, while more studies are required to improve its design.

This second phase of the project covers all the studies needed for the design and implementation of the UHPC-HSS deck system as well as the evaluation of an FRP bridge deck system as an alternative to open grid steel decks.

1.2 Research Objectives

The primary objective of this research project is to investigate UHPC and FRP alternatives to the open grid steel decks. To be viable alternatives, these systems must possess the following attributes:

1. Solid riding surface with good rideability;
2. Weigh less than 25 lb/ft^2;
3. Meet AASHTO load requirements;
4. Have low noise levels; and
5. Low profile (approximately 5 in. depth).

This second phase of the project focuses on practical implementation issues and materials and system characterization of UHPC deck system proposed in the first phase. The evaluation of a new FRP deck system as an alternative to open grid steel decks is another focus of this research.

1.3 Research Approach

Two deck systems were considered in this study:

1. Ultra-high Performance Concrete (UHPC) Deck
2. Fiber-Reinforced Polymer (FRP) Deck made by Structural Composites Inc. of Melbourne, FL

Experimentation included flexural tests, both static and dynamic, on the above two deck systems to establish their suitability for movable bridges. Some ancillary tests on the connections of UHPC deck were also performed. Analytical modeling of dowel action phenomenon and uniaxial fatigue testing on UHPC specimens was also performed.

1.4 Report Organization

This report is comprised of five chapters. This first chapter serves as an introduction, mainly describing the problem statement, research objectives, and research approach. Chapter 2 covers the experimental work related to UHPC deck, including component and system level testing, and testing for the estimation of development length of high-strength steel embedded in UHPC. Chapter 3 focuses on dowel action phenomenon and uniaxial fatigue tests on UHPC specimens. Chapter 4 describes the static and fatigue testing of the FRP deck made by Structural Composites Inc. Chapter 5 provides summary and conclusions for the project, as well as recommendations for future research.

Chapter-2

Ultra-High Performance Concrete Deck

2.1 Introduction

Ultra-high Performance Concrete (UHPC) is a relatively new structural material composed of a high-strength cementitious matrix and steel fibers (Habel et al. 2007), with much higher durability and strength than other cementitious materials (Habel et al. 2006 and Graybeal 2007a). UHPC has around 4 – 8 times higher compressive strength than conventional concrete, and its tensile strength ranges from 0.9 to 1.7 ksi (Graybeal and Hartmann 2003). The interaction of steel fibers at the microscopic level and their ability to sustain load after the onset of cracking are the major contributing factors to the high tensile strength of UHPC (Perry 2003 and Harris and Roberts-Wollmann 2005). Curing of UHPC by submerging it in 194ºF water for 48 hours considerably increases its compressive strength and modulus of elasticity, and almost eliminates its long-term shrinkage (Graybeal 2006). UHPC also attains high flexural strengths ranging from 5.0 to 7.2 ksi based on standard flexural beam tests (Perry and Zakariasen 2003). In Australia, Japan, New Zealand, South Korea, Europe and the U.S., UHPC has been used for both vehicular and pedestrian bridges (Graybeal 2006, Blais and Couture 1999, and Hajar et al. 2003). Although a number of UHPC bridge decks have been developed (Graybeal 2007b, Perry 2007, and Toutlemonde et al. 2007), they are not suitable for replacing the existing movable bridges due to their higher self-weights.

A lightweight, low profile UHPC deck system reinforced with high-strength steel (HSS) has been proposed as an alternative to open grid steel deck (Saleem et al. 2011). The system consists of a thin slab with primary ribs spanning between girders, and shallow secondary ribs connecting the primary ribs parallel to the direction of traffic. Figure 2.1 shows the schematics of a single unit of the proposed deck, which weighs about 25 lb/ft^2. The deck is designed as an alternative to open grid steel decks typically spanning a girder spacing of 4 ft. The UHPC material, used in this research is composed of cement, silica fumes, ground quartz, sand, super plasticizer and steel fiber (2% by volume). The steel fibers have a diameter of 0.008 in. and a length of 0.5 in. UHPC achieved an average compressive strength of 25.5 ksi in the laboratory without heat curing. The material for entire project was provided by Lafarge North America of Calgary, Canada, The primary ribs of the deck system were reinforced with one #7 HSS rebar, provided by MMFX Technologies of Irvine, CA.

This section presents the experimental results for the deck-to-girder connections and deck-to-deck connections; lateral distribution of live load; large-scale repeated load and residual strength of the deck; and pullout and beam tests for determination of development length.

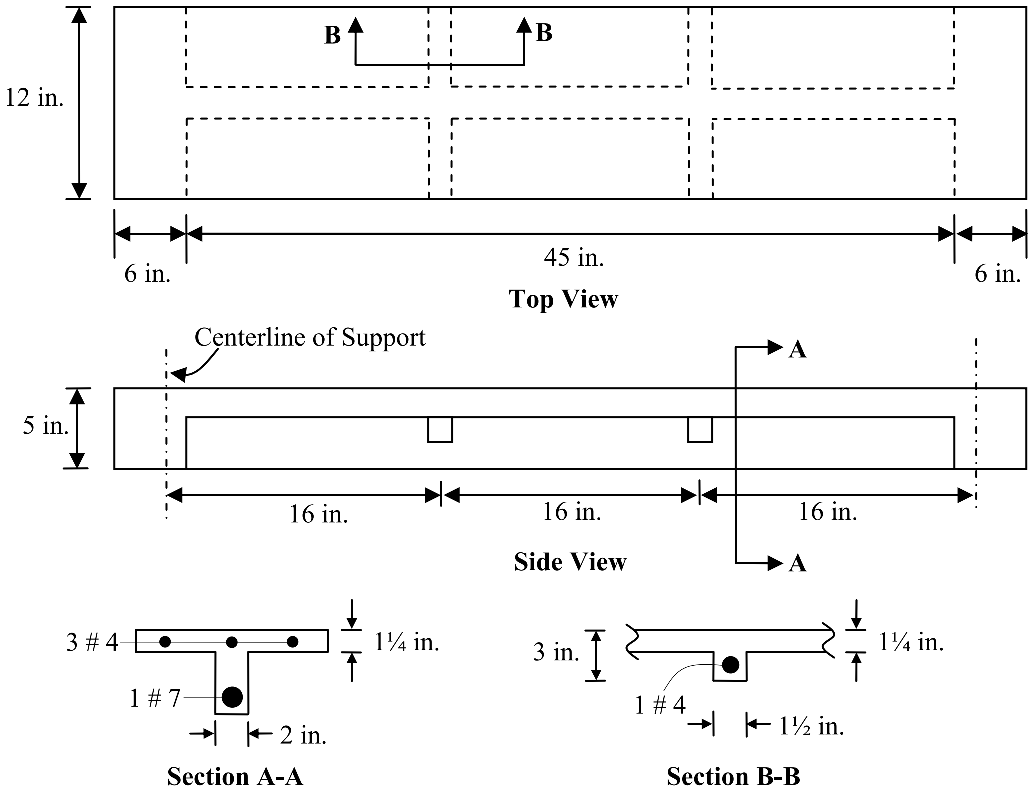

Note: 1 in. = 25.4 mm

Figure 2.1 Schematics of Single Unit Deck Panel

2.2 Experimental Work and Discussion – Part 1

The primary objective of this part of the experimental work was to investigate the long-term performance of the proposed UHPC bridge deck system. Before testing the full-scale specimen, it was imperative to establish the individual strengths of deck-to-deck and deck-to-girder connection and their modes of failure as well. In addition to this, the lateral distribution of live load was also determined as a secondary objective. To achieve these objectives a test matrix was developed which is presented in Table 2.1 Loading followed AASHTO (2005) recommendations, using a prescribed footprint of HS20 truck dual-tire wheel (10 x 20. in), with a 1 in. thick neoprene pad under the steel plate. Strain gauges, string potentiometers, and displacement transducers were installed at strategic locations to obtain strain and deflection data, using a data acquisition system with a sampling frequency of 1 Hz. The target live load for the large scale test was 37.24 kip (16 kip x 1.75 x 1.33), including the load factor of 1.75 and the dynamic impact factor of 1.33, based on the AASHTO (2005) recommendations. It should be noted that AASHTO (2005) allows to ignore the lane loading for the design of decks spanning in the direction perpendicular to traffic, therefore the target load is only based on wheel load (16 kip) of an HS20 truck.

Table 2.1 Specimen Test Matrix – Part 1

Serial No.	Description of Test
1	Deck-to-Girder Connection
	- Shear Test
	- Uplift Test
2	Deck-to-Deck Connection
3	Lateral Distribution of Load
	Simple-span specimen with four ribs (4T1S)
	Simple-span specimen with five ribs (5T1S)
	Two-span specimen with four ribs (4T2S)
4	Large Scale Specimen
	- Fatigue Test
	- Residual Strength Test

2.2.1 Shear Test of Deck-to-Girder Connections

The objective of this test was to establish the lower-bound capacity of the deck-to-girder connection against horizontal shear produced due to the braking force of an HS20 truck and horizontal component of the wind load on the superstructure of a bridge. In the case of an interior deck panel, the braking force will be resisted in two ways, first by the deck-to-deck connection that will transfer the force to the adjacent panel, and secondly by the deck-to-girder connection that will transfer the force to the girder. For the last panel on the bridge deck, the braking force will be resisted by the deck-to-girder connections only. Therefore, it was imperative to determine the shear capacity of the deck-to-girder connection alone. The required factored shear force based on the recommendations of AASHTO came out to be 7.8 kip. This connection is composed of a 4 in. long, and ½ in. diameter shear stud welded on top of the girder flange and encased in UHPC. Rectangular opening (2 in wide, 3 in. long and 5 in. deep) was left in each specimen at the time of casting to be filled later with UHPC. Two precast portions of the proposed deck, with a clear spacing of 15 in. were placed on top of the girder flange accommodating the already-welded studs in the openings left for this purpose. Fresh UHPC was then cast to fill the openings in both the specimens. No special treatment was carried out on the old surface of the opening except cleaning it with water to remove any dust. Plastic sheets were placed as bond breakers between the specimens and the girder, to make the most critical condition for the connection. Test was conducted after 28 days of casting the concrete in the connection. A hydraulic jack was placed in the space (15 in.) between the two specimens which simultaneously pushed both of them outwards, subjecting the stud to horizontal shear.

Figure 2.2 shows the test setup, failure pattern, and the load-displacement responses for the shear test. Displacements were measured at the top of both panels using string potentiometers, and the load was measured using a load cell. The ultimate shear strength of the connection was found as 15.3 kip, about twice the factored design shear force, based on AASHTO (2005). The two deck portions exhibited similar behavior until the peak load, after which one of them cracked and displaced more than the other. The photo shows the portion of the deck close to the load rotating about a horizontal axis. The rotation was caused by a big crack starting at the bottom and moving up, all the while growing wider near the bottom. The stud remained intact so as the UHPC around it, which was poured to fill the opening left for the connection. The cold joint between the old and new UHPC caused the crack to remain restricted only in the deck panel. Connection failure of this nature would not be expected in an actual bridge deck because of the confinement provided by the concrete around the connection region and also because the studs present in a line on other girders will resist the shear force, and prevent such rotation. Due to confinement, the shear strength of connection in an actual bridge deck is expected to be much higher than what is exhibited in this test. This test, however, shows that the isolated shear strength of the connection is much higher than the required capacity.

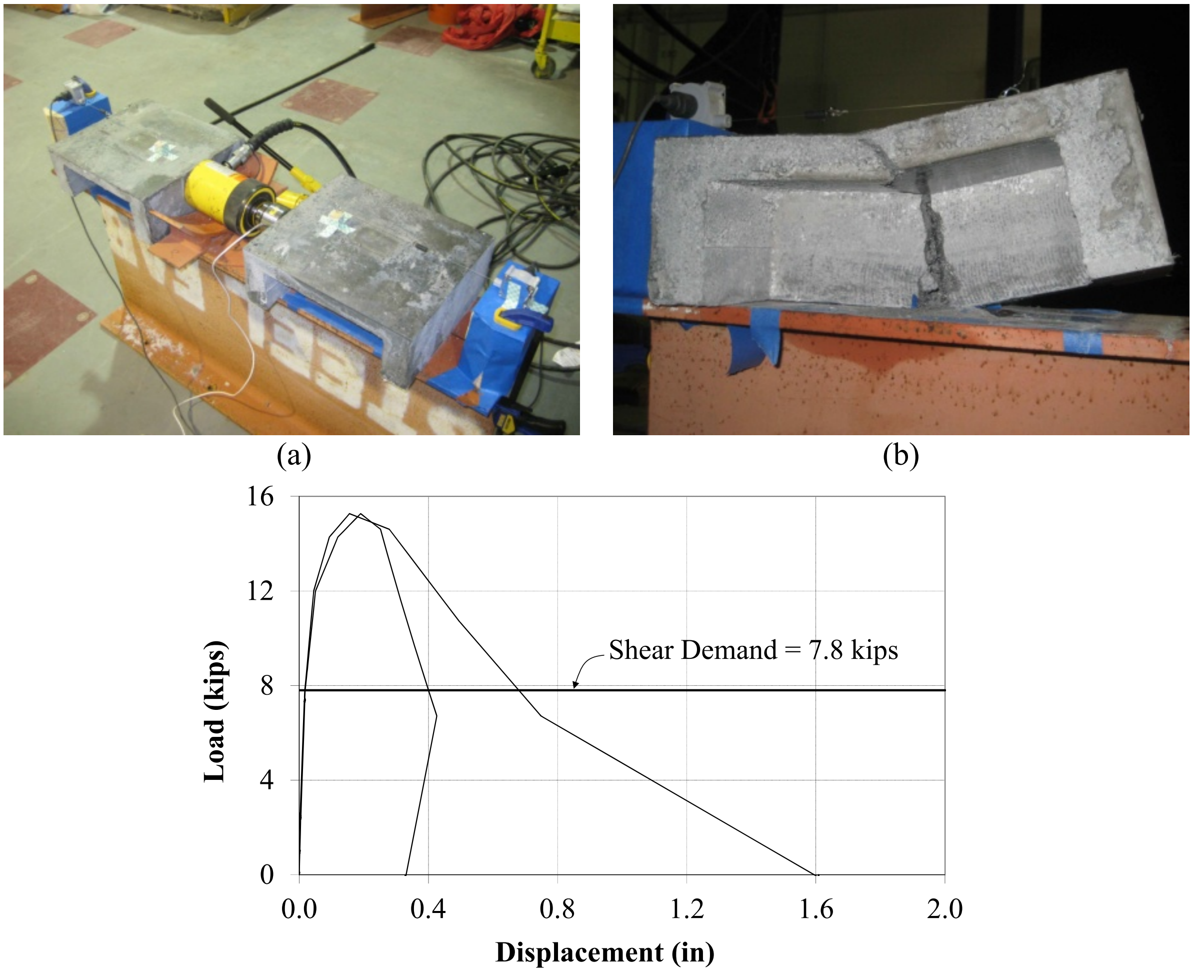

(c)

Figure 2.2 Testing of Deck-to-Girder Connection for Shear: (a) Test Setup; (b) Mode of Failure; and (c) Load-Displacement Responses

2.2.2 Uplift Test of Deck-to-Girder Connections

The uplift test characterizes the resistance of the deck-to-girder connection against uplift wind pressure. As per AASHTO Load and Resistance Factor Design, LRFD, 3.8.2 (2005), an upward wind pressure of 0.02 ksf times the width of the deck shall be applied at the quarter point of the deck width, and this is applied only for the Strength III limit state, which has a load factor of 1.4 for wind load on the super structure of the bridge. For a 50 ft. wide bridge, the service wind pressure comes out to be 1 kip/ft. And the factored wind pressure becomes 1.4 kip/ft. Because the stud is planned to be used at a spacing of 1 ft, therefore the required uplift capacity for the connection becomes 1.4 kip, assuming a worst case when only one stud is present to take this load. The test specimen and connection were of the same size and prepared in the similar way as for the shear test. Upward load was applied using two hydraulic jacks, one on each side of the test specimen. Steel shims were used between the pistons and the specimen to ensure proper contact and to avoid any differential movement. Deflections were measured at two positions, one at the location of the stud and another at the edge of the filled joint. Figure 2.3 shows the test setup, failure mode, and the load-deflection responses. The connection proved to be more than adequate for the uplift, with the peak load of more than 5.7 times the AASHTO (2005) required strength of 1.4 kip. Shear stress at the interface of the old and new concrete at the peak load of 8 kip was 0.16 ksi. Failure occurred along the filled joint, with the deck lifted up while leaving the new UHPC and the stud intact and connected to the girder. To avoid this type of failure in an actual bridge deck, the configuration of the openings in the deck panel could be changed to stepped instead of rectangular. Stepped opening could provide mechanical interlocking, which will also enhance the capacity of the connection. Roughing of the old concrete surface in the opening created to accommodate the stud could also create better bond with the new concrete and further increase the strength of the connection. The load-displacement responses show that the old and new UHPC experienced no relative slip before the failure took place. The post peak behavior of the connection was however brittle as seen from a sudden drop of load to about 60% of the peak load. A stepped connection with rough concrete surface is expected to exhibit more ductile failure than what is experienced in this test. Figure 2.4 presents the comparison between rectangular opening, which was used in the shear and uplift test, and the proposed stepped opening. It was decided to use stepped opening for the large-scale specimen.

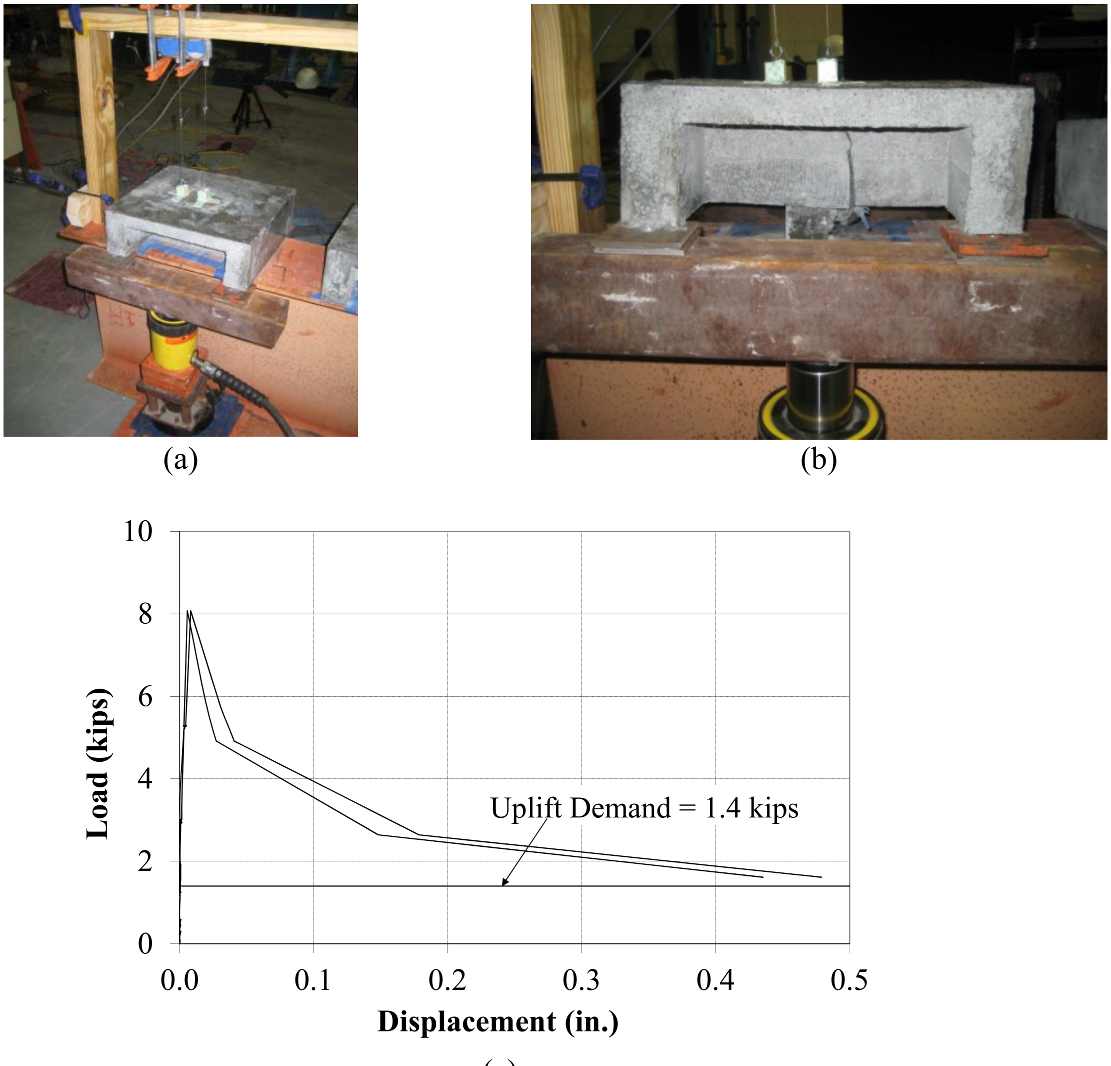

(a) (b)

(c)

Figure 2.3 Testing of Deck-to-Girder Connection for Uplift: (a) Test Setup; (b) Mode of Failure; and (c) Load-Displacement Responses

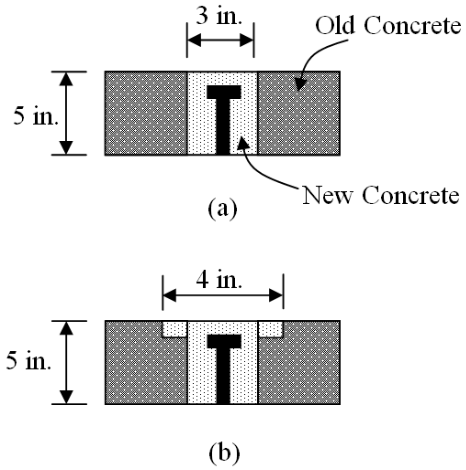

(a)

(b)

Figure 2.4 Deck-to-Girder Connection: (a) Rectangular Opening and (b) Stepped Opening

2.2.3 Deck-to-Deck Connection Test

Deck-to-deck connection is composed of tongue and groove in two adjacent panels. The connection was not a match-cast, however the experience of testing emphasized that need of a match-cast connection. Strength of the deck-to-deck connection is important for the transfer of load between panels, and its failure may lead to excessive deflection and potential delamination of the wear surface. Two simply-supported 4 ft. span panels were loaded along their joint, as the most critical condition. Figure 2.5 shows the test setup, mode of failure, and the load-deflection responses. Four string potentiometers, one under each rib, monitored the deflections. At the service load of 16 kip all four ribs showed linear behavior. As the load progressed, the two ribs near the load area exhibited more nonlinear behavior (D2 and D3 in Fig. 2.5) and shear cracks were developed at 42.5 kip in the rib with the groove which was directly under the load. As the cracks gradually grew wider, the rib with the tongue also began to crack in shear. While the ribs far from load (D1 and D4) showed almost linear behavior until the peak load was reached after which rib 1 exhibited relive in the load, indicating punching around the loading pad. The two edge ribs showed very small shear cracking, approaching the peak load. The test was stopped at about 0.8 in. deflection due to safety concerns. The load-deflection responses show a small relative deflection between the two ribs having the connection (D2 and D3 in Fig. 2.5). The reason could be some human error in the forming of the tongue and groove which results in a small gap between them and they do not engage each other at the initial stage of loading. To avoid this relative deflection, it is recommended to either prepare a match-cast connection or use epoxy grout to connect the tongue and groove while placing the deck panels on the girders. Uniform deflection of ribs at the connection is important not only for comfortable riding but also keeps the wearing surface intact. Otherwise transverse cracks can appear in the wearing surface at the location of joint between two panels. The connection failed at 79 kip, more than twice the target load (37.24 kip). This high strength of the deck-to-deck connection will ensure the development of panel action to effectively distribute the load in the lateral direction. A match-cast connection or connection with epoxy is expected to have higher strength and smaller deflection then what was observed in this test.

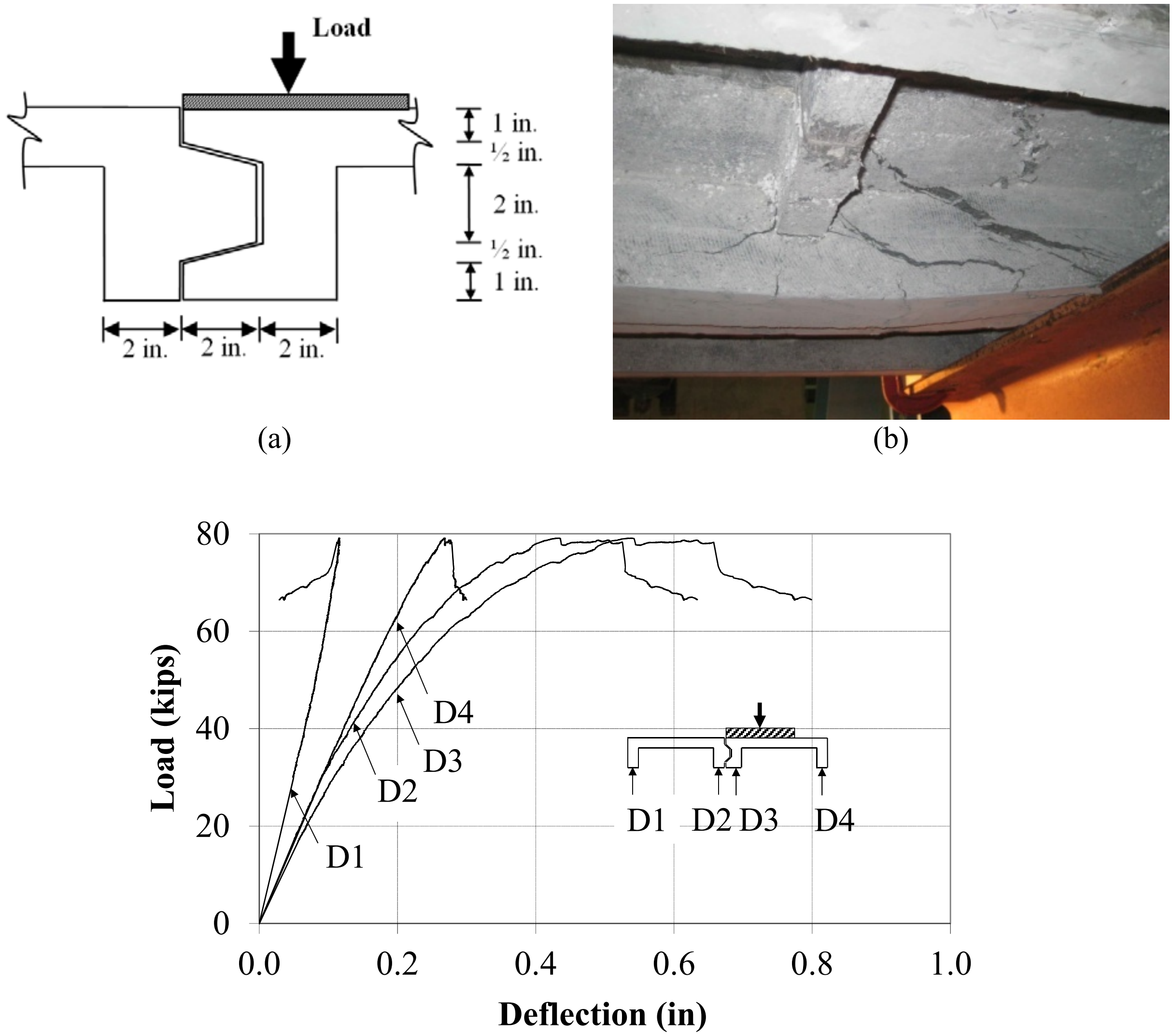

(a)

(b)

(c)

Figure 2.5 Testing of Deck-to-Deck Connection: (a) Schematics of the Connection; (b) Mode of Failure; and (c) Load-Deflection Responses

2.2.4 Lateral Distribution of Live Loads

Guidelines for lateral distribution of load for this type of deck are not readily available in the AASHTO (2005), hence there was a need to determine the share of the load taken by each rib. For this purpose, simple-span and two-span flexural tests were performed on different specimens with different loading configurations. All specimens were loaded at the same displacement rate of 0.015 in./min. Using the deflection criteria, distribution factor $(DF)_i$ for each rib i is calculated as

$$DF_i = \Delta_i / \sum \Delta_i \qquad (2.1)$$

Where Δ_i is the deflection for rib i. The DF for each rib was calculated at service load, while also tracked throughout the loading history. Figure 2.6 shows the service load DF_i for each specimen.

The reason for calculating *DFs* at service load is that the deck remains within the elastic range at the service load and use of deflection for calculating *DFs* is more justifiable within the linear elastic limit. In Specimen 5T1S, where the load was applied symmetrically with two ribs on either side, 79.5% of the load was resisted by the rib directly under the load and its two adjacent ribs. In Specimen 4T1S, with asymmetrical load, 89.1% of the load was taken by the rib directly under the load and those next to it on either side. These two tests indicate the trend that when the load is applied directly on one of the ribs most of it is taken by that rib and the two ribs immediately adjacent to it. In Specimen 4T2S, where the load is applied between the ribs, the two nearby ribs took 69.8% of the load. Results of the three specimens show that the ribs either under the load (or immediately next to it, when the load is applied between the ribs) take an average 34% of the load. The fact that the rib under the load shares only 34% of total load emphasizes the need of optimization of single-unit (T-section) of deck system. Currently, the single-unit is designed to take the full target load of 37.24 kip. In the future research this single-unit could be designed for 34% of the target load which will help in reducing the self-weight of the system.

The specimen with deck-to-deck connection, however, exhibited a different distribution than the other single panel specimens. The load was applied on the edge of the connection on the rib with groove. The two ribs that together form the connection took a total of 64% of the total load, with 35% and 29% for the rib directly under the load and the one next to it, respectively. The 6% difference between the two ribs needs to be minimized, if not eliminated altogether, for a better load transfer between panels. This may be accomplished by epoxy grouting of the joint.

Figure 2.7 shows the variation of the load share, indirectly calculated based on deflections, for each rib with the progression of loading. It can be clearly seen that the share of the load for the rib directly under the load or immediately next to it, when load is applied between the ribs, increases with the load. On the other hand, the share of the load for the edge ribs decreases at higher loads. This implies that the area closest to the loading pad attracts more load as the test progresses. This is consistent with the punching failure seen in single panel specimens. On the other hand, joint rotation in the specimen with deck-to-deck connection prevented the punching failure, as also seen by the more gradual variation of the load share of the center ribs for this specimen. It is important to note that calculation of load distribution based on deflection criterion is more justifiable in the linear elastic range. Ribs under/near the loading pad deflect more at higher load due to nonlinear behavior therefore the calculations of load distribution based on deflection provides approximate results.

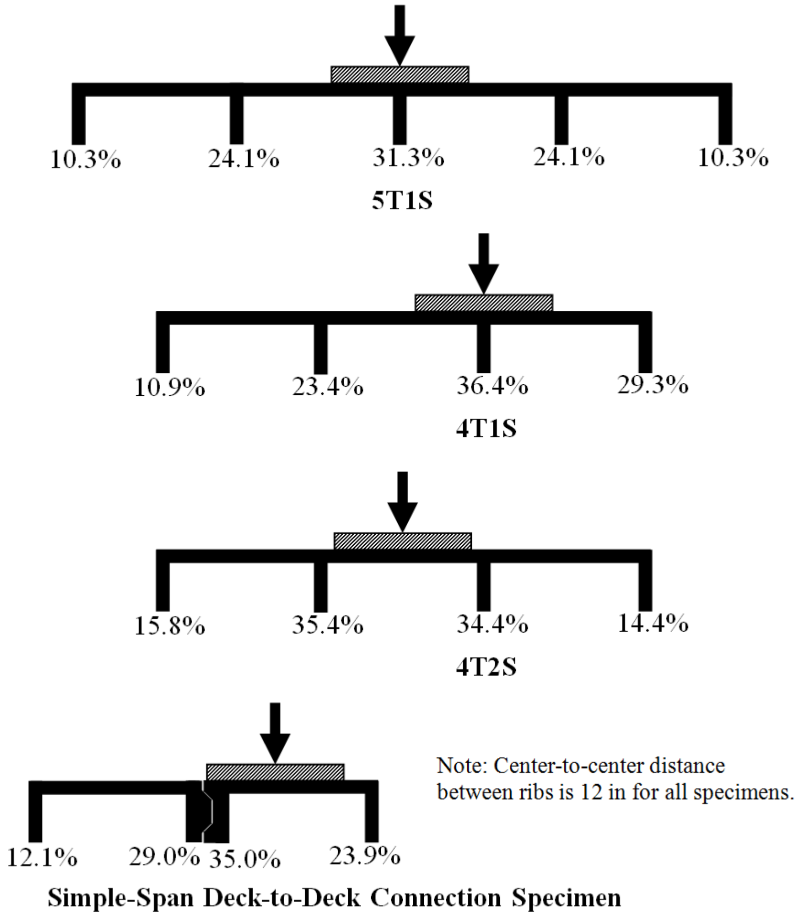

Note: Center-to-center distance between ribs is 12 in for all specimens.

Figure 2.6 Service Load Distribution Factors in Each Specimen

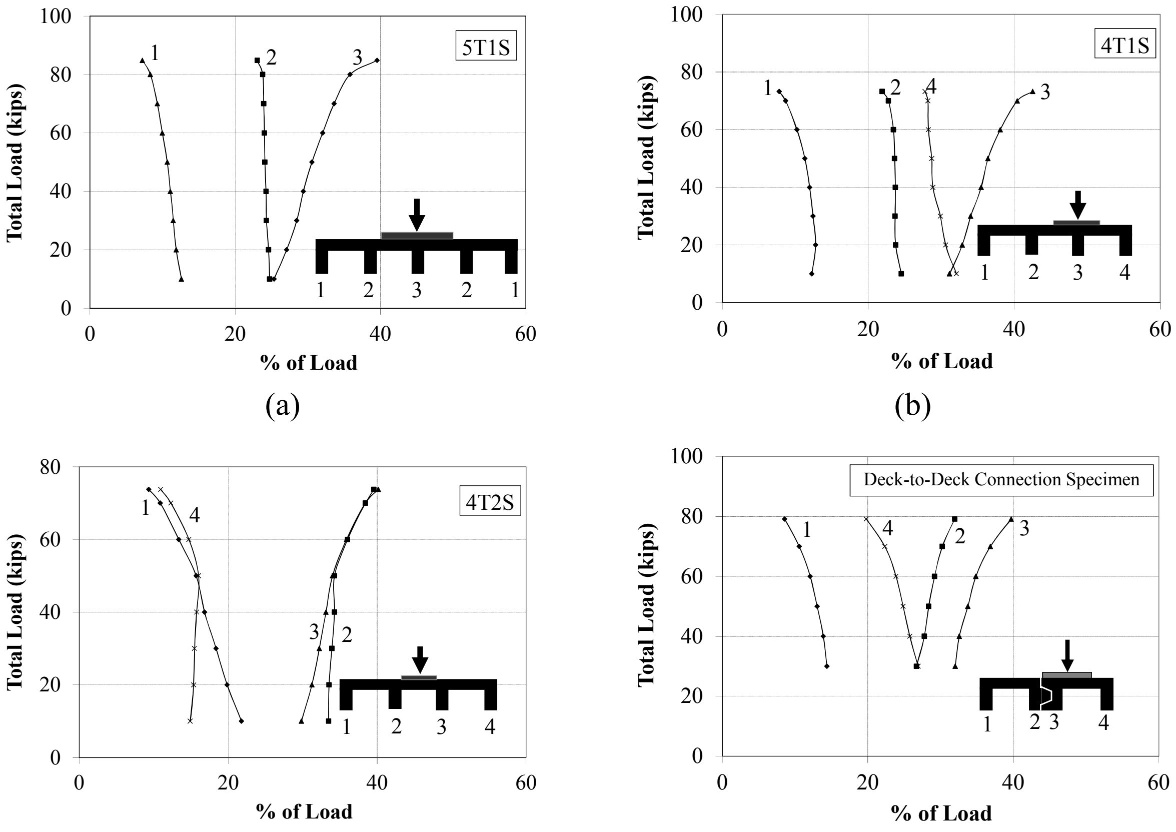

(a) (b)

(c) (d)

Figure 2.7 Variation of Load Distribution Factors for: (a) Specimen 5T1S;
(b) Specimen 4T1S; (c) Specimen 4T1S; and (d) Deck-to-Deck Connection Specimen

2.2.5 Fatigue and Residual Strength Tests

The idea behind performing this test was to evaluate the long-term performance of the full-scale specimen along with the deck-to-deck and deck-to-girder connections. The specimen consisted of two independent two-span deck panels connected to each other through tongue and groove connection and with the girder through a shear stud. The deck-to-girder connection was also changed to stepped instead of using rectangular, based on the findings of the uplift test. To ensure proper lateral distribution of load and avoid the differential deflection between the ribs of the tongue and groove, as experienced in the deck-to-deck test, epoxy was used to join tongue and groove. All joints were sealed, and then epoxy was poured from top of the connection. Pouring of epoxy was completed in three steps spanning three days to make sure that it has filled the entire area of tongue and groove, as some epoxy was initially lost to leakage. The epoxy was given 24 hours from the last pour to fully cure. Figure 2.8 shows the instrumentation plan and loading configuration for the fatigue and residual strength tests. In addition to the displacement transducers shown in Figure 2.8, strain gauges were applied on top and bottom steel rebars as well as concrete surfaces at the locations of maximum positive and negative moments. Two loading pads were placed at the center of each span at a center-to-center distance of 4 ft, which is more critical than the 6-ft wheel spacing of an HS20 truck. Deck panels were subjected to two million cycles of design truck single axle sinusoidal load in the range of 0.5 – 16 kip in each span at a frequency of 4 Hz. The lower limit of 0.5 kip was set to prevent the pads from walking (Vyas et al. 2009). The test was run continuously for about six days. Load, displacement and strain data were recorded continuously for 16 sinusoidal cycles after every 1,000 cycles. During and after the test, the deck panels were monitored for cracks in the panels or connections. After the fatigue test, two static tests were performed on the panels to determine their residual strengths.

After 2 million cycles of fatigue loading, the deck panels showed no sign of cracking or failure. Figure 2.9 shows a rapid increase in deflection at D6 after 20,000 cycles. Although nothing unusual was observed, however there could be some cracking in the epoxy which could have affected the distribution of load in Span 2 causing this growth of deflection. Change in response of D2 after 200,000 cycles can also be attributed towards cracking in epoxy. In open grid steel deck bridge, the steel girders provide the longitudinal stiffness therefore the local deflection in the deck does not affect the total deflection of the superstructure (Vyas et al. 2009). The absolute maximum deflection was observed in D6, which increased from 0.04 in. (L/1200) at cycle 1 to 0.15 in. (L/320) at cycles 2,000,000. The long-term deflection growth deserves further study and monitoring in the field. Fatigue loading developed compressive stresses in the range of 2.5 to 4.9 ksi in concrete, and tensile stresses in the range of 5.5 to 16.6 ksi in steel.

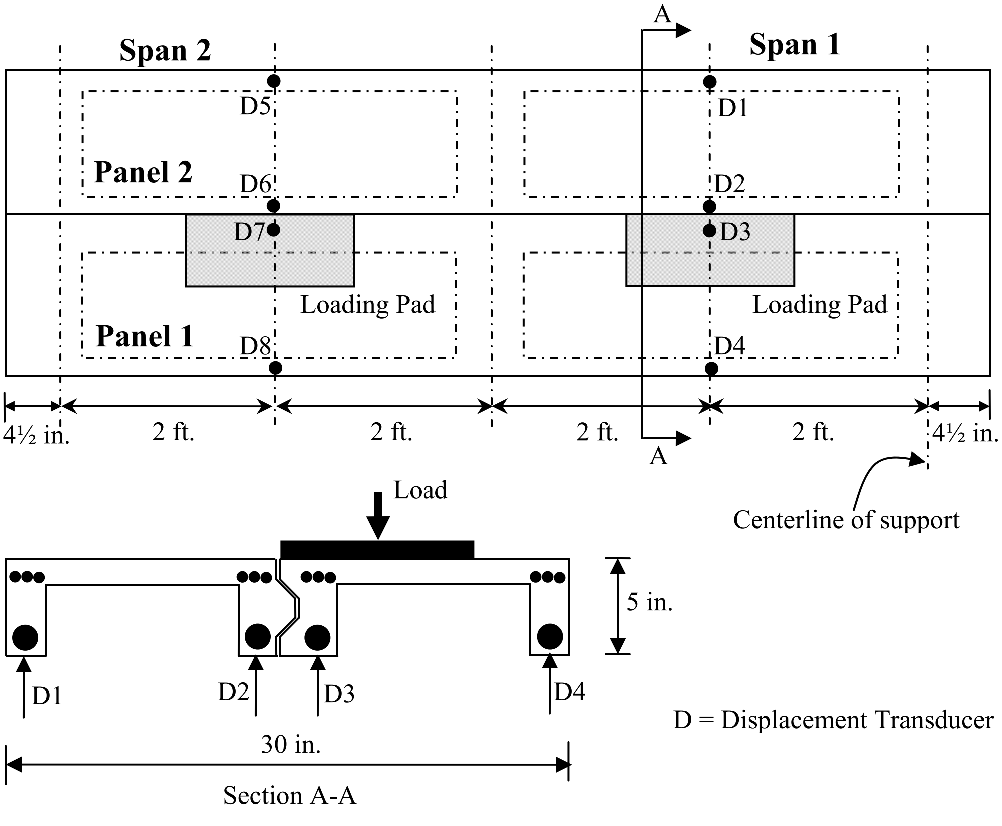

Figure 2.8 Loading Configuration and Instrumentation Plan for the Fatigue Test

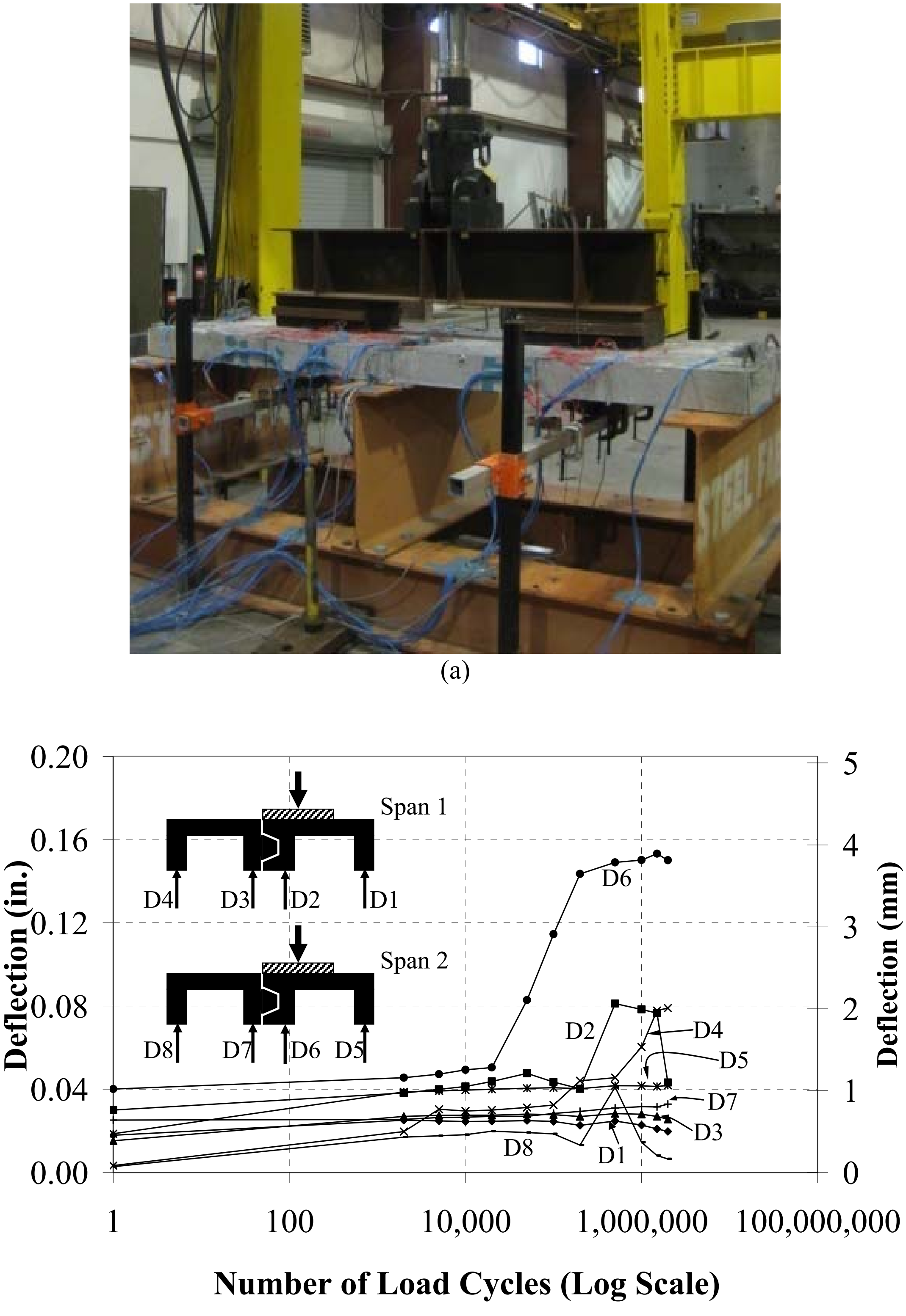

(a)

(b)

Figure 2.9 Fatigue Test: (a) Test Setup and (b) Deflection Growth

Figures 2.10 and 2.11 show the test setup, the load-deflection responses and cracking pattern for the two residual strength tests. In each test, only one span was loaded. In the first test (Test A), load was applied at the edge of the deck-to-deck connection, whereas in the second test (Test B) the load was applied on top of the connection. In Test A, the first shear crack appeared near the interior support at 40 kip, and the specimen achieved an ultimate load of 55 kip, which is 47% more than the target load of 37.24 kip. The shear crack kept on growing beyond 40 kip with smaller cracks appearing at the interior support. Approaching the ultimate load, longitudinal cracks appeared in the edge rib and in the rib with the tongue. It appears that the loading pad started punching close to ultimate load, which developed tensile force between the flange and the edge rib leading to the longitudinal crack. The longitudinal crack in the rib with the tongue may have developed due to the shearing of the tongue. As the loading pad punched at ultimate load, ribs with tongue and groove took greater portion of the load, and the edge rib at the far end of the loading point experienced a relief in its load share, as visible in the load-deflection responses.

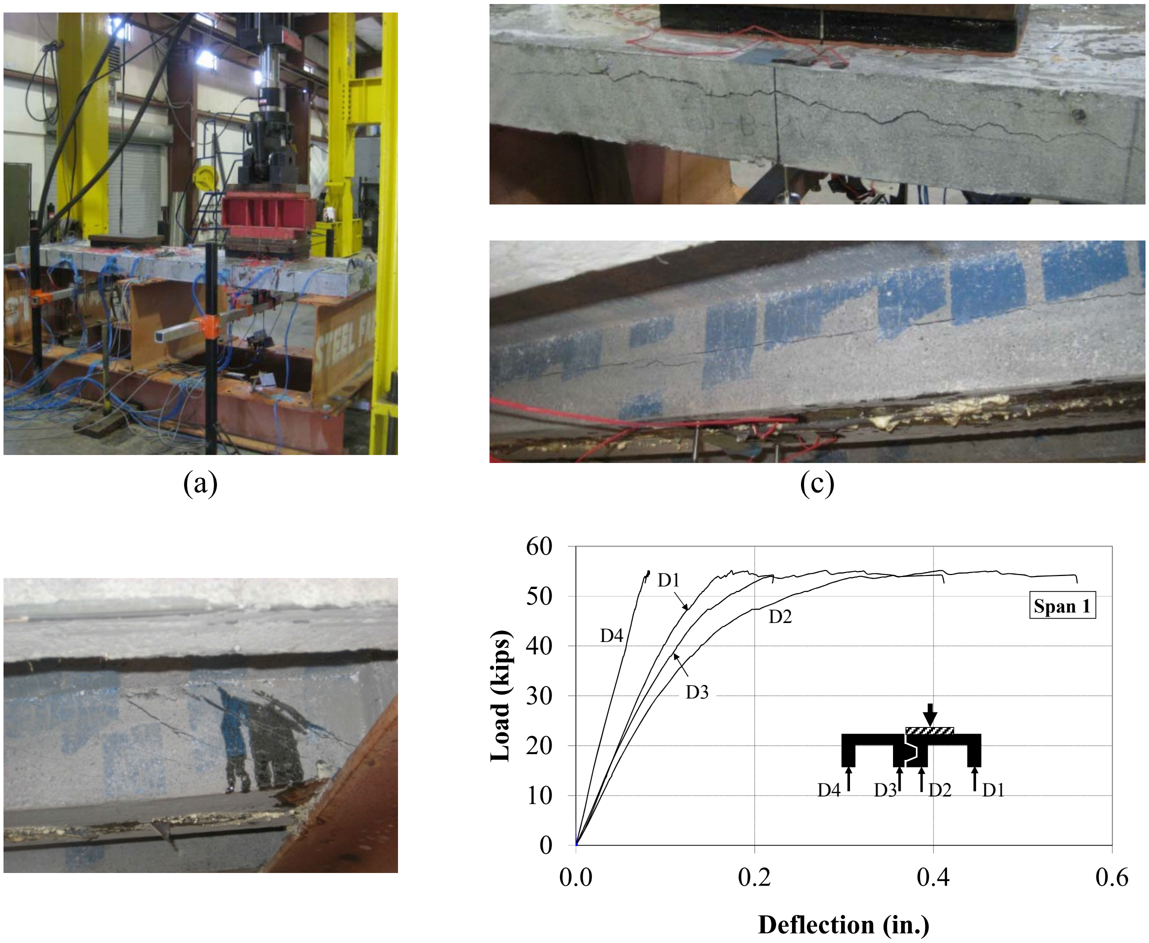

(a)

(c)

(b)

(d)

Figure 2.10 Residual Strength Test with Load on Edge of Deck-to-Deck Connection:
(a) Test Setup; (b) Shear Cracks; (c) Longitudinal Cracks; and (d) Load-Deflection Responses

In Test B, the first longitudinal crack in one of the edge ribs was seen at 60 kip and the first shear crack near the interior support appeared at 70 kip. The specimen achieved an ultimate load of 72.4 kip, 94% higher than the target load. The specimen maintained this ultimate load for some time and the deflection kept on increasing, while more shear cracks appeared at both supports of the loaded span, and then grew towards the mid-span. Cracks appeared near the mid-span were smaller than those near the supports, and were closer to the web and flange junction. Punching of the loading pad was also observed at the time when load started dropping. The difference between the ultimate loads of Tests A and B shows that the load is more evenly distributed when it is applied directly on the connection rather than its edge. The specimen also showed a more ductile behavior in Test B as compared to test A. In Test A, the difference between the load at the first shear crack and the ultimate load was 15 kip (or 27% of the ultimate load); while in Test B it was only 2.4 kip (or 3% of the ultimate load). Therefore, the situation when the truck wheel is at the edge of the deck-to-deck connection is more critical, as compared to the case when wheel is directly on top of the connection.

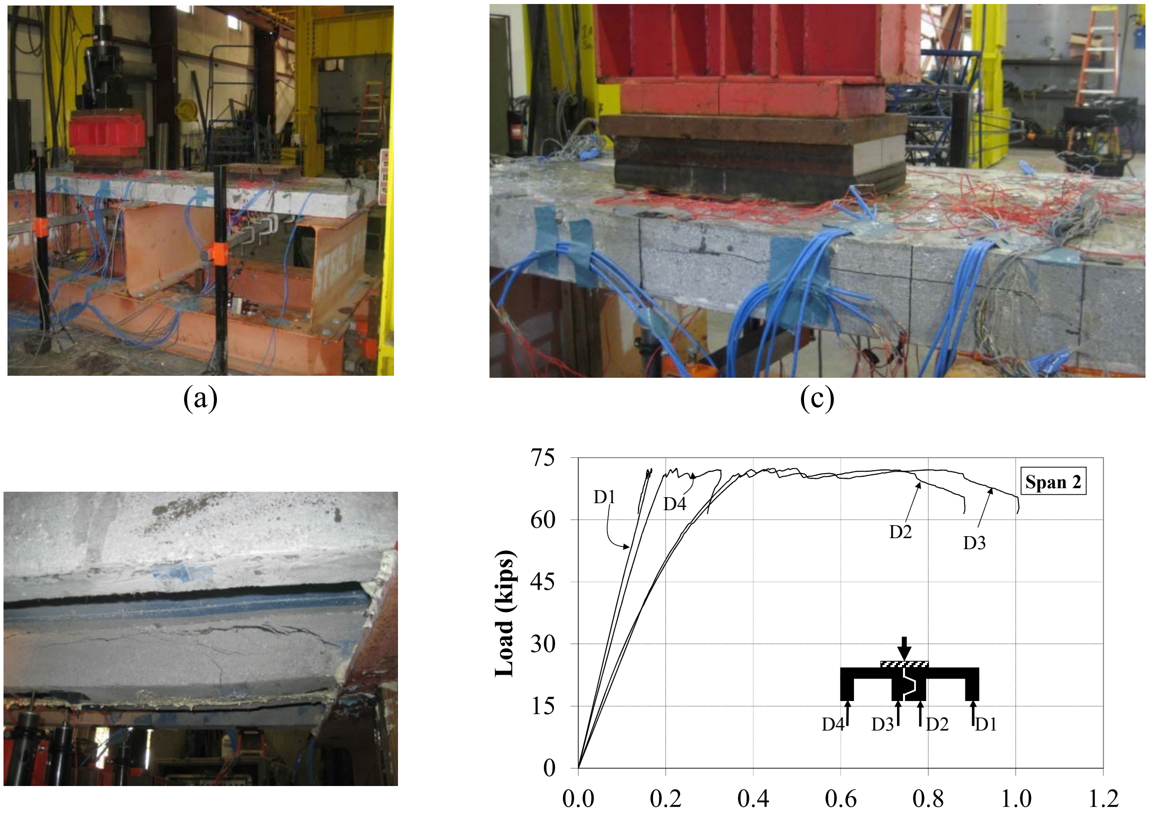

(a) (c)

(b) (d)

Figure 2.11 Residual Strength Test with Load on Top of Deck-to-Deck Connection:
(a) Test Setup; (b) Shear Cracks; (c) Longitudinal Cracks; and (d) Load-Deflection Responses

2.3 Experimental Work and Discussion – Part 2

This part of the experimental work focused on estimating the development length of #3 and #7 HSS rebars in UHPC. At the initial stage, pullout tests were carried out to have an idea about the range of embedment length in which development length could exist and then beam tests were performed refine the results. Although some researcher (Harajli et al. 2002 and Mo and Chan 1996) have pointed out that pullout tests underestimate the bond strength, however, these could provide lower bond results. Table 2.2 shows the test matrix including pullout and beam tests.

Table 2.2 Test Matrix – Part 2

Type of Test	Bar Size	Embedment Length		Number of Specimens
			(in.)	
Pullout	#3	8d_b	3	3
	#3	10d_b	3.75	3
	#3	12d_b	4.5	3
	#7	8d_b	7	3
	#7	10d_b	8.75	3
	#7	12d_b	10.5	3
	#7	18d_b	15.8	3
Beam	#3	10d_b	3.75	2
	#3	12d_b	4.5	2
	#3	14d_b	5.25	2
	#3	48d_b	18	2
	#7	14d_b	12.3	2
	#7	16d_b	14	2
	#7	18d_b	15.8	2
	#7	21d_b	18.4	2

Since the proposed deck includes #3 and #7 rebars as main reinforcement, only these two rebar sizes were tested. All pullout specimens were prepared with 2 in. width to match the width of the primary rib of the proposed deck. Also, top and bottom covers in the pullout specimens were both kept as ½ in. to match the clear cover of the main rebars in the deck. Figure 2.12 shows the schematics of the pullout specimens, all of which were 12 in. long, except the three specimens of #7 rebar with 18d_b embedment length (i.e., 18 in.), where d_b is the rebar diameter. Polyvinyl chloride (PVC) tubes were used to achieve different embedment lengths.

Tests were performed on a universal testing machine, which had two platforms: one stationary and other moving. The pullout specimens were supported against the stationary-platform and the steel bars were gripped in the moving-platform. When moving-platform was moved upward it pulled the steel bar while subjecting concrete to compression. Load was applied at a rate of 25 lb/sec. Three quantities were measured during the pullout tests: load, rebar slip relative to concrete, and the strain in rebar. The measured slip was corrected for the elongation in the steel rebar. The slip, however, did not account for the compression strain in the concrete. The compression strain in UHPC is expected to be much smaller than regular concrete because UHPC has modulus of elasticity more than 2.5 times higher than the regular concrete. Slip and strains were measured using a string potentiometer and a surface mounted post-yield strain gauge, respectively. Strain gauge was installed on the steel rebar near the loaded end of concrete. All instrumentation was connected to a high-speed data acquisition system, recording the data at a frequency of 1 *Hz*. The embedment lengths were initially selected as $8d_b$, $10d_b$ and $12d_b$, based on the flexural tests of the deck samples (Saleem et al. 2011) and previous studies (Harajli et al. 2002). Based on the results of these specimens, three (3) more specimens of #7 rebar with an embedment length of $18d_b$ were cast and tested.

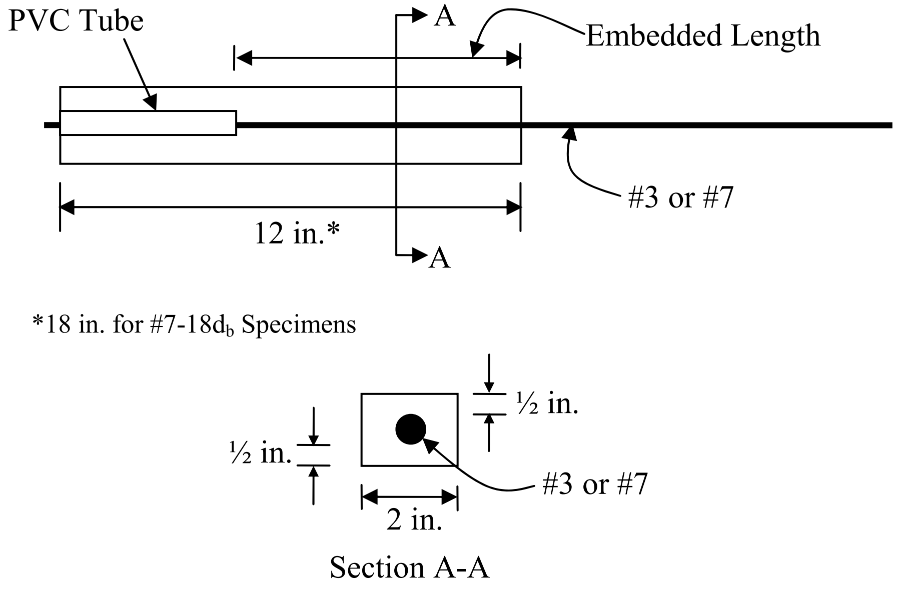

*18 in. for #7-$18d_b$ Specimens

(a)

(b)

Figure 2.12 Pullout Test: (a) Schematics of Specimens and (b) Specimens Ready for Casting

The beam specimens had a T-section and the web similar to the ribs of the proposed deck. The width of the web was 2 in. for both #3 and #7 rebars and a clear cover of ½ in. at the bottom. End blocks were added to avoid twisting of the specimen due to unintentional eccentricity during loading. Figure 2.13 shows the schematics and instrumentation of the specimens in four-point bending. A data acquisition system monitored the load; mid-span deflection; rebar slippage relative to concrete; and strains in steel rebar at mid-span, under one of the loads, and at the middle of the embedment length. Specimens were constantly observed during the test to note any sign of distress. Excessive cracking or displacement and significant load drop were considered as failure and an indication to stop the test.

Previous studies have shown that the beam tests estimate the bond strength more accurately than pullout tests (Harajli et al. 2002 and Mo and Chan 1996). However, previous studies did not encounter the challenge of the small concrete cover, as in the present study. The small cover could not only cause premature failure, but could also make it more difficult to provide shear stirrups, necessary to avoid shear and splitting failure. Tastani and Pantazopoulou (2010) reported that transverse reinforcement and thick cover may both prevent or delay the splitting failure. Transverse reinforcement may also help in enhancing the ductility while increasing the bond strength very slightly (Harajli et al. 2004). Because of space limitation, #2 plain steel rebars of Grade 60 were used as shear reinforcement at an average spacing of 1.5 in. on center, slightly larger than the ACI 318-08 recommended minimum spacing (effective depth/2) of 1.3 in. and 1.4 in. for the #3 and #7 rebar specimens, respectively. It should be noted that specimens with # 3 and #7 rebar have slightly different effective depth while they had same clear cover of ½ in. Smaller spacing of stirrups would have created issues in placing the UHPC and tying the shear reinforcement to the flexural reinforcement.

Additionally, some of the previous studies included spliced rebars to evaluate the bond and development behavior (Harajli 2004, Azizinamini et al. 1993, and Seliem et al. 2009). However, given the size limitation of the ribs, such arrangement was not possible in the present study. Based on the results of the pullout tests, it was decided to use $10d_b$, $12d_b$ and $14d_b$ for #3, and $14d_b$, $16d_b$ and $18d_b$ for #7 rebars beam specimens. Two beam specimens of each rebar size (#3 and #7) were tested without any PVC tube, leading to embedment lengths of $48d_b$ and $21d_b$ for the #3 and #7 rebars, respectively.

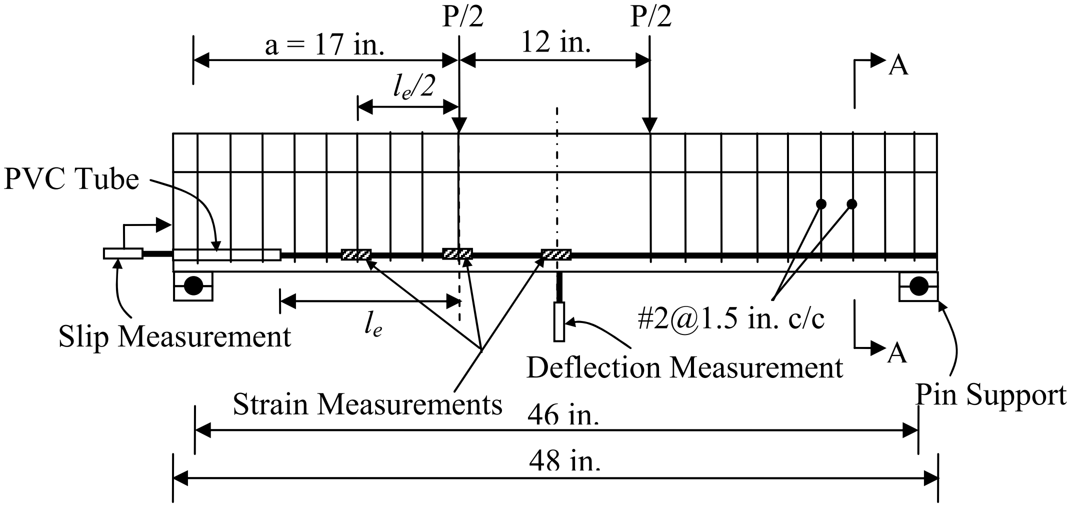

Instrumentation Plan

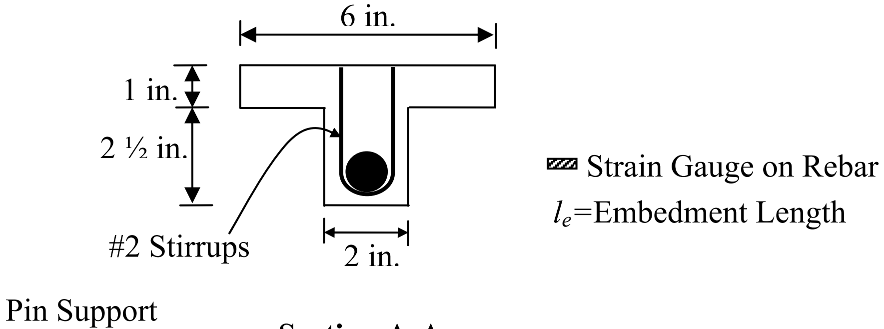

Section A-A

Figure 2.13 Schematics of Beam Specimens with Instrumentation

2.3.1 Pullout Test – Discussion

Figure 2.14 shows typical load-slip responses for #3 rebar specimens with $8d_b$, $10d_b$ and $12d_b$ embedment lengths. Because plotting all the responses together would make it difficult to differentiate among them, only a typical response is plotted from each group of embedment lengths. A complete summary of ultimate strains and ultimate slips is provided in Table 2.3. The failure load consistently increased with the increase in the embedment length. However, the variation of slip is not consistent. For instance, in Figure 2.14, the specimen with $12d_b$ embedment length showed higher slippage than the specimens with $8d_b$ and $10d_b$ embedment lengths. One reason could be the local failure of concrete key near one of the transverse ribs of steel rebar at a load of around 5.5 kip, when a change of stiffness is noted. Lack of interlocking due to the absence of coarse aggregate could also be a reason for sudden increase in slippage. Two out of three #3 rebar specimens with $12d_b$ embedment length crossed the yield strain threshold of 0.004, with a magnitude of 0.0067 and 0.0049. This indicates a development length of around $12d_b$ for #3 rebars.

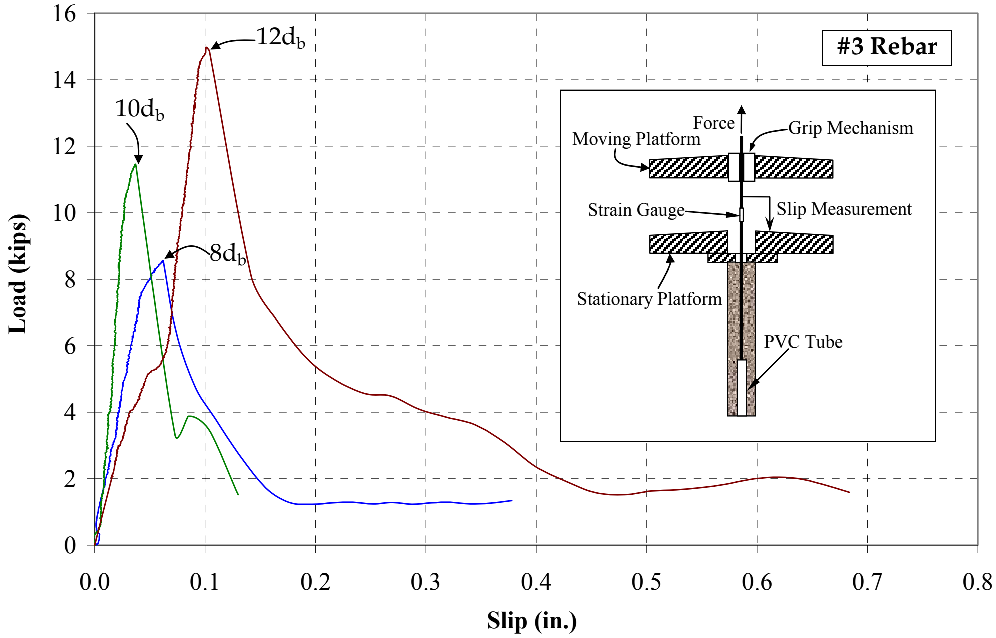

Figure 2.14 Typical Load-Slip Responses for #3 Rebar Pullout Specimens

Figure 2.15 presents the typical load-slip responses for #7 rebar pullout specimens. Initially, the specimens with $8d_b$, $10d_b$ and $12d_b$ embedment lengths were tested and then based on the observed trend of the strains, it was predicted that the yield strain could be achieved with an $18d_b$ embedment length. Therefore, three specimens with $18d_b$ embedment length were cast and tested in the second phase along with the beam specimens. Specimens with $8d_b$, $10d_b$ and $12d_b$ embedment length showed consistent behavior, however, the ones with $18d_b$ depicted very different responses. Previous studies on lightweight concrete have indicated that bond strength would decrease with the increase in embedment length (Khandaker and Hossain 2008). The behavior of the $18d_b$ specimens indicates that this is also true for UHPC. Azizinamini et al. (1993) also made a similar argument that increasing the development length is not an efficient way to enhance the bond strength in case of high-strength concrete (HSC), especially when cover is small. It appears that bond strength increases with the increase in embedment length up to a threshold, after which it decreases with any further increase in the embedment length. For the specimens of the present study such threshold appears to exist somewhere between $12d_b$ and $18d_b$. With the increase in the embedment length, more and more transverse ribs are available to resist the applied force, which causes stress concentration in the region around the load bearing area, resulting in premature failure. Azizinamini et al. (1993) argued that in comparison with normal strength concrete specimens, HSC specimens have stronger concrete keys in front of transverse ribs, which have higher resistance against crushing and slippage leading to the concentration of bond force in few ribs at the loaded end. Both the stronger concrete keys and a larger number of ribs can cause stress concentration at the loaded end. In the present study, concrete keys are quite strong, and with the increase of embedment length, it further helps in resisting the force and increasing the chances of stress concentration leading to an early failure of load bearing area. None of #7 rebar specimens reached the yielding strain, indicating that the steel rebars were not fully mobilized. Figure 2.16 shows the modes of failure of all specimens. Most of the #3 rebar specimens showed one distinct crack that runs from the loaded end up to the full embedment length. However, Specimens #3-12d_b-1 and #3-12d_b-2 showed some local cracks near the loaded end. All #7 pullout specimens showed significant local cracks pointing towards stress concentration in the load bearing region. Another reason for local cracks is smaller cover on one side of #7 rebars, as compared to the #3 specimens. The smaller concrete cover and the stress concentration prevented full mobilization of stress in rebars. It may be concluded that the pullout tests may not provide appropriate results for large rebar sizes when small concrete cover is provided.

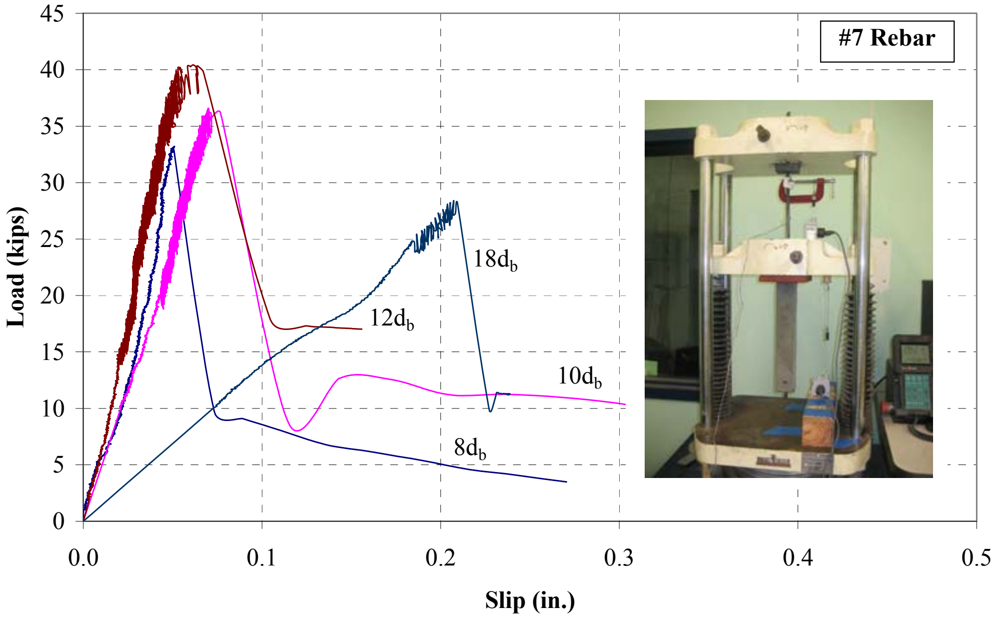

Figure 2.15 Typical Load-Slip Responses for #7 Rebar Pullout Specimens

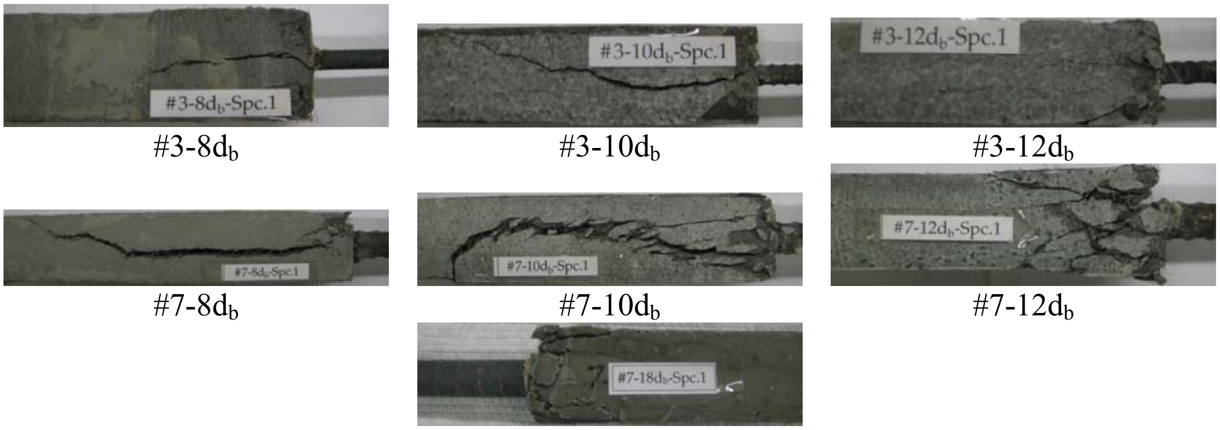

#3-8d_b #3-10d_b #3-12d_b

#7-8d_b #7-10d_b #7-12d_b

#7-18d_b

Figure 2.16 Modes of Failure in Pullout Specimens

Table 2.3 Summary of Pullout Test Results

Specimen Name	28-day Compressive Strength (ksi)	Rebar Strain at Ultimate Load (ε_u)	Strain Ratio ($\varepsilon_u / \varepsilon_y$)	Slip at Ultimate Load (in.)
#3-8d_b-1	24.0	0.0025	0.63	0.115
#3-8d_b-2	24.0	0.0021	0.53	0.070
#3-8d_b-3	24.0	0.0028	0.70	0.062
#3-10d_b-1	24.0	0.0040	1.0	0.037
#3-10d_b-2	24.0	0.0033	0.83	0.048
#3-10d_b-3	24.0	0.0025	0.63	0.080
#3-12d_b-1	24.0	0.0067	1.68	0.101
#3-12d_b-2	24.0	0.0035	0.88	0.039
#3-12d_b-3	24.0	0.0049	1.23	0.053
#7-8d_b-1	24.0	0.0016	0.40	0.051
#7-8d_b-2	24.0	0.0011	0.28	0.025
#7-8d_b-3	24.0	0.0024	0.60	0.031
#7-10d_b-1	24.0	0.0021	0.53	0.051
#7-10d_b-2	24.0	0.0020	0.50	0.077
#7-10d_b-3	24.0	0.0022	0.55	0.086
#7-12d_b-1	24.0	0.0025	0.63	0.055
#7-12d_b-2	24.0	0.0019	0.48	0.064
#7-12d_b-3	24.0	0.0024	0.60	0.061
#7-18d_b-1	25.2	0.0017	0.43	0.209
#7-18d_b-2	25.2	0.0017	0.43	0.115
#7-18d_b-3	25.2	0.0009	0.23	0.127

2.3.2 Beam Test – Discussion

The objective of performing beam tests was to refine the results provided by the pullout tests, especially for #7 rebars. Table 2.4 provides the summary of test results for all beam specimens. Figure 2.17 shows the typical load-deflection responses for the beam specimens with various embedment lengths. It can be seen that the #3 rebar specimens with 10d_b, 12d_b and 14d_b embedment lengths all failed at a very early stage. These six specimens cracked at the location where debonding of bottom rebar began. These were all premature flexural failures, and the steel rebars could not be fully mobilized. The ultimate steel strain in all #3 beam specimens could only reach a maximum of 20% of yield strain, except for the specimens without debonding, which corresponded to the embedment length of 48d_b. The load-deflection responses in Figure 2.17 indicate that the initial stiffness of all specimens were comparable and that the ultimate load increased with the increase in the embedment length. The #7 rebar specimens with 14d_b and 16d_b embedment lengths failed in a similar way to those of #3 beam specimens. However, #7 rebar specimens achieved higher strains than their #3 counterparts. One of the two specimens each with 18d_b and 21d_b embedment lengths crossed the yield strain and failed in flexure at the mid-span in the zero shear force zone.

Figure 2.18 shows the modes of failures of all beam specimens. The length of unbonded part of the rebar played a significant role in determining the way a particular specimen would fail.

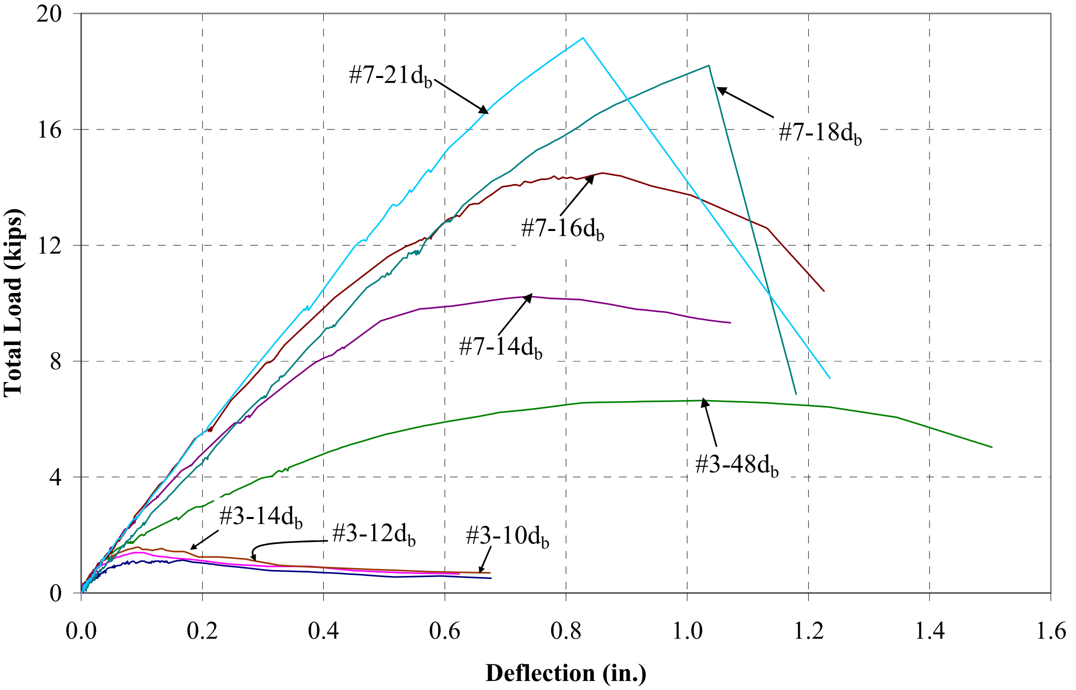

Figure 2.17 Typical Load-Deflection Responses of Beam Specimens

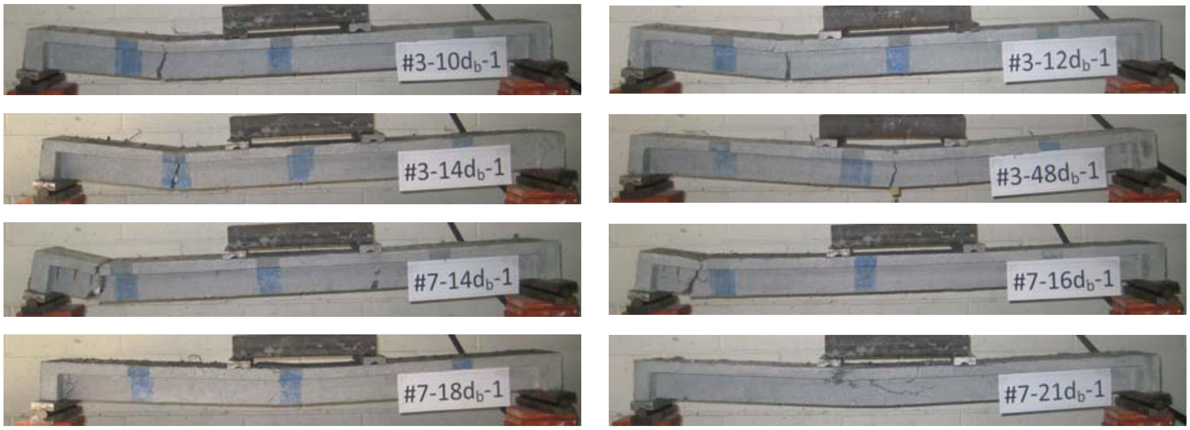

Figure 2.18 Modes of Failure in Beam Specimens

Table 2.4 Summary of Beam Test Results

Specimen Name	28 Days Compressive Strength (ksi)	Ultimate Strain in Rebar (ε_u)	$\varepsilon_u / \varepsilon_y$	Slip at Ultimate Load (in.)
#3-10d_b-1	24.4	0.0007	0.18	0.039
#3-10d_b-2	22.6	0.0006	0.15	0.033
#3-12d_b-1	25.0	0.0006	0.15	0.0037
#3-12d_b-2	25.4	Strain gauge damaged.		
#3-14d_b-1	25.8	0.0007	0.18	0.0037
#3-14d_b-2	25.5	0.0008	0.20	0.018
#3-48d_b-1	26.2	0.0218	5.45	No Slip
#3-48d_b-2	24.9	0.0109	2.73	No Slip
#7-14d_b-1	24.3	0.0026	0.65	0.306
#7-14d_b-2	25.3	0.0024	0.60	0.304
#7-16d_b-1	23.6	0.0020	0.50	0.118
#7-16d_b-2	25.0	0.0019	0.48	0.185
#7-18d_b-1	25.8	0.0071	1.78	0.077
#7-18d_b-2	24.3	0.0035	0.88	0.030
#7-21d_b-1	24.6	0.0054	1.35	No Slip
#7-21d_b-2	25.1	0.0035	0.88	No Slip

2.3.3 Comparisons with ACI 318-08, ACI 408R-03

ACI 318-08 and 408R-03 provide equations for calculating the development length for steel rebars embedded in regular concrete. ACI 318-08 limits its applicability to concretes with compressive strength lower than 10,000 psi. Azizinamini et al. (1995), however, suggested that this limit may be removed with a condition of providing shear reinforcement throughout the development and splice lengths. Hamad and Itani (1998) also called this limit as unnecessary and unwarranted. Darwin et al. (1996) concluded that $\sqrt{f_c'}$ does not provide an accurate representation of the effect of concrete compressive strength on the bond strength. His suggestion of instead using $\sqrt[4]{f_c'}$ for concretes with compressive strengths between 2,500 and 16,000 psi was adopted in ACI 408R-03.

From the test results of this study, it appears that the restriction of 10,000 psi compressive strength is valid for HSS embedded in UHPC. Figure 2.19 provides a comparison of the development lengths suggested by the present study and those calculated from the formulae of the ACI 318-08 and ACI 408R-03. The values of f_c' and f_y used for calculating the development lengths were 25,000 psi and 100,000 psi, respectively. The figure clearly shows that the ACI 318-08 lead to very high values of the development length for both #3 and #7 rebars. However, the values calculated from the ACI 408R-03 are very close to the ones recommended based on the present study. According to the ACI 408R-03, the development lengths for #3 and #7 rebars are 15d_b and 20d_b, respectively, versus the 12d_b and 18d_b suggested by the present study. This study also confirms the conclusion of Seliem et al. (2009) that for HSS rebars, the equations of ACI 408R-03 provide a reasonable development length.

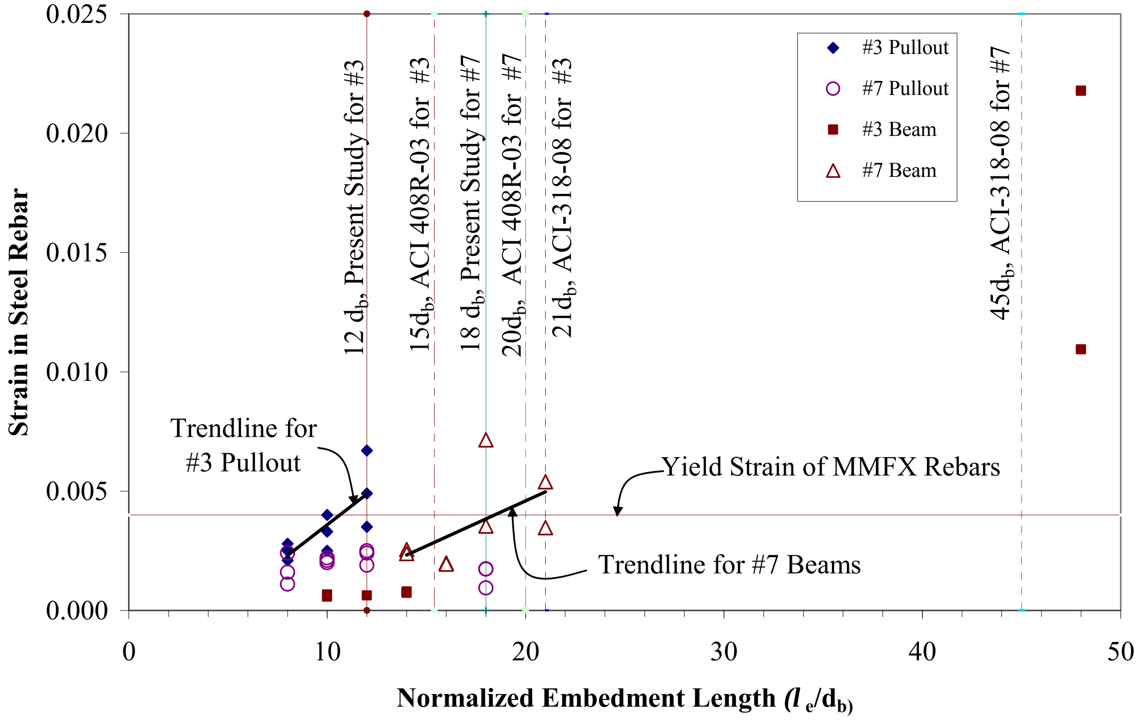

Figure 2.19 Comparisons of Test Data from Present Study with ACI 318-08 and ACI 408R-03

2.4 Guides on Design, Installation and Inspection

The UHPC-HSS deck system with its waffle configuration has been shown to meet the strength and serviceability requirements, while staying within the weight and depth limits specified for the 4-ft stringer spacing given in this project. The need for a 30% reduction in the weight of the proposed deck (from its current value of 25 lb/ft^2 to a preferred value of 17 lb/ft^2) was recently communicated through FDOT District 4 to the Research Team to help accommodate some of the existing bascule bridges due the higher weight limitations of their trunnions. The current design could be further improved by either optimizing the size of the rebars and the depth of the ribs, or through the re-design with a lighter weight reinforcement, i.e., stay-in-place fiber reinforced polymer (FRP) system that is integrated with the UHPC.

In its current configuration of the UHPC-HSS deck system, the design moment, M_u, for a single unit section on 4-ft stringer spacing is 45 kip-ft, which becomes 15.3 kip-ft based on the experimentally determined distribution factor of 0.34. The nominal strength of the section, M_n, may be calculated as 19.7 kip-ft, with a conservative use of 100 ksi yield strength for the HSS rebars, and using the same rectangular stress block as that of the normal strength concrete as specified by the AASHTO LRFD (2005). This leads to a very conservative strength reduction factor of 0.78, offering an additional safety factor of 1.15, which implies that the section could be optimized by reducing the size of the rebars and the depth of the ribs.

In terms of its serviceability, the proposed UHPC-HSS deck closely meets the L/1,200 limit on deflection at service loads, i.e., 0.04 in. on a 4-ft stringer spacing (see AASHTO 9.5.2).

Therefore, the depth of the ribs should not be reduced significantly, if the deflection limits are to be observed. However, size of the rebars may be further optimized. Additional work is also needed to assess the cracking behavior of the deck, particularly in terms of inspection. Further studies are also needed to help with better understanding of the punching shear of the proposed UHPC-HSS deck.

Installation of the proposed UHPC-HSS deck could take place using either precast or cast-in-place procedures. The experiments have clearly shown the need for epoxy grouting of the joints between different modules. Procedures for the connections to shear studs have also been shown in earlier sections. Given that all exposed surfaces of the proposed UHPC-HSS deck are concrete, visual inspection of the deck should include signs of deterioration, such as location, pattern and size of cracks, discolorations, blistering, or otherwise abnormal surface conditions.

2.5 Conclusions

This research work reported in this chapter was focused on experimental evaluation of a UHPC-HSS deck system for movable bridges and estimation of development length of HSS embedded in UHPC, with small cover. Initially, the connections were tested to establish their individual capacities and later on the complete system was tested for evaluating the long-term performance. Pullout and beam tests were performed for determining the development length. The deck-to-girder and the deck-to-deck connections both proved to be adequate for the loading conditions expected from the HS20 truck and wind forces. The failure pattern observed during the shear test of the deck-to-girder connection is not expected in the field due to the confinement effect of the concrete around the connection area. Tests for the live load distribution showed that most of the load is taken by the ribs under or immediately next to the load. The rib under the load, on average, takes 34% of the service load. This share increases with the load, consistent with the punching failure observed in single panel specimens. The share of load calculated for ribs based on deflection is however approximate, especially in the nonlinear range and only provides an estimate about how the ribs share the load. The deck panels and connections successfully endured two million cycles of repeated loading. After this fatigue test, both components had a residual strength that exceeded the AASHTO (2005) factored load requirement, by 47% for deck panels and by 94% for connections. Propagation of deflection of the rib under the load during the fatigue test may not be directly related with the strength of the deck system and needs further investigation in the laboratory and field. In the residual strength test the deck system exhibited significant deflection beyond the peak load, indicating substantial ductility and warning before failure. Differential deflection across the tongue and groove connection during the deck-to-deck connection test demonstrated the need for using epoxy grout at the tongue and groove joint. It is recommended to either use epoxy or have a match cast connection in the real bridge deck.

Development length for #3 rebars embedded in UHPC was found as $12d_b$, based on the pullout tests, and for #7 rebars as $18d_b$, based on the beam tests. These values should be considered as an estimate and may require further verification. It is observed that the pullout tests can provide reasonable results for smaller rebar sizes but not for the large rebars, especially when concrete cover is rather small. Beam tests are recommended for such cases. However, the configurations of the specimens, test setup and method of loading should be carefully selected. Development lengths calculated based on the equations provided by the ACI 408R-03 agree reasonably well with the values suggested by the present study. On the other hand, ACI 318-08 overestimate the development length for HSS rebars embedded in UHPC.

While the proposed system shows great promise, further studies are needed to optimize the design by decreasing the weight of the deck from its current 25 lb/ft^2 based on the lateral distribution of live load, assess the effectiveness of the UHPC as wearing surface, and field monitoring of the deck under ambient traffic and designated truck loading. It is also recommended to perform a set of pullout and beam tests with other rebar sizes and cover thicknesses to develop a database, which could then be used to propose an equation for calculating development length for HSS rebars embedded in UHPC. This database could also be used to propose modifications to the prevailing codes and specifications. Traditionally performed beam tests with spliced rebars may also provide helpful data for this purpose.

Chapter-3

Dowel Action of Longitudinal Steel Reinforcement in UHPC and Uniaxial Fatigue Behavior of UHPC

3.1 Introduction

Although the experimental and analytical work reported in Chapter 2 demonstrated the advantages of the UHPC-HSS ribs without any transverse (web) reinforcement, research also revealed that due to the unique properties of UHPC, both mechanical properties (Habel et al. 2006 and Habel et al. 2007) and failure modes of reinforced members of UHPC differ from those of normal strength concrete (NSC). The unique failure modes observed in the UHPC-HSS beams include ductile shear and bond failure (Xia et al. 2011). The fibers in UHPC are capable of effectively bridging flexural cracks, and the subsequent widening of shear cracks occurs only after yielding of the longitudinal reinforcement. For properly anchored longitudinal reinforcement, the ultimate shear failure is then governed by large deformations of the rebar that mobilize the dowel action, and the eventual bond failure. Even additional shear reinforcement added to the web of the UHPC section may not prevent the eventual shear failure, but may allow for some level of crack control.

To better understand the shear failure mode of reinforced UHPC specimens, their shear-moment interaction and bond were investigated in more detail. However, accurately capturing the peak load and post-peak degradation of the flexural specimens is difficult without explicit consideration of the contributions from dowel action. This is of interest because it reflects a change from the design of traditional NSC members, where the contribution from dowel action is considered negligible. The first part of this section describes the test setup used to isolate the dowel action phenomenon performed in the laboratory. The dowel action test results were analyzed based on the traditional Beam on Elastic Foundation (BEF) theory to allow future incorporation into either finite element or simplified design procedures. The results of the experimental and analytical studies on the dowel action of longitudinal steel reinforcement in UHPC are presented and discussed in this part.

In another part of this chapter, the uniaxial fatigue behavior of UHPC is investigated. In addition to consideration of strength, utilization of the UHPC beams under service conditions requires a better understanding of serviceability issues such as creep, acceptable service-level displacements, and fatigue. To investigate the design requirements for serviceability, a preliminary uniaxial fatigue test was implemented. The test description and results are presented in the second part of this chapter.

3.2 Dowel Action

In normal strength concrete (NSC), shear transfer is mainly carried by two components: concrete portion in the compression zone, and the aggregate interlocking. Due to the existence of the shear reinforcement, the NSC beam under three-point bending test usually exhibits flexural failure with widened flexural cracks at mid-span. However, for beams made of UHPC, the situation is different. Due to the unique material properties of UHPC, the shear can be transferred through three main parts, as shown in Figure 3.1: (a) concrete in compression, (b) fiber reaction contribution, and (c) dowel action. Because UHPC has considerable tensile strength, very high post-crack strength, and good bond strength with the longitudinal reinforcement, the flexural cracks can be fully controlled under the limited width. However, the shear cracks may fully develop when there is no web reinforcement crossing the cracking plane.

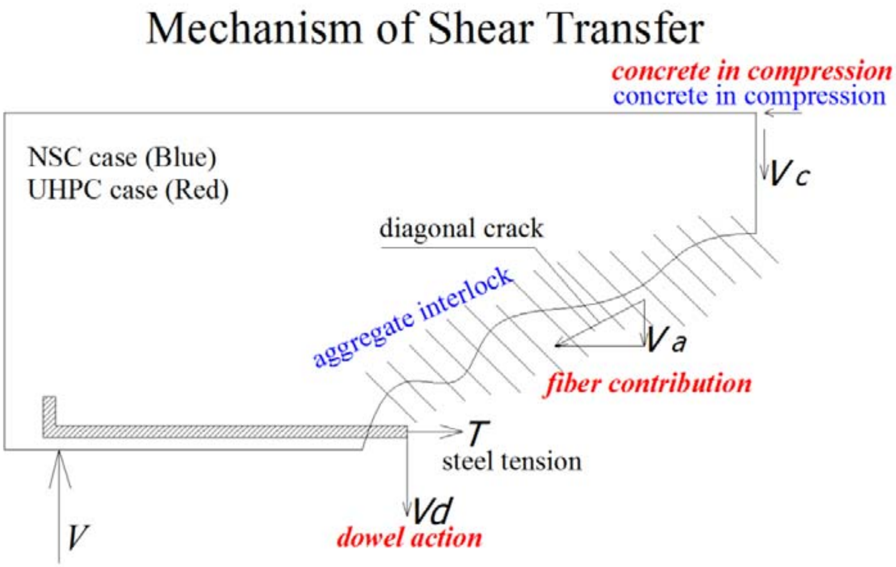

Figure 3.1 Mechanism of Shear Transfer

The direction of dowel action varies based on the location of the shear crack and direction of the shear force. It can act against the core and against the cover as shown in Figures 3.2 and 3.3, respectively. For the case of dowel action against the core, the dowel bar behaves similar to a beam on elastic foundation (Soroushian et al. 1988). The dowel load will reach the ultimate capacity when a splitting crack forms in the concrete underneath the bar. For the case of action against the cover, the bar will initially behave similar to a beam on elastic foundation. However, after the cover splits from the core, it will behave the same as a beam supported on the closest stirrup to the crack (Soroushian et al. 1988). Dowel action performance with NSC (and later FRC) has been extensively studied over the years, and the major findings are summarized in this section.

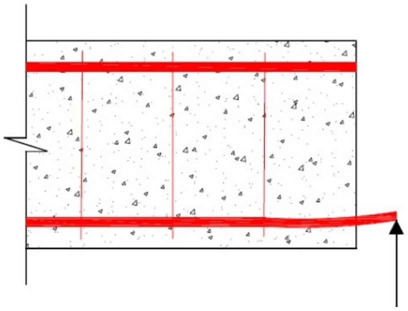

Figure 3.2 Dowel Action against Core

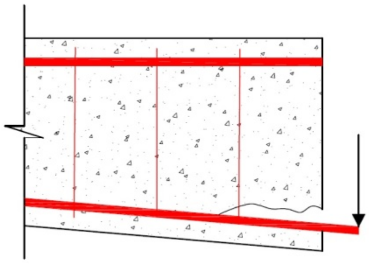

Figure 3.3 Dowel Action against Cover

Soroushian et al. (1987) investigated the behavior of bars in dowel action against concrete cover. Reinforced concrete specimens were tested with dowel action of the longitudinal bars against the cover at the beam-column interface. The specimens consisted of two concrete blocks connected together by two dowels bars, and the aggregate interlock was eliminated using greased brass sheet at the contact surface. For this setup, the bars were pushed against core in one block and against cover in the other. The results showed that the dowels behavior against cover and core are similar before a split crack separates the cover from the core. After that, the behavior depended on the bar size, concrete cover contribution, and the location and the strength of stirrup.

The shear capacity of the dowel specimen is particularly influenced by four design parameters: (1) compressive strength of concrete, (2) yield strength of steel, (3) inclination angle of transverse reinforcement, and (4) size of the dowel bar (Carpinteri et al. 1995 and Ince and Arici 2004). The contribution of the dowel action to the total shear capacity of a cracked RC bean increases with the value of ρf_y (Ince et al. 2007). The bearing strength of concrete would increase with increasing concrete strength and concrete cover normal to the direction of the bearing action. It also increases with decreasing bar diameter. The concrete bearing stiffness under dowel bars increases with increasing concrete strength and bar spacing, and with decreasing bar diameter (Soroushian et al. 1987). Moreover, shear capacity may be also affected by specimen size and maximum aggregate size.

Kwan et al. (2010) developed an analytical model for dowel action of discrete reinforcing bars. The dowel stiffness matrix was derived using the theory of BEF and the direct assemblage of dowel stiffness into the concrete matrices. He used this model to analyze two reinforced concrete deep beams with 127x254 mm cross sections subjected to a single point load at midspan. The obtained results from the numerical analyses verified that the proposed model improved the prediction of the load-deflection behavior of shear concrete members. El-Ariss (2007) developed an analytical model for the dowel action of reinforcing bars that crossing the cracks in reinforced concrete beams. El-Ariss (2007) analyzed the nonlinear behaviors of three reinforced concrete deep beams tested by previous researchers. He concluded that the dowel action has an important effect on the shear strength of the reinforced concrete beams.

Tanaka and Murakoshi (2011) investigated 24 concrete specimens with dowel bars, bolted plate-mounted bars, or welded studs to identify bearing mechanisms and failure of steel bars embedded in concrete and subjected to load. The specimens were divided into three groups. The first one was tested to investigate dowel action of steel bars and find the BEF stiffness values. The second group was prepared with steel plates mounted on both sides, while the third group was prepared by welding a headed stud to the steel plate to investigate the predictive capability of stiffness values calculated from second group. They investigated the behavior up to failure by using the experimental data and analytical theory of beam on elastic foundation. They found that there is no big difference between the depth of spalling under the bolted plate mounted and under dowel bar when compared between companion specimens. Also, welded studs gave ductile behavior and more load capacity compared to the companion dowel bars.

Swamy and Bahia (1979) concluded that the using of fiber reinforcement in concrete not only controls cracking and improves the tensile strength and ductility, but also increases the pullout resistance. They studied the effect of fiber reinforcement on dowel force and load displacement relationship of reinforcement concrete T-beam. They included four variables in their study; fiber volume, web reinforcement amount, longitudinal steel amount, and the distance of the first stirrup from the performed crack. They concluded that the presence of fiber reinforcement restrains and controls dowel cracking and also enhances the stiffness and deformation of the dowel crack zone.

All previous work on dowel performance investigation was based on NSC or fiber-reinforced concrete (FRC). Dowel action investigation on the proposed UHPC system has not been previously considered. To better understand the dowel force contribution to the shear resistance, the “dowel action” test with UHPC specimen was designed and carried out. The steel bar represents a dowel embedded into the UHPC specimen (Figure 3.4). As learned from previous dowel experiences, several parameters such as bar size, concrete compressive strength, specimen longitudinal length, and bar-concrete boundary widths will be considered as the investigation variables.

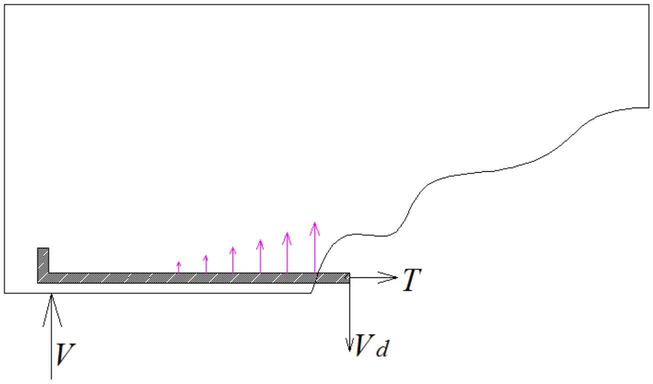

Figure 3.4 Dowel Force Distribution in the Longitudinal Direction

The dowel action contribution represents one of the control parameters for the loading capacity of UHPC beams with no shear reinforcement. Generally, the total shear resistance can be expressed as follows:

$$V = V_c + V_d + V_a \tag{1}$$

The proportion of each contributing factor can be summarized, as shown in Table 3.1.

Table 3.1 Shear Transfer Mechanisms (NSC)

	Describe	Contribution from literature review (Based on NSC)
V_c	Un-cracked concrete compression zone	20 – 40%
V_d	Dowel action of longitudinal reinforcement	15 – 25%
V_a	Vertical aggregates interlock	33 – 50%

3.2.1 Experimental Work

As discussed above, the influence of dowel action can potentially be very important for UHPC beams reinforced with longitudinal steel. However, the amount or percentage of contribution on shear resistance is still not clear. In addition, for capacity-based design purposes, it is important to better understand the load-displacement relationship, which can only be accomplished considering dowel contribution. The experimental tests were designed to predict the effect of the rebar bearing on the cover concrete after the formation of shear cracks. The traditional beam on elastic foundation modeling can be performed to find the effective distributed "subgrade" modulus (and potentially yielding strength) of the UHPC. This data can later be incorporated into the ultimate load predictions coming from the finite element method (FEM).

To obtain the concrete subgrade modulus, a pure (concentrated) dowel force was applied to the designated UHPC beam with a notch $d = 2$ inch in the middle as shown in Figure 3.5. A photo of one of the cast specimens is shown in Figure 3.6.

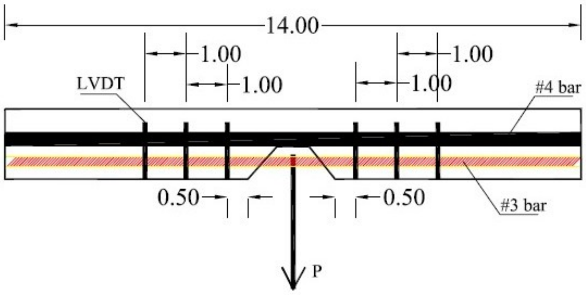

Figure 3.5 Specimen Design Details

Figure 3.6 Actual Cast Dowel Action Specimen

The bottom steel reinforcement was embedded in the concrete but was debonded with the surrounding concrete by covering with plastic pipe. The upper reinforcement was used with a constant #4 bar, size $d = 0.5$ in., bonded with concrete in order to increase the stiffness of upper concrete. Six potential meters (linear variable differential transformer, LVDTs) were attached on the front surface of the beam to record vertical displacement of the cover relative to the top section of the specimen.

The detailed connection of the beam to the Universal Test Machine (UTM) is shown in Figure 3.7.

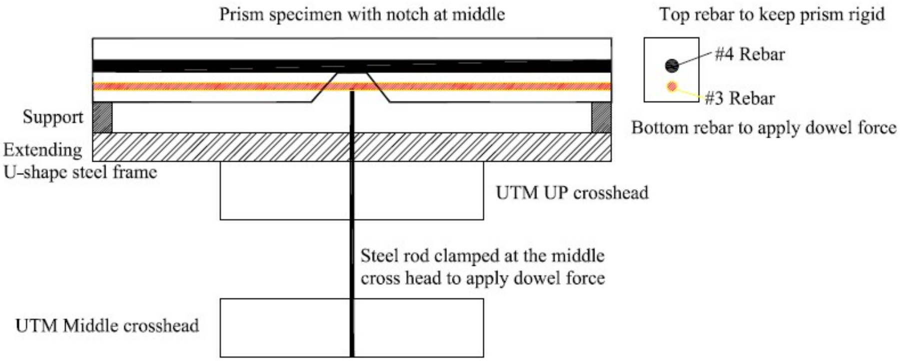

Figure 3.7 Detailed Specimen Test Setup

To investigate potential factors that may influence the concrete subgrade modulus, several comparison groups with variables were specified. The variables considered include: rebar size, beam length, bottom cover thickness as well as side cover thickness. Table 3.2 lists the detailed test matrix.

Table 3.2 Designed Specimen with Comparison Groups

Specimen group ID	Prism length L (in)	Prism height H (in)	Prism width B (in)	Bond length Lb (in)	Bottom cover (in)	Side cover (in)	Steel bar size db (in)
1	14	4.25	1.5	12	1	0.56	#3 (0.375)
2	18	4.25	1.5	16	1	0.56	#3 (0.375)
3	14	4.00	1.5	12	0.75	0.56	#3 (0.375)
4	14	4.25	1.125	12	1	0.375	#3 (0.375)
5	14	4.5	1.75	12	1	0.56	#4 (0.500)

The specimens were cast during two separate concrete pours. Several UHPC cubes were made each time during casting for obtaining general compressive strength properties. A list of detailed batches is shown in Table 3.3. The blocks before and after the compressive test are shown in Figure 3.8 and Figure 3.9, respectively.

Table 3.3 Batches Tested for Obtaining General Compressive strength of Specimen

Pour	Casting date	Batch info				
		Batch shape	Batch age upon testing	Size (in) ($a\times b\times c$)	f_c' (ksi)	Average/Max f_c' (ksi)
1st	11/29/2010	Block	60 days	1.75×1.25×1.5	21.7	19.3/24.3*
	11/29/2010	Block	60 days	1.75×1.25×1.6	24.3	
	11/29/2010	Block	60 days	1.7×1.4×1.5	19.6	
	11/29/2010	Block	60 days	1.75×1.5×1.6	19.6	
	11/29/2010	Block	60 days	1.75×1.5×1.6	16.2	
	11/29/2010	Block	60 days	1.625×1.5×1.75	14.6	
2nd	05/05/2011	Block	51 days	1.8×1.5×3.0	16.8	17.9/20.2
	05/05/2011	Block	51 days	1.5×1.25×1.75	14.9	
	05/05/2011	Block	51 days	1.5×1.25×1.75	20.1	
	05/05/2011	Block	51 days	1.25×1.00×1.25	16.8	
	05/05/2011	Block	51 days	1.45×1.125×1.6	18.0	
	05/05/2011	Block	51 days	1.5×1.3×1.25	20.2	
	05/05/2011	Block	51 days	1.25×1.00×1.38	17.3	
	05/05/2011	Block	51 days	1.9×1.45×1.95	19.3	

*Suggested to use max f_c' as compressive strength for further calculation based on current specimen data, since all f_c' listed above were obtained without specific surface preparation.

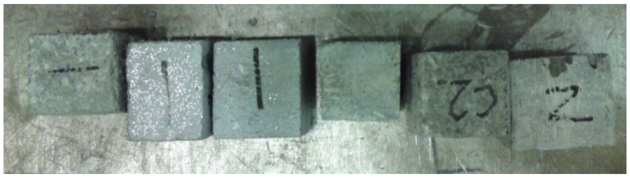

Figure 3.8 Cast Block Batches

Figure 3.9 Block Batches after Failure

The two concrete pours occurred on 11/29/2010 and 05/05/2011. The specimen age at test time was an average of 56 days. The forms for the dowel specimens needed to be very precise, particularly for the variable group containing reduced cover. However, there were some issues with several specimens in part due to mold construction as well as the flow of the cement paste during casting that resulted in several specimens with voids in the matrix. The target and realized number of specimens per group are shown in Table 3.4. Monotonic load was applied under displacement control to the center of the rebar within the notched region. An eye pin was used to apply load to the bar. Under perfect symmetry and loading, the crack formation was expected to occur along the rebar line originating at the notch and propagating back toward the supports. Details of the test setup and progression are shown in Figure 3.10.

Table 3.4 Specimen Summary

Specimen information								
Pour	Grp ID	Casting date	Test date	Specimen age upon test	Scheduled	Survived	Total scheduled	Total tested
1st	1	11/29/10	1/28/11	60 days	3	0	25	14
	2	11/29/10	1/28/11	60 days	3	3		
	3	11/29/10	1/28/11	60 days	3	3		
	4	11/29/10	1/28/11	60 days	3	0		
	5	11/29/10	1/28/11	60 days	3	2		
2nd	1	05/05/11	6/25/11	51 days	3	2		
	2	05/05/11	6/25/11	51 days	1	0		
	3	05/05/11	6/25/11	51 days	1	1		
	4	05/05/11	6/25/11	51 days	3	1		
	5	05/05/11	6/25/11	51 days	2	2		

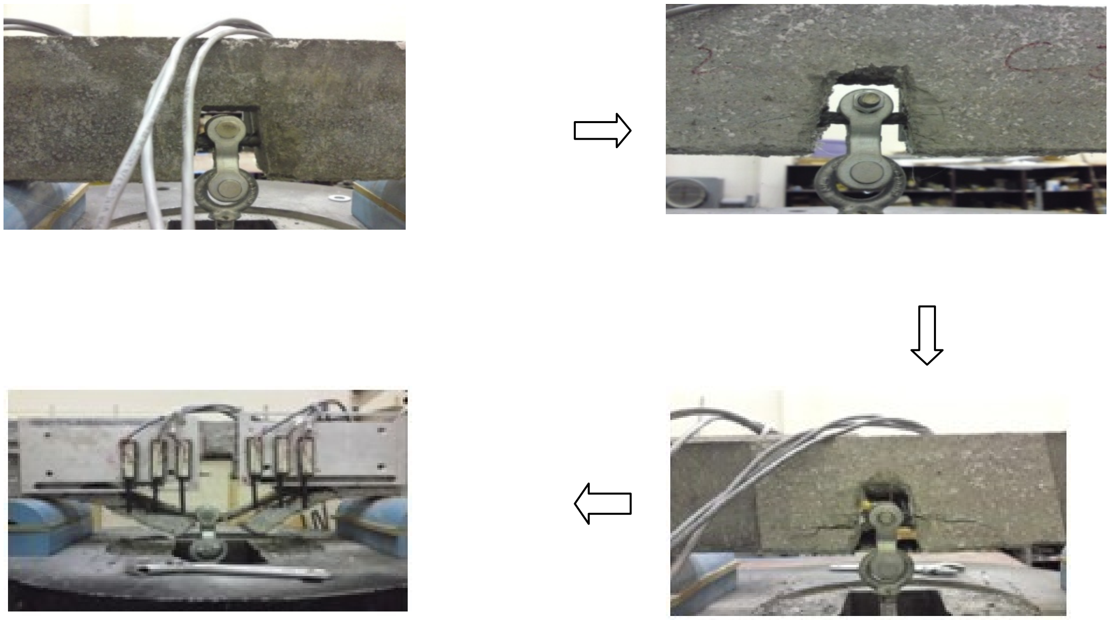

Figure 3.10 Test Procedure and Progression

The recorded load versus displacement curves are presented in the following figures. The results from groups 1 and 2 are shown in Figure 3.11, groups 3 and 4 are shown in Figure 3.12, and group 5 is shown in Figure 3.13. The low peak loads obtained, for example, from specimen 3 of group 2 were due to asymmetric loading of the bar. Therefore, cracking initiated and propagated primarily on one side of the specimen and pulled through the cover at a lower load.

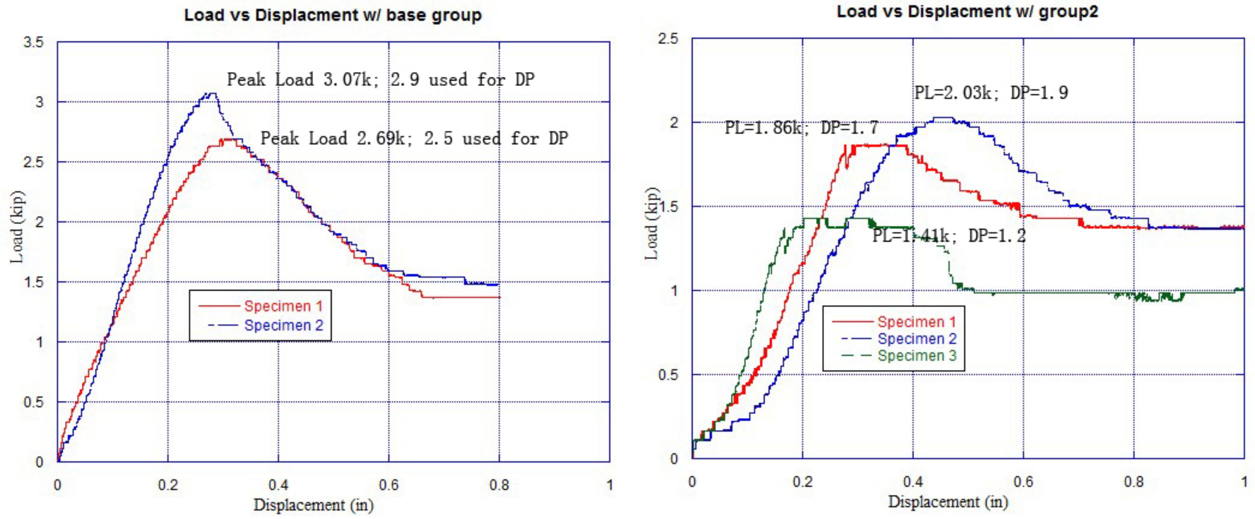

Figure 3.11 Load-Displacement Response from Tested Groups 1 and 2

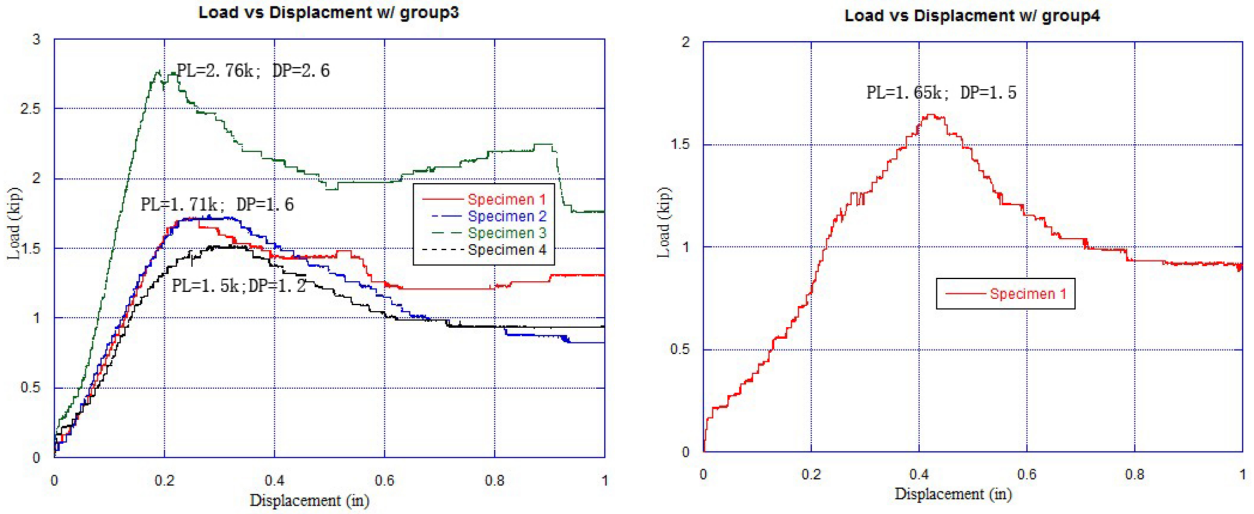

Figure 3.12 Load-Displacement Response from Tested Groups 3 and 4

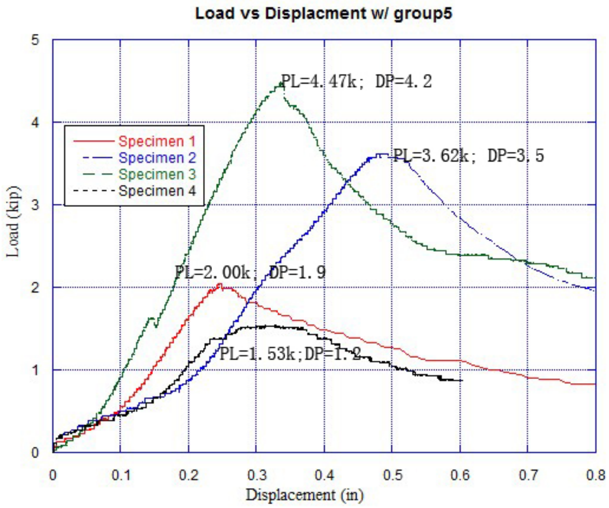

Figure 3.13 Load-Displacement Response of Tested Group 5

3.2.2 Theoretical Analysis

To obtain the concrete subgrade modulus under tensile load on the UHPC cover, the classic beam on elastic foundation (BEF) theory as shown in Figure 3.14 was considered for modeling the practical case.

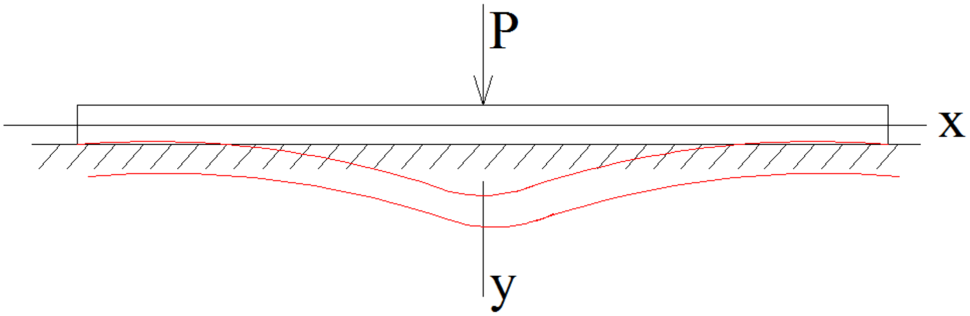

Figure 3.14 Beam on Elastic Foundation (BEF) Simplified Model

The sketched deformation of the specimen in this project is shown in Figure 3.15. Based on the free body diagram, the equilibrium equation is shown in Equation 2.

$$EI\left(\frac{dy}{dx}\right)^4 = -ky \qquad (2)$$

where E is the modulus of the steel (29,000 ksi), and I is the moment of inertia of the steel ($I = \frac{\pi r_d^4}{64}$).

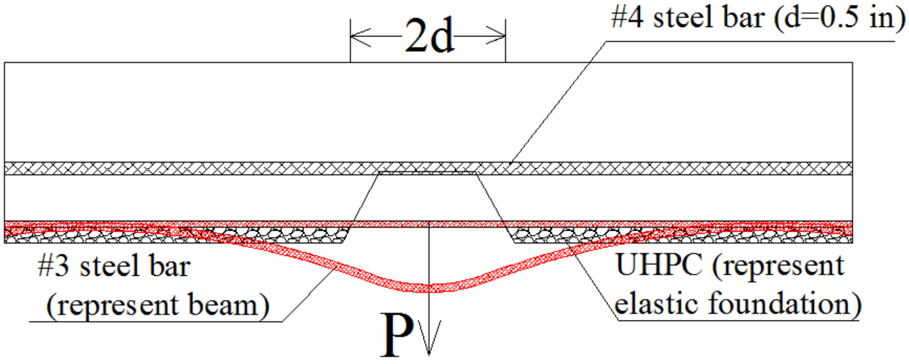

Figure 3.15 Simulated Case from BEF

The continuous support from the continuous surrounding concrete can be equivalent to multi-springs distributed as shown in Figure 3.16.

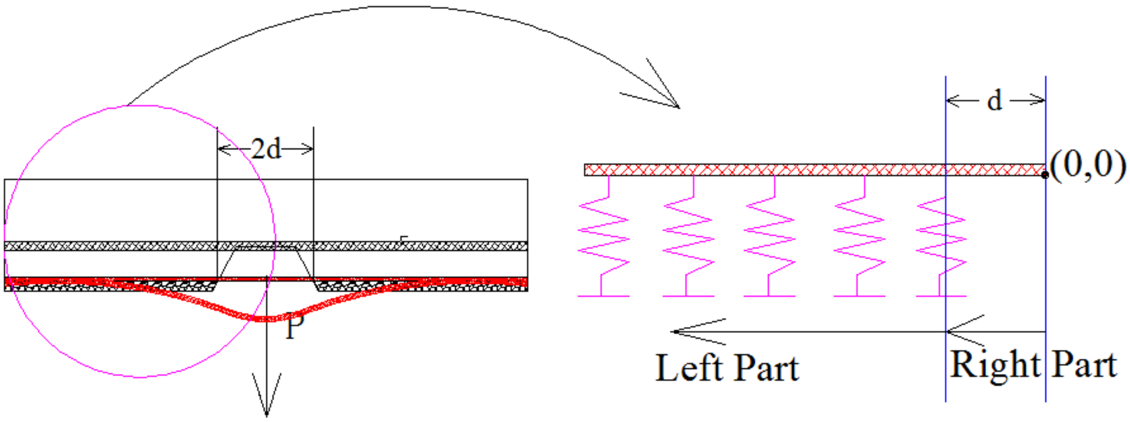

Figure 3.16 Model Explanation

For the reason of specimen design and experiment setup, a gap with length of $2d = 2$ in. was reserved in the middle of the tested beam. Hence, at that part, there is no support from concrete. Considering that, the differential equations in Equation 2 shall be expanded as shown in Equation 3:

$$\begin{cases} EI\left(\frac{dy}{dx}\right)^4 = -ky & x \in (-\infty, -d) \cup (d, \infty) \\ EI\left(\frac{dy}{dx}\right)^4 = 0 & x \in (-d, d) \end{cases} \tag{3}$$

The general solution to Equation 3 is shown in Equation 4:

$$y = \begin{cases} e^{\beta x}(c_1 \sin \beta x + c_2 \cos \beta x) + e^{-\beta x}(c_3 \sin \beta x + c_4 \cos \beta x) & x \in (-\infty, -d) \cup (d, \infty) \\ ax^3 + bx^2 + cx + d & x \in (-d, d) \end{cases} \tag{4}$$

where $\beta = \sqrt[4]{\frac{k}{4EI}}$, and all other unknown parameters are integration constants.
Considering the boundary conditions shown in Equation 5 all eight unknown constants can be solved:

$$\begin{cases} c_1 = 0 \\ c_2 = 0 \\ M_{l@x=d} = M_{r@x=d} \\ V_{l@x=d} = V_{r@x=d} \end{cases} \qquad \begin{cases} y_{l@x=d} = y_{r@x=d} \\ R_{l@x=d} = R_{r@x=d} \\ R_{r@x=0} = 0 \\ V_{r@x=0} = -\frac{P}{2} \end{cases} \tag{5}$$

The final solution to Equation 4 is shown in Equation 6, which represents the vertical displacement distribution along the reinforcement under any given load level.

$$y = \begin{cases} \frac{1}{8}\frac{1}{EI\beta^3}\{Pe^{\beta(-x+d)}[d\beta \sin(\beta x)\cos(\beta d) - \sin(\beta x)\cos(\beta d) - d\beta \sin(\beta x)\sin(\beta d) - \sin(\beta x)\sin(\beta d) \\ -d\beta \cos(\beta x)\cos(\beta d) - d\beta \cos(\beta x)\sin(\beta d) + \cos(\beta x)\sin(\beta d) - \cos(\beta x)\cos(\beta d)]\} & \mathrm{x} \in (-\infty, -\mathrm{d}) \cup (d, \infty) \\ -\frac{1}{24}\frac{P(2x^3\beta^3 - 3x^2\beta^3 d - 3x^2\beta^2 + 3\beta d + d^3\beta^3 + 3d^2\beta^2 + 3)}{EI\beta^3} & \mathrm{x} \in (-\mathrm{d}, \mathrm{d}) \end{cases} \tag{6}$$

where d is the gap length from half of the beam, $d = 1$ in., and r_d is the diameter of rebar, $r_d = 0.375$ in.

The procedure for handling the experimental data and estimate the concrete subgrade modulus using the BEF theory involves filtering the data and nonlinear regression on Equation 6. Moving average (window size of 50) was used to smooth the original data. The initial linear elastic portion of the test was extracted (between 5% and 95% of the peak load on the loading branch) to calibrate the initial subgrade modulus. Nonlinear regression was performed using Matlab®. The curve fitting function of $y(P, \beta, z)$ is obtained from Equation 6, and the results are summarized in the following Table 3.5.

Table 3.5 Numerical Result for Modulus “k” with Material Linear Consideration

Specimen group ID	Specimen number	Rows of data analyzed	Peak load (kip)	Beta value	Average beta	Modulus k value (elastic)	Average k (elastic)
1	1	5083	2.69	1.29	1.31	316	330
	2	7490	3.07	1.32		344	
2	1	28440	1.86	0.902	0.787	75	50
	2	12532	2.03	0.863		63	
	3	11763	1.41	0.597		14	
3	1	11109	1.71	0.875	1.13	66	295
	2	7000	1.71	1.23		261	
	3	6080	2.76	1.64		814	
	4	9413	1.50	0.759		37	
4	1	6403	1.65	0.857	0.857	61	61
5	1	6520	2.00	0.814	1.02	49	137
	2	11993	3.62	1.17		214	
	3	5925	4.47	1.01		117	
	4	8244	1.53	1.10		166	

*Beta value are estimated from numerical computation where load ranges (5%, 95%) of peak load

*All original data from data acquisition system (DAQ) was manually filtered prior to numerical computation

The results indicate that the side cover (due to failure in the side cover rather than bottom cover) is a critical variable that results in the largest subgrade modulus for groups 1, 3, and 5. The highest dowel loads before cracking are obtained with the stiffer dowel bar (group 5). Increasing the span length (group 2) results in lower stiffness, as would be expected. Due to the difficulty in achieving the very small side cover in group 4, only a single specimen survived. However, results indicate that both the peak loads and stiffness are likely lower than the groups with larger side cover. After obtaining β value for each group, plots showing the distributed displacement shape can be constructed as shown in Figure 3.17.

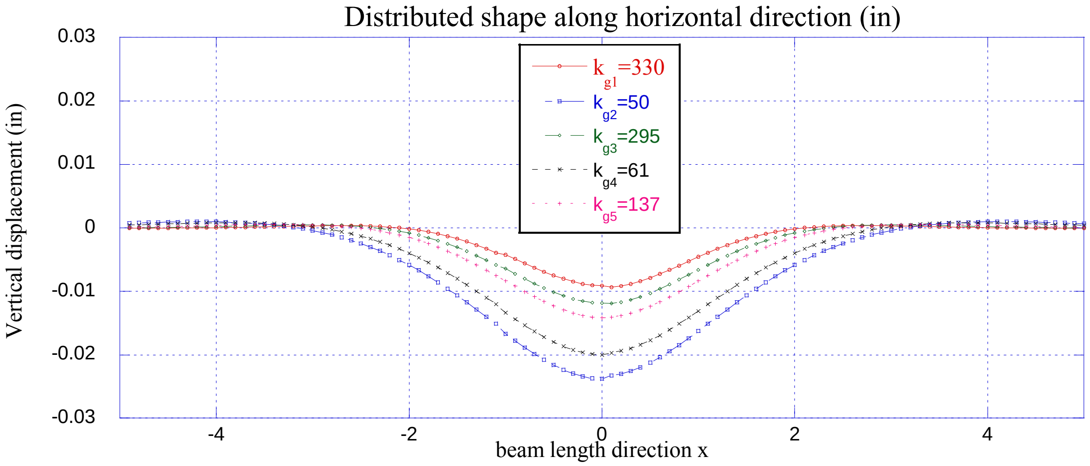

Figure 3.17 Deformed Shape with Estimated β for Each Specimen Group at $P=1k$

Some of the LVDT data at low load levels was not effective in calibrating the BEF model, because of the resolution of the LVDT (recorded values too small). Therefore, an effective lower bound of approximately 40% of the peak load was more efficient for computing the presented subgrade moduli. As observed by previous researchers (Soroushian et al. 1988), the displaced profiles predicted from BEF theory do not match the actual cover deflections after the initiation of cracking. Specifically, BEF theory predicts that the dowel bar pushes into the foundation at some distance away from the point of load application, whereas after cracking initiates, the dowel bar only pulls away from the foundation.

3.3 Uniaxial Fatigue

Concrete (and other material) fatigue loading is usually divided into two types; one is low-cycle loading, while the other is high-cycle loading (RILEM 1984), as summarized in Table 3.6. Low-cycle loading involves the application of a few load cycles at relatively high stress levels. For instance, it is used to simulate the extreme loading scenario like earthquake or wind loading. High-cycle loading is characterized by a large number of cycles at relatively low stress levels. For example, it is used to simulate the traffic loading on bridges or pavement.

Table 3.6 Fatigue Load Classes and Applications

Class	Low-cycle fatigue			High-cycle fatigue				Super high-cycle fatigue		
Cycle numbers	1	10	10^2	10^3	10^4	10^5	10^6	10^7	10^8	10^9
Applications	Structures subjected to earthquakes			Airport pavements and bridges		Highway and railway bridges, highway pavements		Mass rapid transit structures		Sea structures

To assess the structural element lifetime fatigue performance, a couple of different approaches have been adopted for testing. A widely accepted approach in the engineering field is based on the empirically derived Wholer curve, also normally called S-N diagrams. Additionally, the influence of minimum stress in the loading cycle may be represented in so-called Goodman diagrams or Smith diagrams when analyzing metals or metal related structures (Sendecky 2001). These typical curves offer a direct visual graphical representation of fatigue performance for certain loading parameters. On the other hand, another admitted approach is based on fracture mechanics concepts and has been incorporated in a finite element (FE) approach (Reinhardt et al. 1986 and Hordijk 1991).

The conventional testing methods used to identify concrete fatigue properties are fatigue compression test, tensile test, and flexural test, the latter typically used in previous tests on fiber-reinforced concrete. Concrete is a heterogeneous material that is inherently full of flaws, such as pores, air voids, lenses of bleed water, and shrinkage cracks. From previous literature (Gao and Hsu 1998), the fatigue failure mechanism in concrete can be divided into three distinct stages. The 1st stage involves the weak regions within the concrete and is termed flaw initiation. The 2nd stage is characterized by slow and progressive growth of the inherent flaws to a critical size known as microcracking. The 3rd stage is when a sufficient number of unstable cracks have formed that will continue to enlarge and eventually lead to failure. Sometimes the 3 stages are summarized as 2 parts (Horii et al. 1992 and Kolluru et al. 2000) that are called the deceleration stage and acceleration stage. The rate of crack growth decreases as the crack grows in the deceleration stage while there is a steady increase in the crack growth rate right up to failure in the acceleration stage.

Most studies on the behavior of concrete under cyclic load in the past dealt with normal concrete under different loading arrangement (compression, tension, and bending). For structural materials, a majority of fatigue studies are performed via flexural tests. To a lesser extent, fatigue tests of concrete under compressive load have also been performed, while the tests under alternating uniaxial tension-compression are extremely limited. Many structures are subjected to loading reversals under live load; therefore it is necessary to focus on the fatigue behavior of concrete under this type of loading.

In recent years, an increasing number of researchers have examined the fatigue characteristic of concrete in tension (Saito 1987, Cornelissen 1984, and Zhang et al. 2000) due to the introduction of nonlinear fracture mechanics widely accepted in the analysis of concrete. Moreover, some researchers have also studied the effects of combined stresses on the fatigue performance of concrete. It has been found that the fatigue strength of concrete in biaxial compression is greater than that under uniaxial compression (Su and Hsu 1988 and Yin and Hsu 1995).

Because of the widespread use of fiber reinforced concrete (FRC), many studies have been done on the fatigue behavior of this material. The fatigue behavior of steel fiber reinforced concrete (SFRC) under uniaxial and biaxial compression was investigated by Yin and Hsu (1995). They tested seventy-two steel reinforced concrete specimens with different volume percent of fiber under compression fatigue loading. They observed the presence of the fibers enhances the concrete ductility and changes the modes of failure from splitting to faulting-type. Fiber content is the first important factor that influences the fatigue performance of fiber reinforced concrete, while the aspect ratio and type of fiber is the second factor in importance (Johnston and Zemp 1991 and Naaman and Hammoud 1998).

Recently, ultra-high performance concrete (UHPC) has been increasingly used in structural applications with special performance needs. However, very little is known of the fatigue and cyclic behavior of this type of cementitious material. Lappa et al. (2004) studied the flexural behavior of UHPC. They tested steel fiber reinforced UHPC beams with four-point bending at a 750 mm span. They assumed the value of upper load level and then corrected this value by using the remaining beam after test and the image analysis method. They concluded with this method of correction, it is possible to estimate the actual material strength. Fitik et al. (2008) studied the fatigue behavior of UHPC under cyclic stress reversal loading. The test included some important factors like stress level, stress range, and fiber addition. The deformation measurement of their results showed that UHPC can be divided into three stages as known for the normal and high strength concrete.

A series of flexural fatigue load tests on Ductal® were performed and demonstrated the material properties recommended for design by the French code is on the safe side. The specimens were loaded up to 90% of the first crack strength for 106 cycles. After 1 million cycles, no sign of degradation was observed. No description of reversal loading was found (Behloul et al. 2005). For high performance fiber-reinforced concrete (HPFRC), quasi-static flexural strength fatigue tests on notched beams were performed under third point bending. It was found that fiber number across the section is not the only factor govern the flexural fatigue behavior. Regarding the fatigue crack growth, two distinct stages were found, in the first stage, the rate of crack opening is decelerated while the second stage, it is accelerated. As the deflection under fatigue loading is much larger than that for static loading, the failure criterion based on deflection is not suitable (Kolluru et al. 2000).

From summarizing the literature, it was found that for regular fiber-reinforced concrete (FRC), 1) fiber content is the most important factor on the fatigue performance enhancement. But the fibers are more effective to enhance the flexural fatigue behavior while has less or even no contribution on the compressive fatigue behavior. 2) Fiber count is not the only factor determining the fatigue behavior under the same load level. 3) The S-N curve is often a good indication for fatigue analysis. 4) The Japan designers recommend a 50% of the material strength as the fatigue limit loading. 5) The concrete suffers fatigue during pre-crack fatigue behavior while the fiber and interface suffers during the post-crack behavior. 6) The S-N curve for normal FRC is linear.

3.3.1 Experimental Work

The fatigue tests on UHPC were performed to address several questions regarding the fatigue behavior of UHPC. Specifically, a majority of previous concrete fatigue tests are compression only or tension only (in the case of FRC), and do not necessarily address the interaction between cycles of compression and tension. The typical notion of stress life presented in S-N curve format may not be appropriate considering the different tension and compression capacities and behaviors of UHPC. It was anticipated that several differences with fatigue behavior of FRC would be observed, but that use of a stress ratio (or strain ratio) quantity may lead to a bilinear S-N curve. To better control that state of stress within the cross-section, a uniaxial fatigue setup was selected, as shown in Figure 3.18.

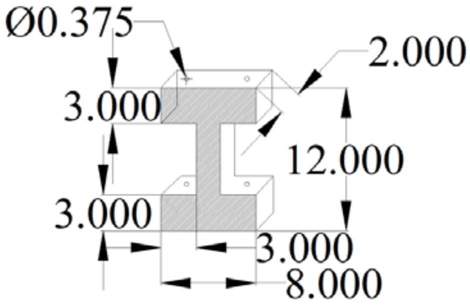

Figure 3.18 Uniaxial Fatigue "I-beam" Specimen Dimensions

Smoothed wooden forms were used to better control the tolerances needed to align the attachment points on the specimens. PVC ducts (3/8” diameter) were attached to the forms to allow through rods for attachment of the flanges on both sides of the web (top and bottom). The forms and casting of the specimens are shown with the final specimens in Figure . Specimens were cast on 05/05/2011 (at the same time as some of the dowel action specimens). A total of 16 specimens were initially cast, 14 of which were useable. The remaining two did not fill the molds entirely primarily due to the spacing between the PVC pipes and the edge of molds relative to the fiber length.

Figure 3.19 Fatigue Specimens during and after Casting

The designed UHPC specimens were connected using high strength bolts through the bottom flange to a W24x146 steel beam attached to the strong floor (Figure). High strength bolts were also used to connect the top flange to an especially machined steel box attached to the MTS (material testing system) crosshead, as shown in Figure 3.21. A significant amount of calibration was performed using neoprene pads and steel plates inserted between the box and the top of the UHPC specimen to optimize the uniaxial effect of the load (which ultimately proved difficult to achieve).

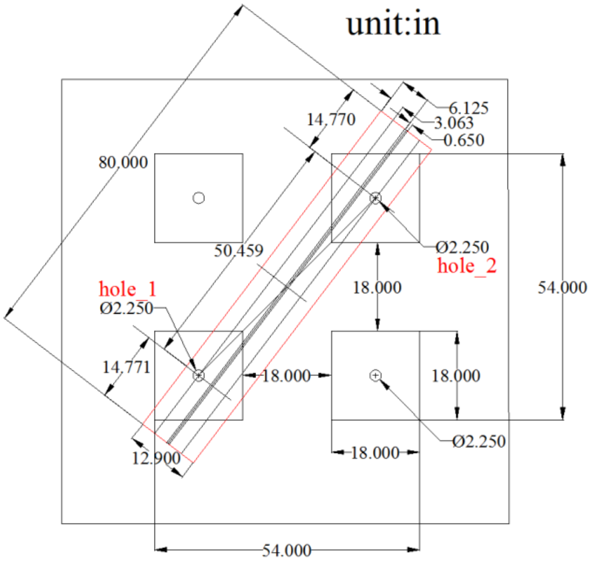

Figure 3.20 Connection of Steel Wide Flange Section to Strong Floor

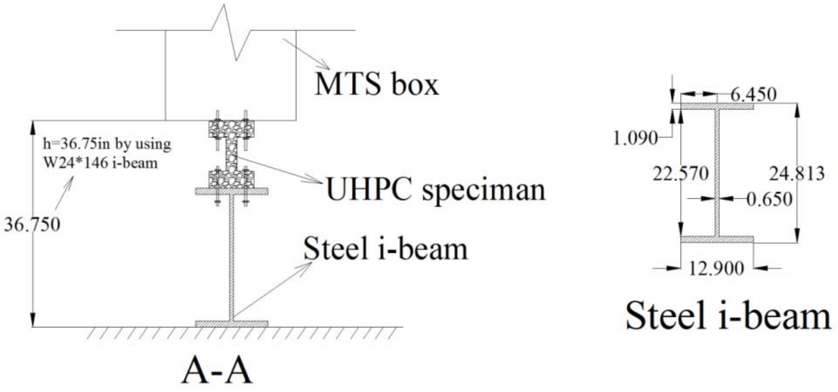

Figure 3.21 Connection of UHPC Specimen to Test Setup

Concrete compressive strength information was obtained from the same cubes taken with the dowel action specimens. The specimens had an average compressive strength at the time of testing of 18 ksi, with an expected value of 20 ksi. The approximate specimen age upon testing was 210 days (varies based on specimen number tested). During the test, a cyclic vertical compression and tension was applied to specimens under load control. All cyclic tests were performed at a rate of 2 Hz. The compressive stress was kept constant between all specimens; however, the tensile stress was varied. Higher tensile loads (relative to the expected tensile strength) were selected to decrease the total number of cycles necessary to fail the specimens. The testing matrix indicating the actual achieved stress levels is shown in Table 3.7. The specimens not shown in the matrix were used for monotonic tension/compression testing or were not tested to failure due to cracks that formed outside the web of the UHPC specimen.

Table 3.7 Specimen Testing Matrix with Achieved Stress Ranges

Cross section (in^2)	Specimen	Achieved load in kip (percent of critical)		No. of cycles to failure
		Tension*	Compression**	
2x2	Sp0	1.0 (17%) & 2.5 (42%)	10 (13%)	49,300
	Sp1	2.4 (40%)	15 (20%)	67,000
	Sp2	2.1 (35%)	15 (20%)	142,700
	Sp3	2 (33%)	15 (20%)	2,534,000
	Sp4	4.3(70%)	15(20%)	80
	Sp5	3.3 (55%)	15 (20%)	13,800
	Sp6	3.0 (50%)	15 (20%)	5,000
	Sp7	2.3 (38%)	15 (20%)	10,000
	Sp8	2.8 (47%)	15 (20%)	53,000
	Sp9	This specimen was tested monotonically		N/A

*A critical UHPC compression stress of $\sigma_C = 20$ ksi was used for calculation;

**A critical UHPC compression stress of $\sigma_T = 1.5$ ksi was used for calculation;

Foil-backed resistance gauges were mounted on each of the four faces of the specimen webs. A sample load time history (Figure 3.22) and strain time history (Figure 3.23) are presented for specimen 3 (Sp3) between cycles 100,000 and 100,010. The asymmetric tension/compression load was maintained until tensile cracks developed in the specimens and the achieved tension force dropped to zero. However, eccentricities developed during the tests that allowed some moment to be imparted to the specimen during the compression cycle. This curvature within the web resulted in considerably higher tensile strains on one or more faces of the specimen. Therefore, the number of cycles before the target tensile load was not met was lower than in a pure uniaxial stress state.

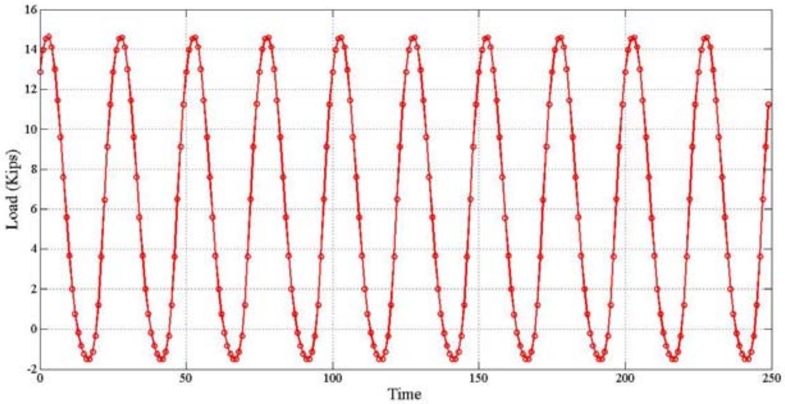

Figure 3.22 Ten Load Cycles (at 100,000th Cycle) for Specimen SP3

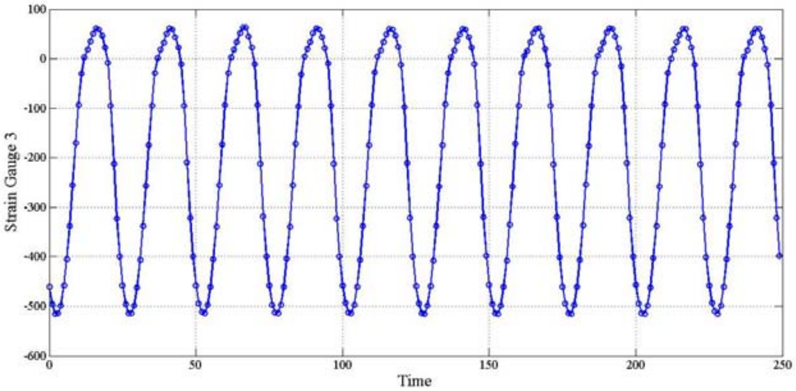

Figure 3.23 Ten Strain Cycles (at 100,000th Cycle) for Specimen SP3

Table 3.8 summarizes the maximum tensile and compressive strains measured by each of the four strain gages for the specimens tested under fatigue loading. Several strain gages were lost during testing as tensile cracks formed in the webs. Therefore, the actual peak tensile strains achieved in the specimens were likely higher. In addition, due to eccentricities in the loading, the peak tensile strain measured in some gages was higher than the strain corresponding to the mean tension stress on the cross section, which contributed to failure at lower cycle numbers for several of the specimens.

Table 3.8 Peak Tensile and Compressive Strain Values Recorded during Cyclic Loading

Micro-strain	Specimen							
	Sp0	Sp1	Sp2	Sp3	Sp5	Sp6	Sp7	Sp8
Tension		1227	1679	150	120	181	412	131
Compression		-579	-886	-611	-655	-697	-612	-564

Specimen 0 was initially tested under a 1 kip tension load and 10 kip compression load while evaluating response of the experimental setup. After 19,300 cycles, the test was stopped for inspection of the specimen and setup, with no indication of cracks in the specimen. The load level was then increased to 2.5 kip in tension and failed after 30,000 at this new load level. Specimen 1 did not fail across the center of the UHPC cross section, but rather in the flange portion due to the pre-tensioning force applied to equalize the strains on the cross section. Specimen SP2 ultimately failed as expected with a crack perpendicular to the axis of the member at the center of the gage length. Strain gage 2 indicates tensile strains in excess of 1000 με that correspond to the cracking load of UHPC in tension. Several photos illustrate the final cracked state of Specimen SP2 in Figure 3.24.

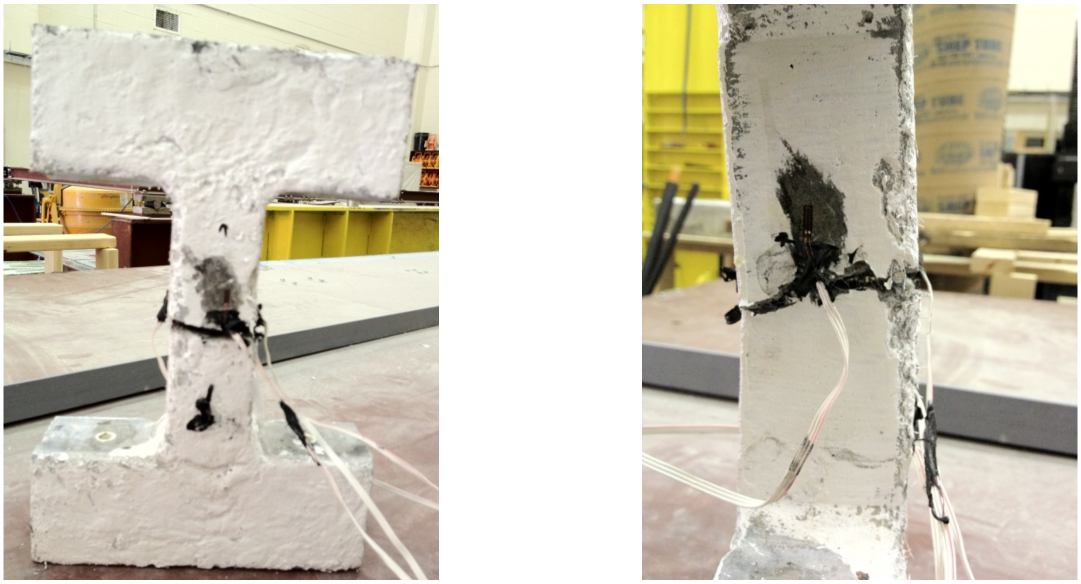

Figure 3.24 Failure of Specimen SP2 after Cycling

Specimen 3 was the only specimen that exhibited consistent compression and tension strains during cycling over the full number of cycles. Figure 3.25 shows the maximum tensile strain readings every 1000 cycles for Specimen 3 (Sp3). Similarly, the maximum compressive strain readings are shown in Figure 3.26. The jump in the SG1 reading around cycle 200,000 occurred due to loosening of the tie-down bolts between the steel wide flange and the strong floor. The test was stopped after approximately 2500000 cycles and the specimen was monotonically tested to failure. The residual tension strength of the specimen after this number of cycles was 4.7 kip.

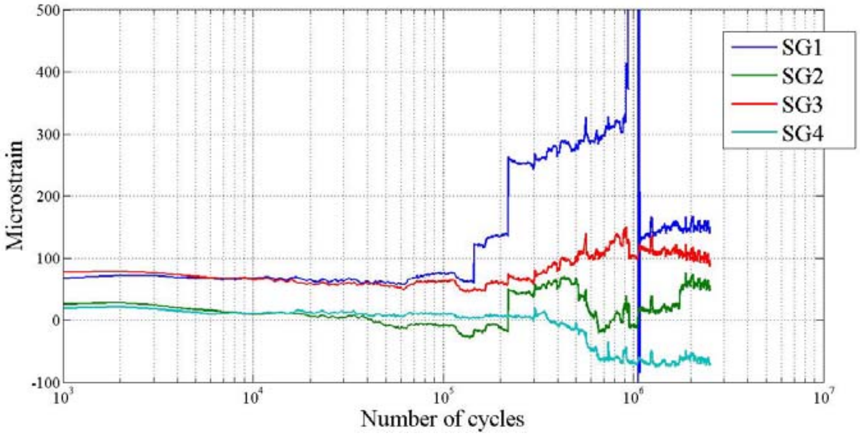

Figure 3.25 Peak Tensile Strains in Specimen SP3

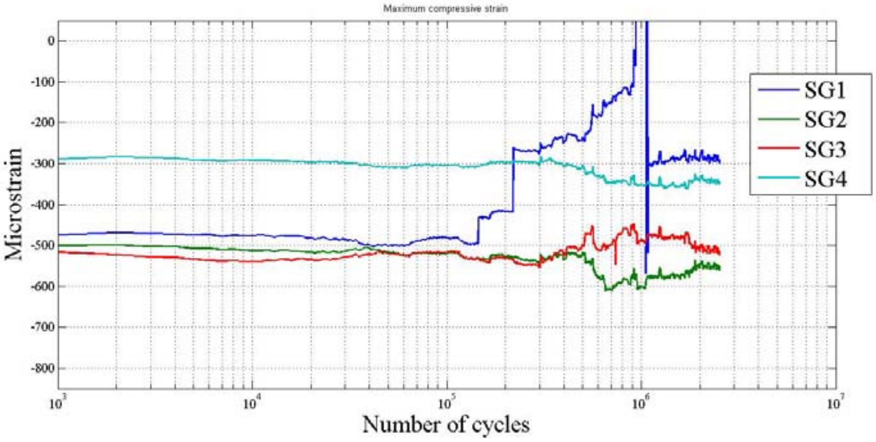

Figure 3.26 Peak Compressive Strains in Specimen SP3

Specimen SP4 was tested under higher tensile load level (4.25 kips) and it was stopped after only 80 cycles due to an early crack that continued to open rapidly. Specimens SP5, 6, 7, and 8 all failed with a single widening crack perpendicular to the axis of the member. The first visible crack for these specimens occurred around the 500th cycle and continued to open as the cycles progressed to failure. Specimen SP9 was tested monotonically under displacement control with a rate of 0.02 in/min and the maximum tensile load was 4.45 kips. Significantly unbalanced tension strains were seen on one face of the specimen as the load approached 4 kip.

3.3.2 Analytical Work

Generally three methods are used to analyze and calculate the fatigue life for all materials. These methods used for calculating the fatigue life are; stress-life approach, strain-life approach, and fracture mechanism approach. Each method has its area of application but there are commonalities among them. A majority of stress-life or strain-life material curves are generated using constant amplitude testing to failure. However, due to the eccentricities encountered in these tests, both the stresses and strains were variable amplitude during the course of the cyclic tests. The peak tensile strain data from the available strain gage recordings for each specimen are used in this section to produce a rough estimate of the strain-life behavior of the UHPC specimens.

Several assumptions were made, specifically that a linear damage rule was appropriate, only the tension cycling contributed to damage, and there is only a single (log) linear branch in the strain-life curve. This typical linear damage rule was proposed by Palmgren, and later modified by Miner, hence and it is commonly referred to as the Palmgren-Miner rule (Stephens et al. 2001). Based on this rule, the damage caused by a certain stress or strain level is defined as:

$$D_i = \frac{n_i}{n_{f_i}} \tag{7}$$

Where n_i is the number of (full) cycles of the stress or strain level applied, and n_{f_i} is the fatigue life for the same level of loading. Therefore, the total cumulative damage caused by variable amplitude loading will be:

$$\sum_i \frac{n_i}{n_{f_i}} = 1 \tag{8}$$

A traditional model of fatigue life (Basquin Equation) was adopted to calculate the fatigue life for each amplitude:

$$S_{N_f} = \sigma_f'\left(2N_f\right)^b \tag{9}$$

Where S_{N_f} is the stress corresponding to the fatigue life N_f (number of half cycles to failure), and and b are material constants. As the data recorded was strain based, the strain version of Equation 9 was used, which is commonly referred to as the Coffin-Manson relation, with corresponding strain terms E_{N_f} and ε_f'. In addition, the tension cycles were non-symmetric; therefore, a correction was included to account for the mean strain on the strain-life behavior of material. Some models have been derived to consider the effect of the mean stress or strain. The Goodman modified equation was used in the correction of the strain amplitude:

$$\frac{E_a}{E_{N_f}} + \frac{E_m}{E_u} = 1 \tag{10}$$

where E_m is the mean strain or stress = $\frac{1}{2}\left(\varepsilon_{\max} + \varepsilon_{\min}\right)$, E_a is the strain or stress amplitude = $\frac{1}{2}\left(\varepsilon_{\max} - \varepsilon_{\min}\right)$, and E_u is the ultimate strain. It was assumed that the ultimate strain coincided with the strain corresponding to σ_f'. A numerical value of 4000 με was used for calculation purposes and corresponds to the 0.3% tension strain used for UHPC constitutive modeling (but is not the tensile rupture strain).

Based on Equation 8, the material constant b was determined by summing the damage at each strain amplitude until failure occurred in each specimen. Based on the average lower bound (corresponding to strain gages with higher tensile strains) of several calculations, the material constant b was found to be = -0.18. Figure 3.27 shows the resulting strain life curve, based on the assumptions mentioned, for UHPC specimens tested. Using the curve, it is quickly evident that the fatigue life under a uniaxial tension strain of 150 με (such as for Sp3) would be >5e7 cycles, which would exceed the measured number of cycles in Sp3. However, when correcting for the mean strain (tension and compression cycling), the predicted life (considering SG3) drops to 2e6 cycles. It can be concluded that the calibrated b values are better representations of the strain behavior in the high amplitude, low cycle region, whereas the material likely exhibits a different degradation rate in the low amplitude, high cycle region that was not populated in these tests.

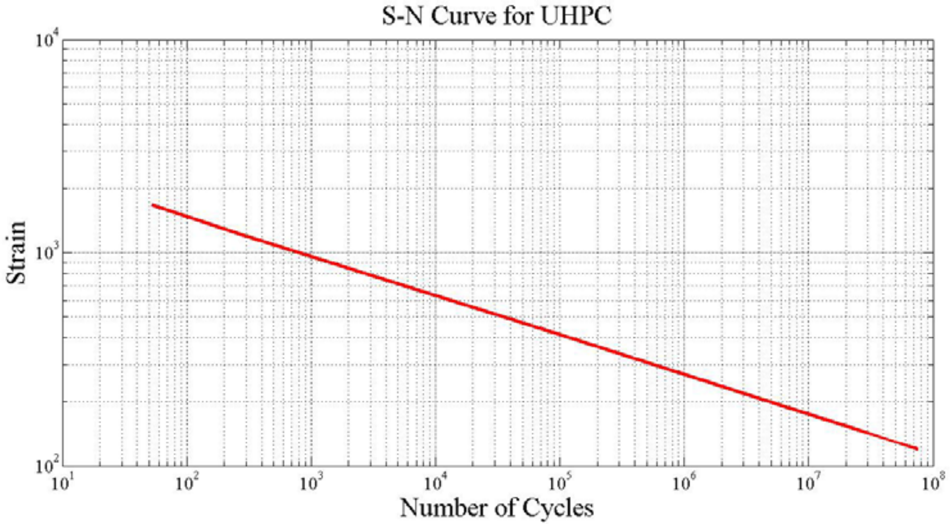

Figure 3.27 Approximate Strain-Life Curve Proposed from Tests

3.4 Conclusions

With the data recorded from the dowel test, it is obvious that even for a #3 bar, the dowel force can reach up to 3 kip, corresponding to the designated specimen. Hence, dowel action provides a reasonably high contribution to shear resistance that should not be ignored when applied to UHPC related structures without web reinforcement. In addition, some other parameters, such as bottom cover thickness, side cover thickness, dowel bar size as well as the beam length, also influence the dowel action performance. With additional testing, an empirical expression based on these variables can be developed similar to those available for NSC.

It was shown that the BEF theory is applicable to investigation of dowel action against UHPC cover, particularly in the initial elastic portion of the responses. Moreover, the BEF sub-grade moduli were calibrated based on the data obtained from the experiments. To better capture the peak loading and behavior of the fibers bridging the cracks, a beam on nonlinear foundation model is needed, or an alternative theory based on beam traditional flexural theory. However, this phenomenon requires more investigation in the future, because the UHPC beams considered do not contain transverse reinforcement. Therefore, it is not clear what mechanism provides support for the cover that is deforming. Once the concrete sub-grade modulus calibrated, it can be used for simulation purposes in a FEM model, which can provide guidance on optimal design based on the observed shear failure mode of the UHPC-HSS specimens. Such a model can also be used (1) to compare with the situation without considering dowel action, and (2) to analyze if the dowel bar connection approach is a viable approach for deck-to-deck connections.

Furthermore, the uniaxial fatigue behavior of UHPC was investigated by testing sixteen UHPC specimens under cyclic vertical compression and tension. The test setup, size of the specimens, and the required load levels made it difficult to control eccentricity of load on the cross section. Therefore, tensile cracks opened earlier on one face of the specimen and resulted in failure at lower cycle numbers than would have occurred under a purely uniaxial stress state. However, a well-balanced specimen was able to achieve $2.5\text{x}10^6$ cycles without failure. After a monotonic strength test, the specimen lost only approximately 20% of its static capacity. Using the variable amplitude strain data and assumptions regarding the form of the stain-life curve, it was possible to predict the material constants governing the Coffin-Manson relation for UHPC. However, due to the variability in strains in the cross section of each specimen and the high load amplitude testing, more testing should be carried out before extrapolating the predictions to the high cycle regime.

Chapter-4

FRP Bridge Deck

4.1 Introduction

The application of fiber-reinforced polymers (FRPs) in bridge construction has grown rapidly in the last two decades, in part due to their potential to ease and accelerate the construction, extend service life, and improve performance of the bridge. Excellent properties of FRP materials including high strength-to-weight and stiffness-to-weight ratios, long-term durability, and good corrosion and fatigue resistance make them promising alternatives to conventional construction materials (Ehlen 1999, Mertz et al. 2003, and Zhang et al. 2006). FRP composites were first used in retrofit and repair applications in the form of fabrics, laminates, and shells. They improve shear and flexural strengths of structural components as well as the column confinement (Mertz et al. 2003 and Mirmiran et al. 2004). FRP has also been used as reinforcing bars, prestressing strands, and pultruded profiles in new construction. FRP bridge deck is another application of FRP materials, which allows for accelerated replacement and new construction in bridges (Bakis et al. 2001). An FRP bridge deck weighs approximately 80% less than a concrete deck (Mu et al. 2006). The lightweight FRP deck could be especially beneficial for movable bridges, where spans have to be lifted up for the passage of vessels.

FRP decks are generally made using three manufacturing methods: vacuum-assisted-resin-transfer-molding (VARTM), open mold hand layup, and pultrusion. Three deck systems which are made using these manufacturing methods are shown in Figure 4.1 (O'Connor and Hooks 2003).

Currently, there are several commercially available FRP deck systems such as TYCOR deck from 3TEX, DuraSpan deck from Martin Marietta Composites, Superdeck from Creative Pultrusions, Kansas Structural Composites deck, TeckDeck from Fiber-Reinforced Systems, and ZellComp deck. Due to proprietary design and manufacturing methods of FRP decks, their design guidelines and specifications are often performance-based.

Several studies have been carried out on different FRP deck systems and their connections to characterize their static and dynamic performance. Connections of FRP decks were studied by Keller and Gurtler (2005), Righman et al. (2004), and Davalos et al. (2011). Material constituents and mechanical properties were investigated by Davalos et al. (2001) and Alagusundaramoorthy et al. (2006). Deflection and deformation, ultimate capacity, and failure mode were studied by Wu et al. (2003), Kumar et al (2004), and Davalos and Chen (2005). Creep and fatigue in FRP decks were investigated by Scott et al. (1995), Cole et al. (2006), and

Alnahhal et al. (2006). Wu, Mirmiran and Swanson (2004) studied the fatigue behavior of a prestressed tubular bridge deck made of FRP tubes.

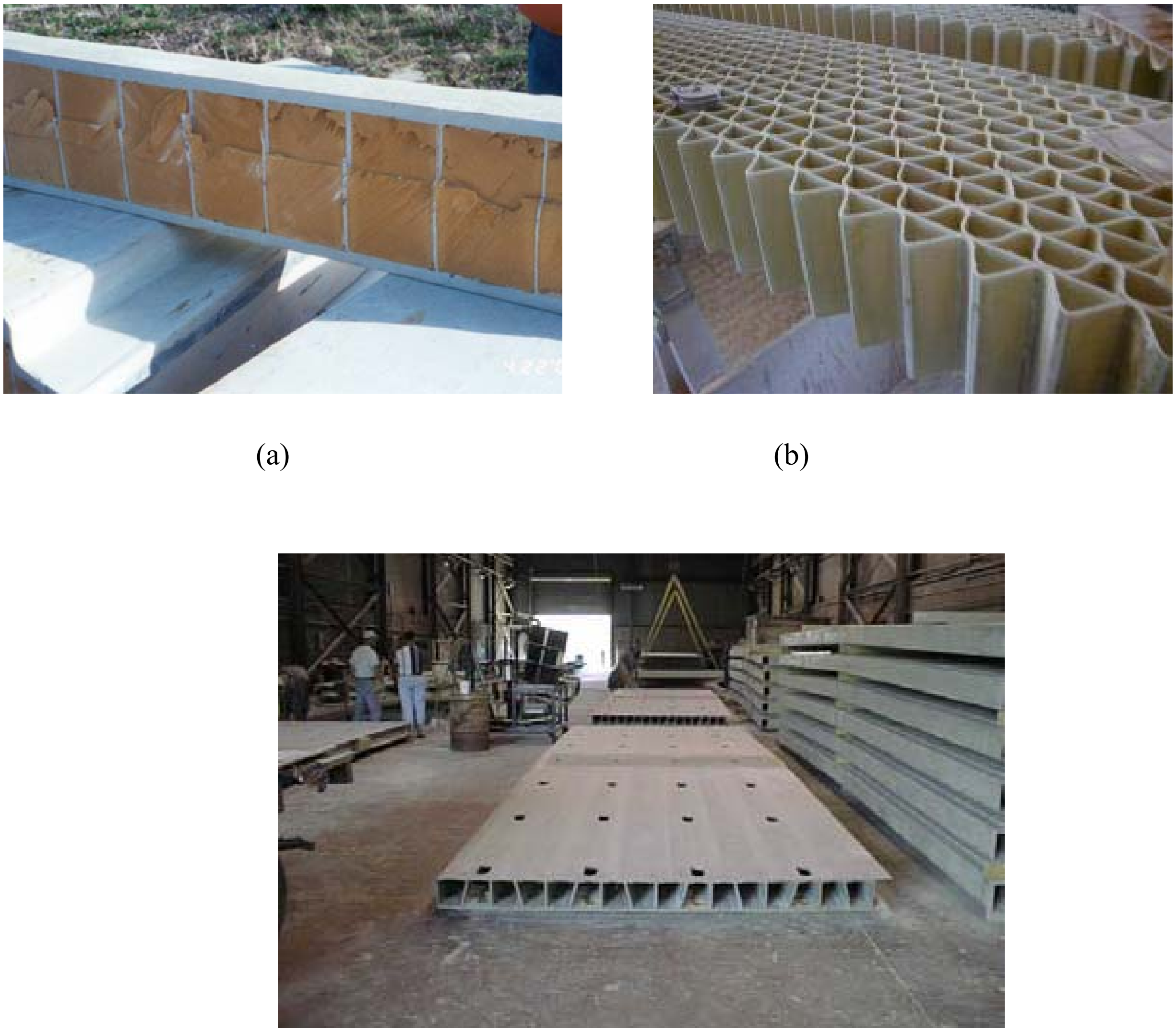

(a)

(b)

(c)

Figure 4.1 FRP Deck Systems Made Using: (a) VARTM; (b) Open Mold Hand Lay-up; and (c) Pultrusion Manufacturing Methods (O'Connor and Hooks 2003)

During the past decade, over 40 FRP bridge decks have been installed on existing or new bridges in the US. These bridges are located in California, Delaware, Florida, Idaho, Illinois, Iowa, Kansas, Maryland, Missouri, New York, North Carolina, South Carolina, Ohio, Oregon, Pennsylvania, Virginia, West Virginia, and Wisconsin.

In this part of the project, an FRP deck product made by Structural Composites Inc. of Melbourne, FL, was tested under static and fatigue loading. This FRP bridge deck system is 4.6 in. thick, and is composed of top and bottom glass FRP (GFRP) face sheets (four longitudinal and four transverse layers) and a core layer made of trapezoidal foam sections and four layers diagonal (shear) GFRP sheets (see Figure 4.2), all laminated together using VARTM. The mechanical properties of the GFRP layers used in each direction are presented in Table 4.1. The manufacturing process of a scaled FRP bridge deck is shown in Figure 4.3. Figure 4.4 shows the cross-section and the elevation view of the FRP deck system which was tested in this study.

The FRP bridge deck system was first subjected to a static load up to a target service load, as specified in the next section, to determine its serviceability. The specimen was then unloaded, and subsequently tested under repeated cyclic (fatigue) loading. Finally, the residual strength of the specimen was evaluated by loading it statically up to failure. The experimental program as well as the test results and discussions are provided in the following sections.

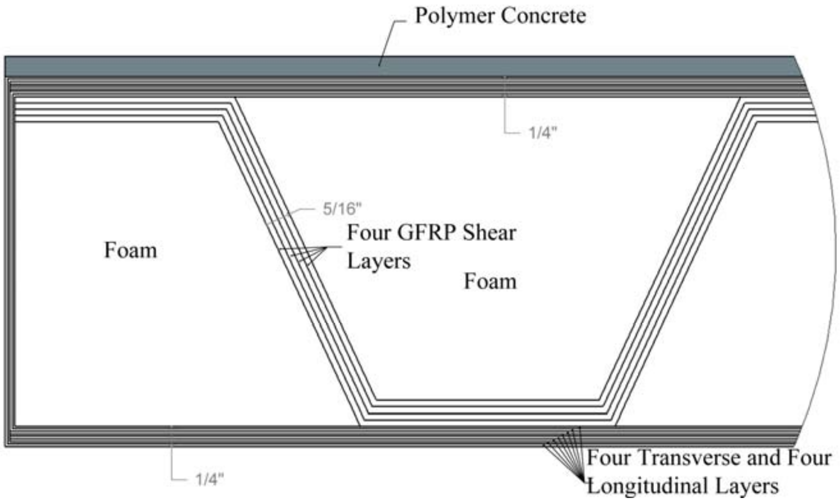

Figure 4.2 Components of The FRP Bridge Deck (Courtesy of Structural Composites Inc.)

Table 4.1 Mechanical Properties of GFRP Layers (Courtesy of Structural Composites Inc.)

Direction	Tensile Strength (ksi)	Modulus of Elasticity (Msi)
Transverse and Longitudinal	61	3.7
Diagonal (Shear)	46	2.79

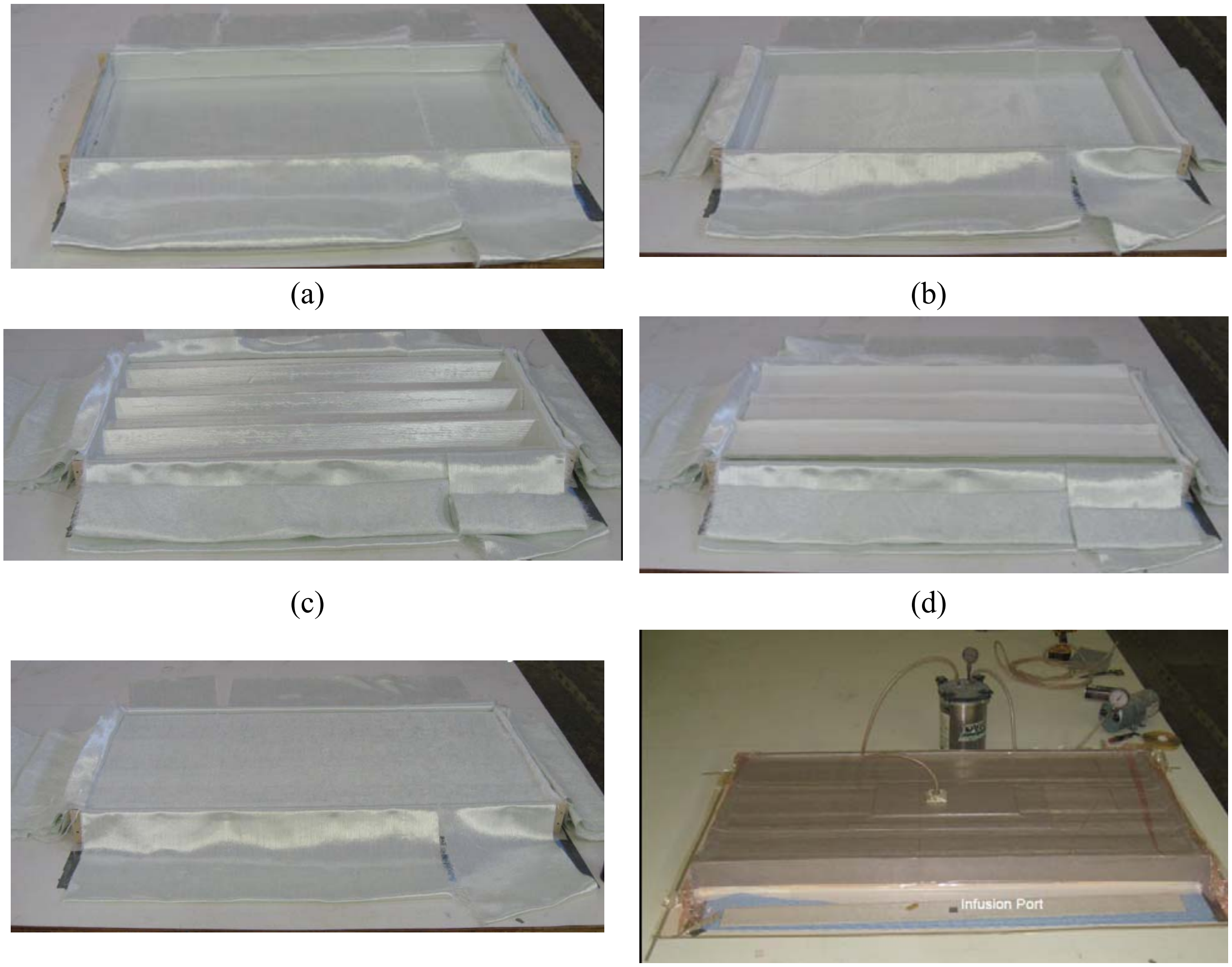

(a) (b)

(c) (d)

(e) (f)

Figure 4.3 Manufacturing Process of a Scaled FRP Bridge Deck: (a) Laying Transverse Layers; (b) Laying Longitudinal Layers; (c) Installing Bottom Foams; (d) Laying Shear Layers and Installing Top Foams; (e) Folding Transverse and Longitudinal Layers; and (f) VARTM Process (Courtesy of Structural Composites Inc.)

(a) (b)

Figure 4.4 Tested FRP Deck System: (a) Cross-Section and (b) Elevation View

4.2 Experimental Program

4.2.1 Test Setup

The FRP bridge deck specimen, loading configuration, and FRP deck-steel girder connection details are shown schematically in Figure 4.5. The two-span specimen had a 5-ft center-to-center (c/c) spacing between the supporting steel girders (see Figure 4.5 (a)). For the initial static and fatigue tests, the specimen was loaded simultaneously at the middle of each span, while it was loaded only at the south mid-span during the residual strength test. Loads were applied on an AASHTO prescribed footprint of 20 x 10 in. for an HS 20 truck dual-tire wheel, using a neoprene pad with a steel plate on top and with the longer side oriented perpendicular to the traffic. The distance between the two loading pads was 5 ft (see Figure 4.5 (b)), which is more critical than the standard wheel base of 6 ft for an HS truck. Shear studs with a diameter of 3/4 in. and a height of 3.5 in. were welded onto the top flange of the girders. Slots were created at appropriate locations in the FRP deck specimen to be filled later with epoxy to fully encase the studs (see Figure 4.5 (d)). The epoxy fill was Sikadur 31, Hi-Mod Gel, made by Sika Corp. of Lyndhurst, NJ. The test setups for the initial static and fatigue tests and residual strength test are shown in Figure 4.6.

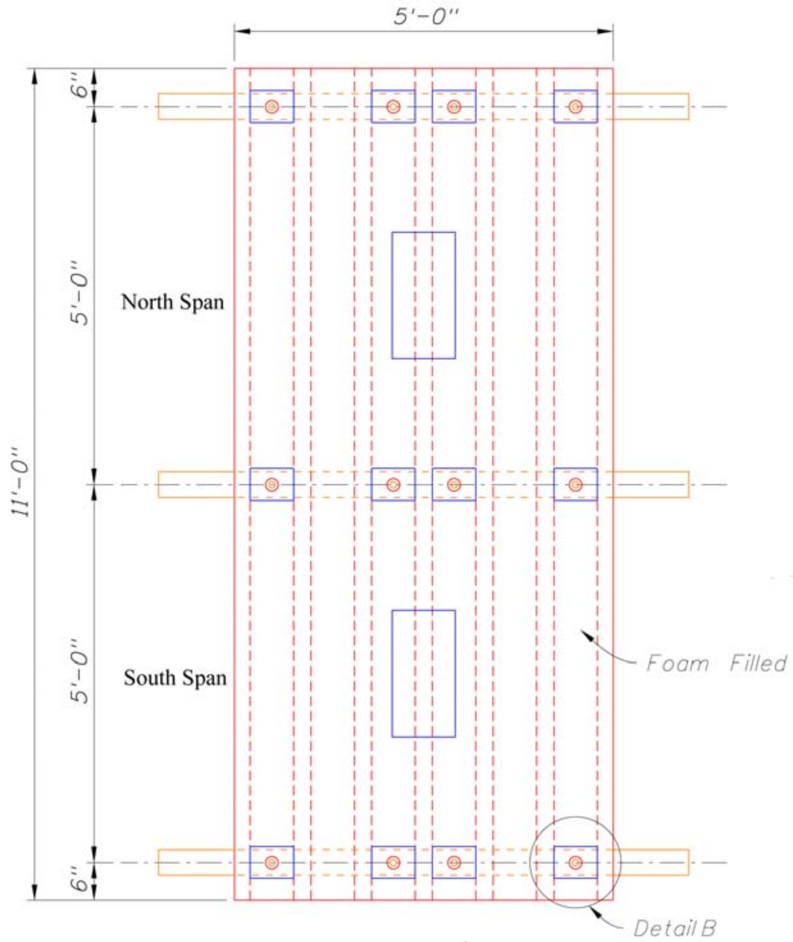

(a)

Figure 4.5 Layout of the FRP Bridge Deck Specimen: (a) Plan View

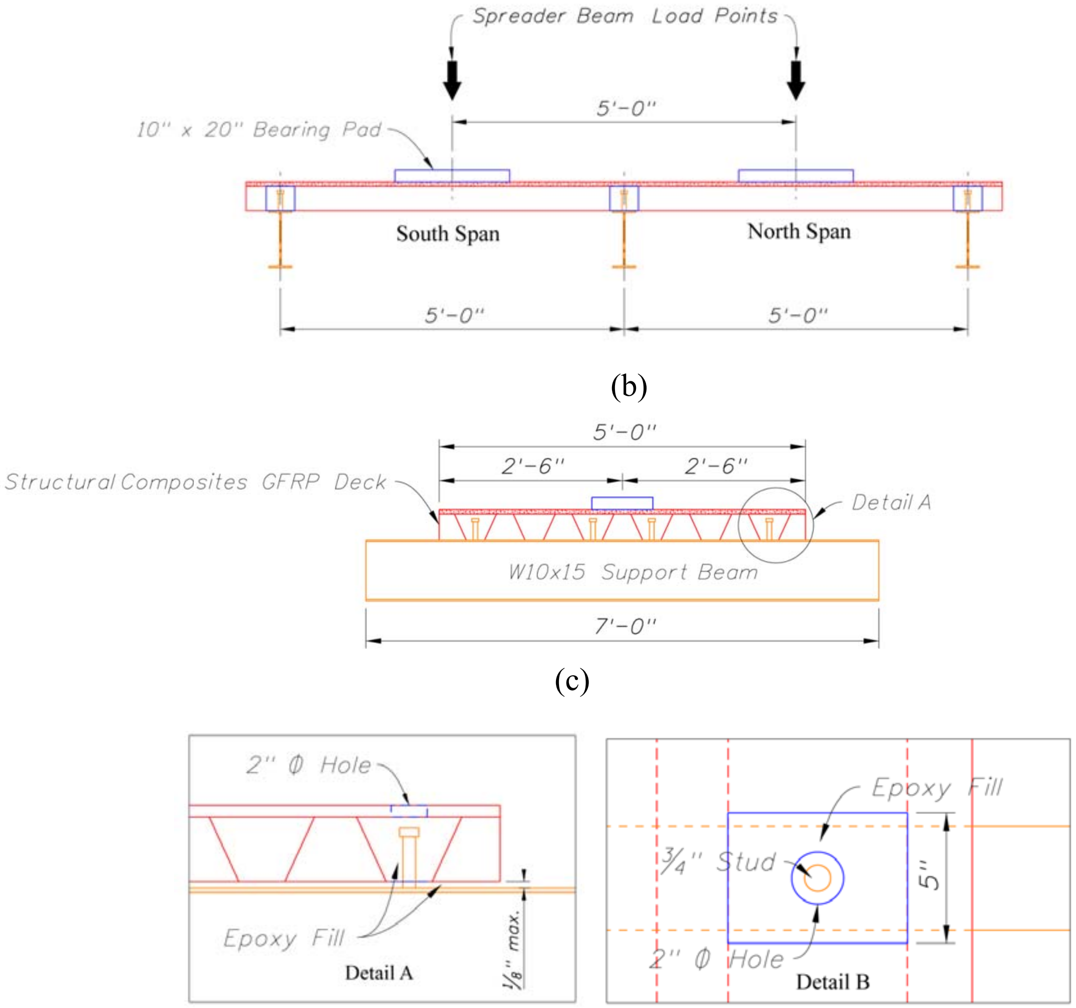

(b)

(c)

(d)

Figure 4.5 (Continued) Layout of the FRP Bridge Deck Specimen; (b) Elevation View; (c) Cross-Section; and (d) Connection Details

(a)

(b)

Figure 4.6 Test Setup: (a) Initial Static and Fatigue Tests and (b) Residual Strength Test

4.2.2 Instrumentation Plan

The instrumentation plan is shown in Figure 4.7. Surface-mounted strain gauges and displacement transducers were installed at critical locations to gather strain and deflection data. Seven strain gauges were attached to the bottom surface (tension side) of the FRP deck at each mid-span (north and south), the sections with maximum positive moments (see Figure 4.7 (b)). Three strain gauges, on the other hand, were attached to the top surface (tension side) of the FRP deck at the interior support to record the strains induced by maximum negative moments (see Figure 4.7 (c)). In addition to the strain gauges, one displacement transducer was used at the center of each steel girder (see Figure 4.7 (c) and (d)) to monitor the deflections at the supports, while the deflections at each mid-span (north and south) were monitored using three displacement transducers (see Figure 4.7 (b)).

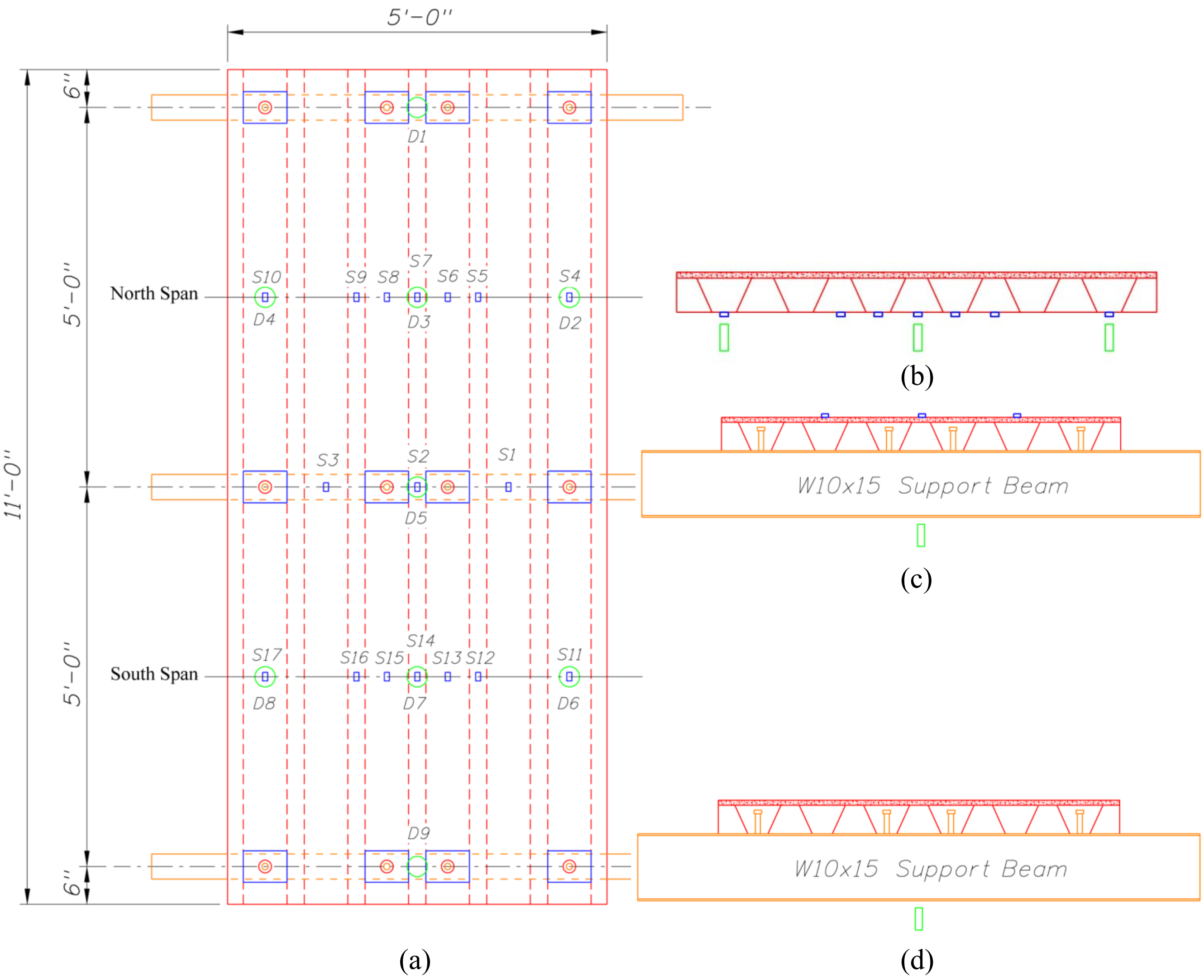

Figure 4.7 Instrumentation Plan: (a) Plan View; (b) Mid-Span; (c) Interior Support; and (d) Exterior Support

4.2.3 Initial Static Test

Before the application of fatigue loading, the FRP bridge deck was subjected to static load up to service limit, and then unloaded. The target service load was calculated as 42 kip based on an HS 20 single axle load (32 kip) and the impact factor of 1.33, as suggested by AASHTO LRFD Highway Bridge Design Specifications (2005). Accordingly, each span was loaded simultaneously up to 21 kip. The serviceability of the FRP bridge deck system, including its stiffness and deflection, was investigated through this static test. The loading of the specimen was performed at a constant rate of 0.25 kip/sec. Figures 4.8, 4.9, and 4.10 show the load-deflection responses at the north mid-span, south mid-span, and interior support, respectively. Linear responses were observed at all critical locations, which is attributed to the linear elastic behavior of FRP materials. The maximum deflections at service load were seen at the centers of the north and south mid-spans with the values of 0.17 in. (L/350, where L is the span length) and 0.18 in. (L/330), respectively. These maximum deflections are considerably higher than the deflection limit of L/1,200 recommended by AASHTO LRFD 9.5.2 (2005). The low elastic modulus of GFRP could be the main reason of the high deflection of the FRP bridge deck system. The higher deflection often leads to a mismatch of the stiffness between the deck and the girder, and whether or not the design is based on a composite action, the accompanying vibration could expedite the deterioration of the superstructure. Therefore, it may be more appropriate to enhance the stiffness of the FRP deck through hybridizing it with more bulky and stiff materials, e.g., UHPC.

The tensile strains at the sections with maximum moments are shown in Figures 4.111, 4.12, and 4.13. As seen in the figures, the maximum tensile strain was recorded at the center of the interior support (negative moment) which was 0.00102. At service load, the maximum tensile strains at the north and south mid-spans were 0.000967 and 0.00101, respectively. At the end of the initial static test, a crack was observed within the polymer concrete overlay along the interior support. The crack however did not propagate into the FRP deck system; therefore, the structural performance of the bridge deck specimen was not affected by this crack.

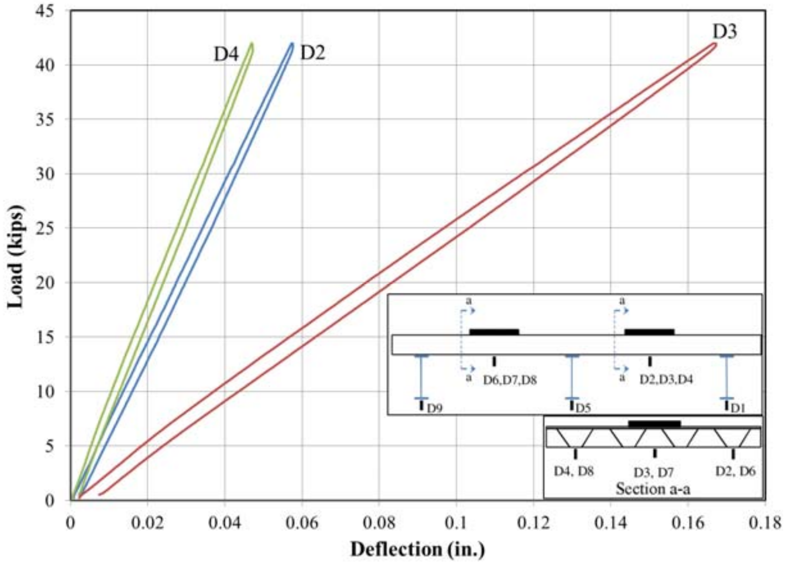

Figure 4.8 Load-Deflection Response at the North Mid-Span

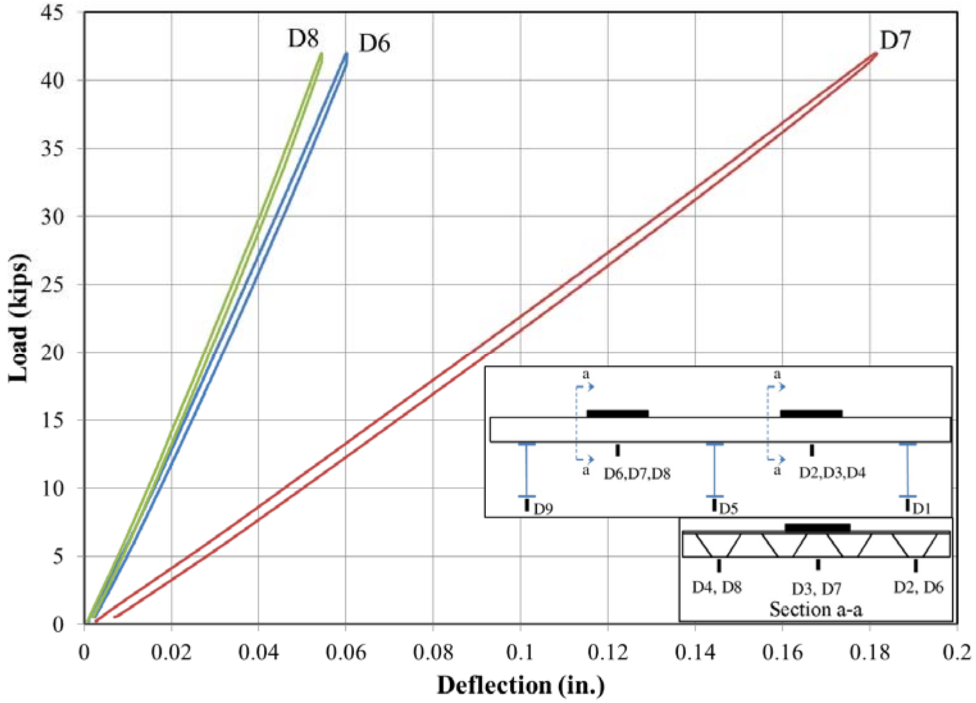

Figure 4.9 Load-Deflection Response at the South Mid-Span

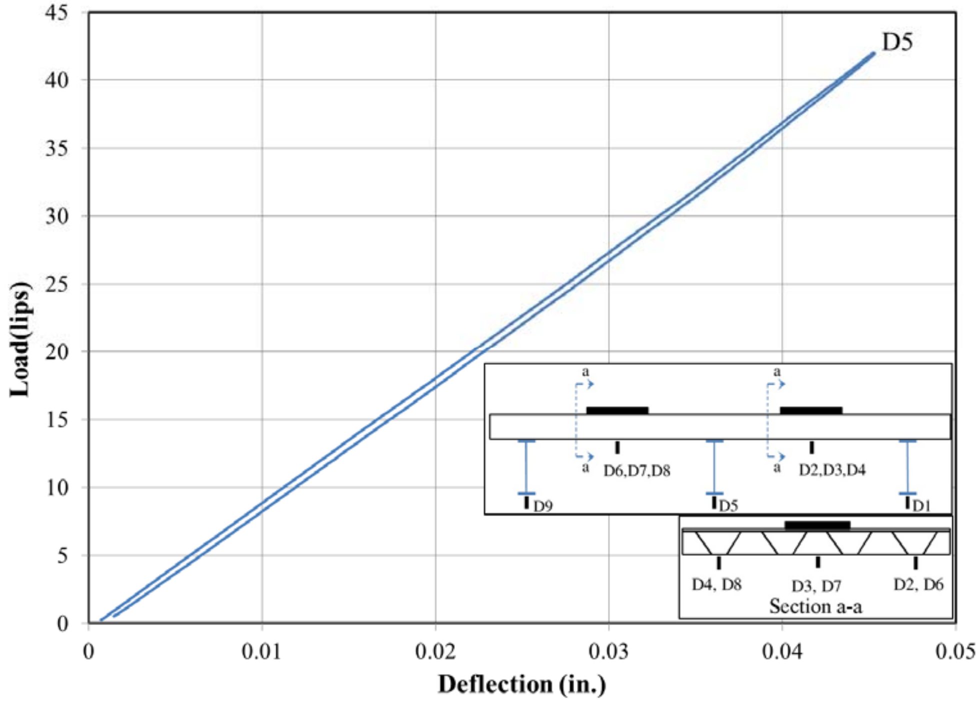

Figure 4.10 Load-Deflection Response at the Interior Support

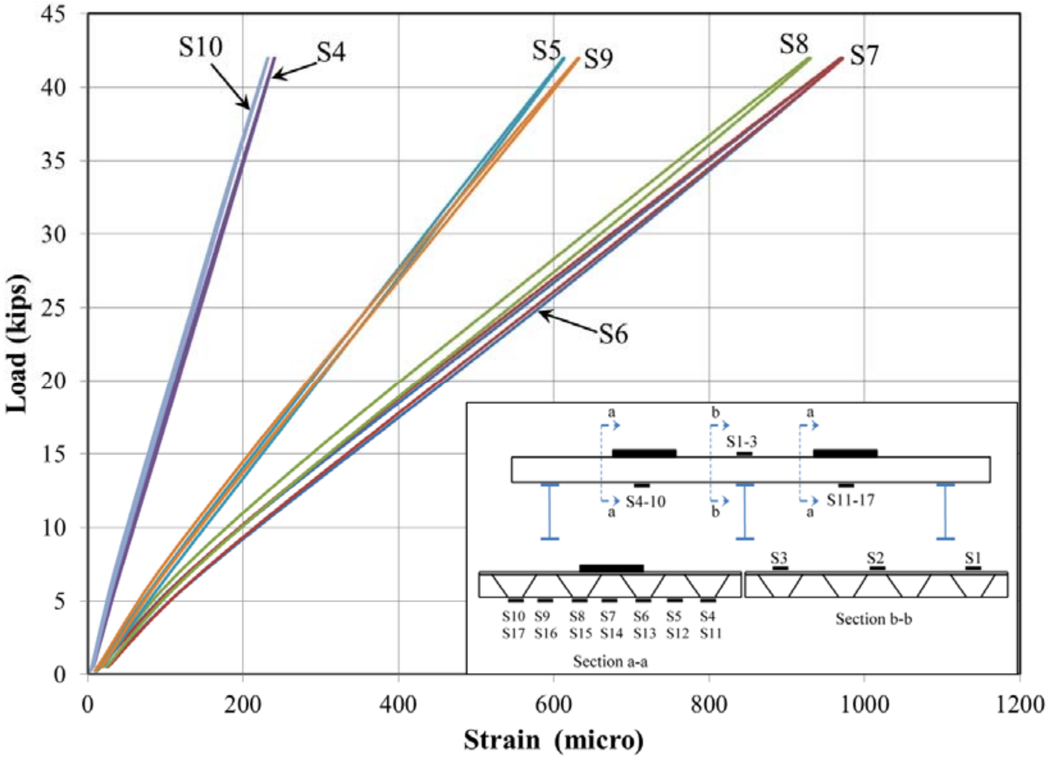

Figure 4.11 Tensile Strain at the North Mid-Span

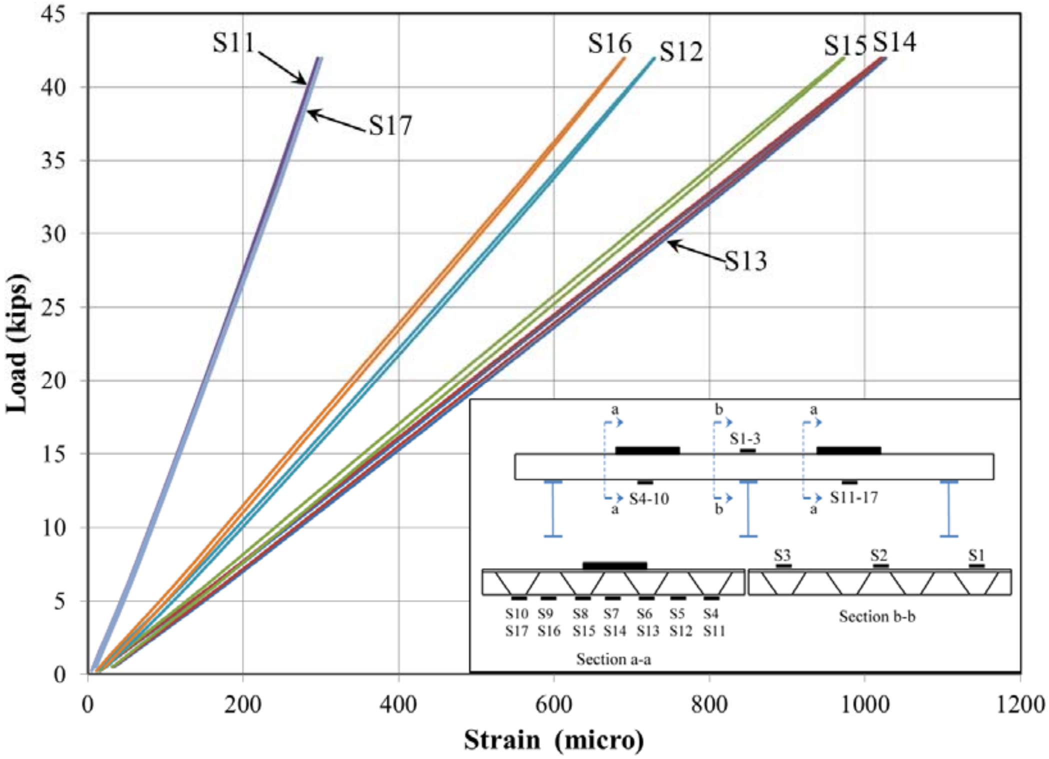

Figure 4.12 Tensile Strain at the South Mid-Span

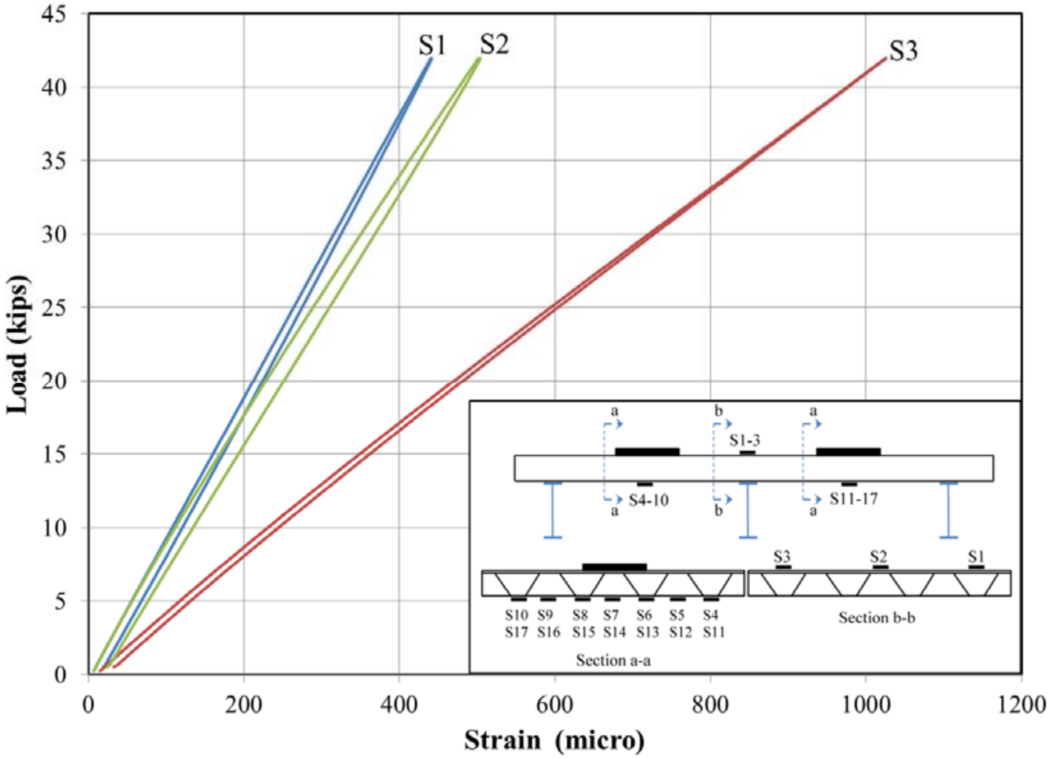

Figure 4.13 Tensile Strain at the Interior Support

4.2.4 Fatigue Test

The FRP bridge deck was subjected to two million cycles of design truck single axle sinusoidal load in the range of 1.5 – 21 kip in each span at a frequency of 4 Hz. The lower limit of 1.5 kip was set to prevent the pads from "walking" (Vyas et al. 2009). Load, displacement, and strain data were recorded for two seconds after every 1,000 cycles up to 1,500,000 cycles, and at 2 million cycles. Figure 4.14 shows the fatigue deflection responses at the north mid-span, south mid-span, and interior support. As shown in the figure, no significant change was seen in the deflections throughout the fatigue test, implying that the FRP bridge deck system withstood the fatigue loading with no sign of damage or failure. Similar to the initial static test, the maximum deflections were seen at the centers of the north (D3) and south (D7) mid-spans. The highest deflections in D3 and D7 at the end of the fatigue test were 0.18 in. and 0.21 in., respectively. These values as well as the deflections at other critical locations are very similar to their counterparts measured in the initial static test.

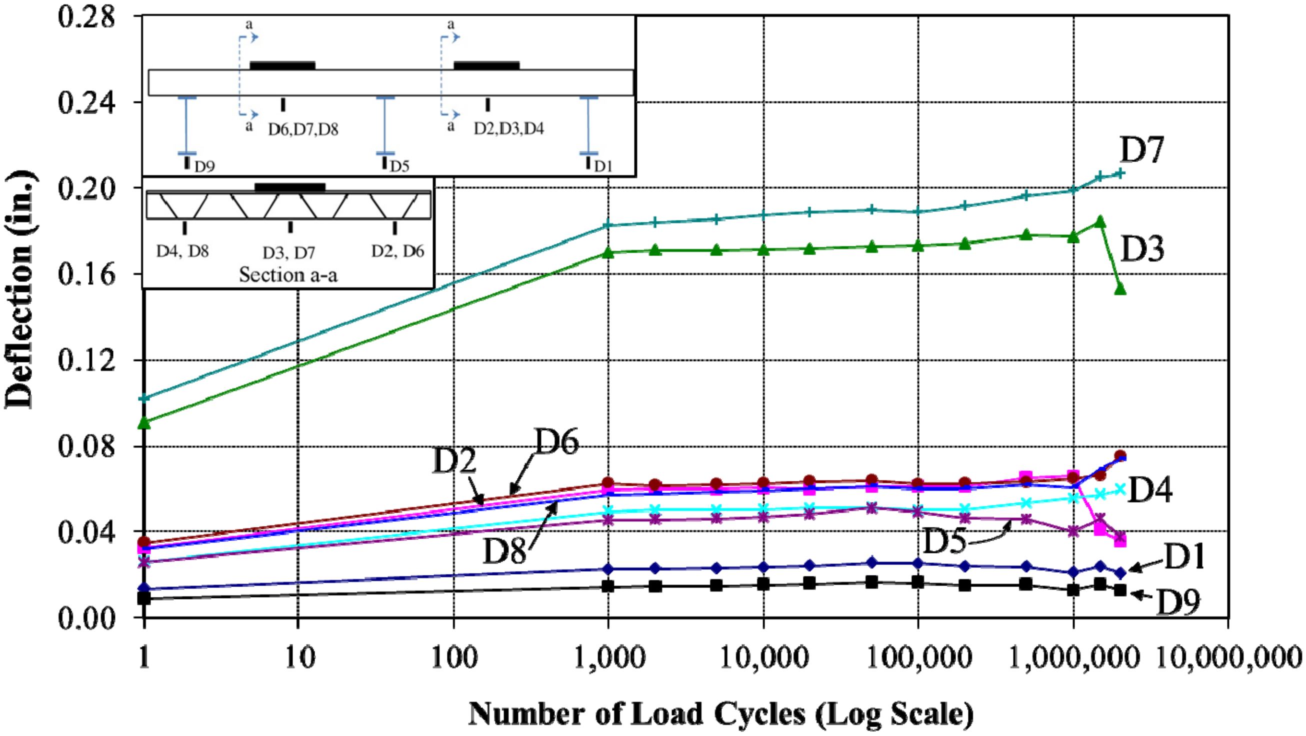

Figure 4.14 Fatigue Deflection Responses

Figures 4.15 and 4.16 show the fatigue strain responses at the north mid-span and south mid-span, respectively. Since the strain gauges at the interior support were damaged during the initial static test due to the cracking in the polymer concrete overlay, the strains at this section could not be recorded. Similar to the measured deflections, no significant change was observed in the strain responses during the fatigue test. The maximum tensile strains measured at the center of the north and south mid-spans were 0.00110 and 0.00111, respectively. Generally, the strains measured at critical sections during the fatigue test were similar to those measured during the initial static test. This also confirms that the FRP bridge deck system showed no sign of damage or failure during the fatigue loading.

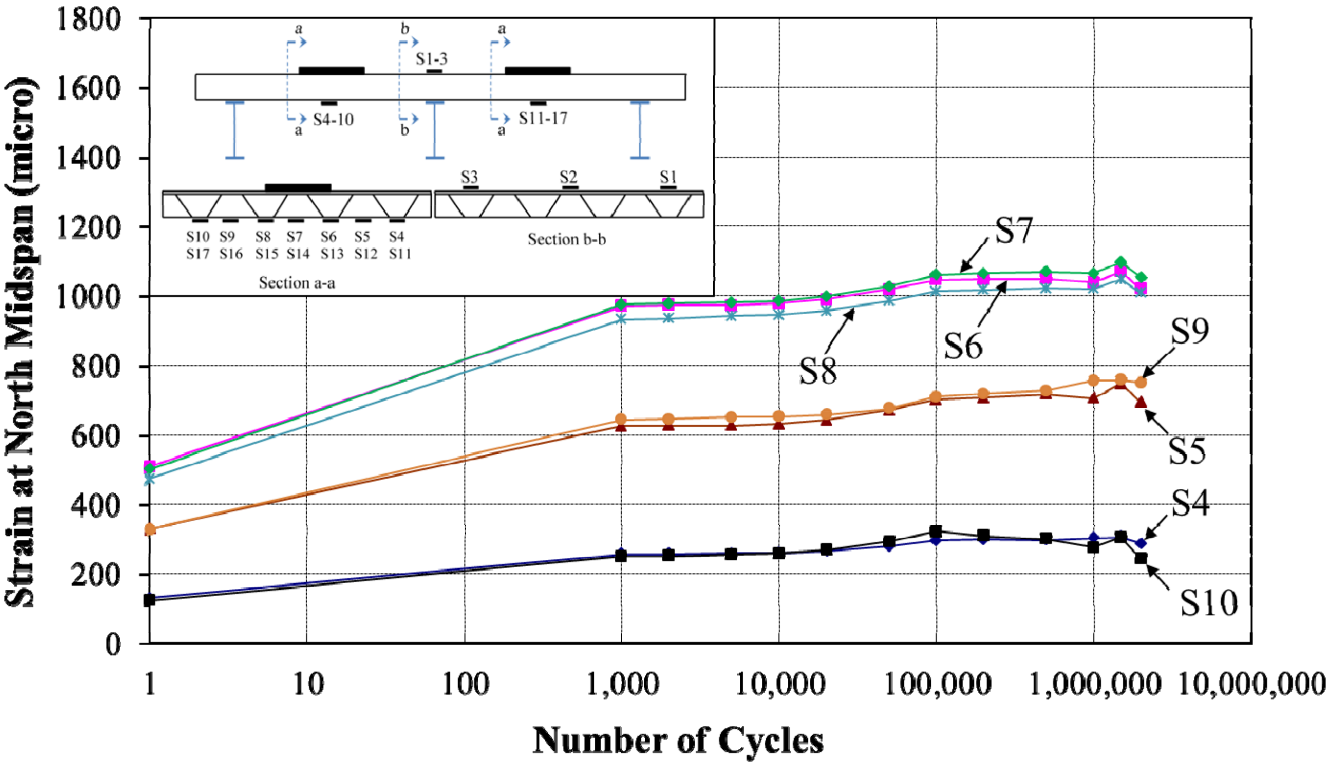

Figure 4.15 Fatigue Strain Responses at the North Mid-Span

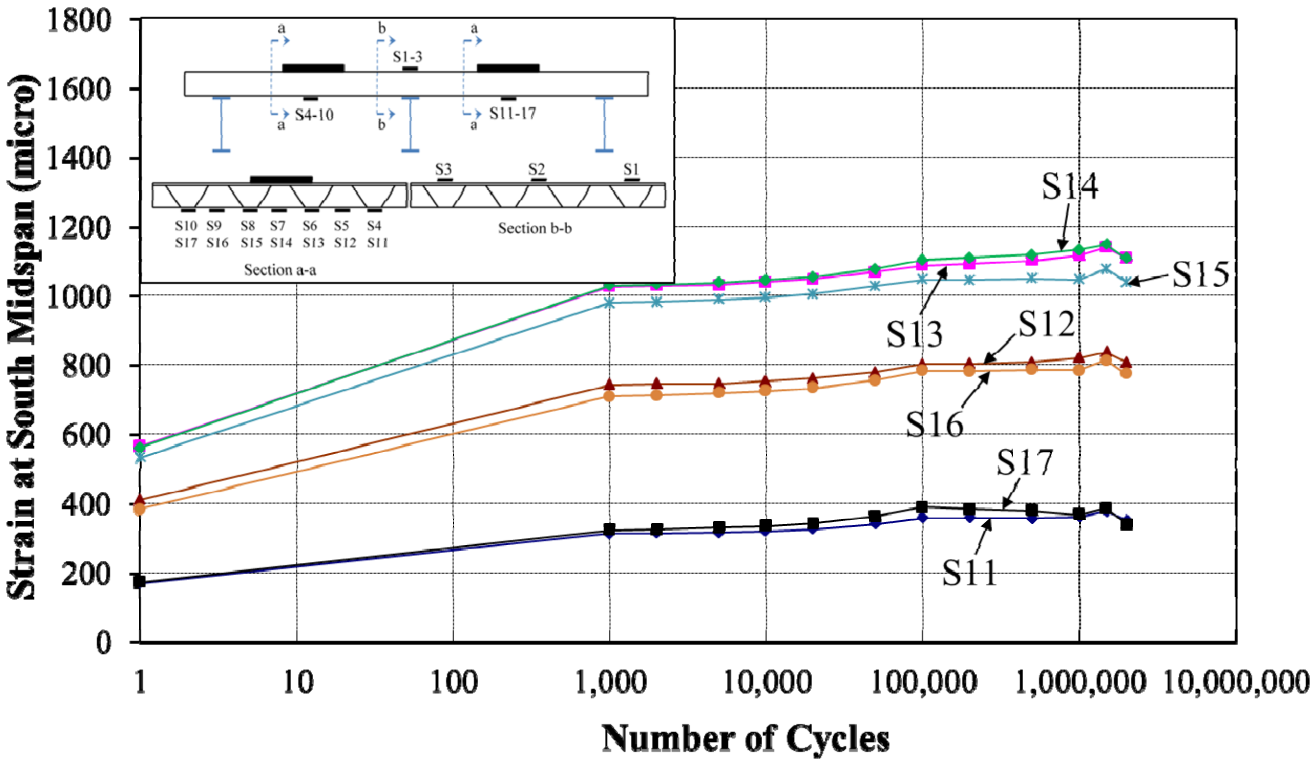

Figure 4.16 Fatigue Strain Responses at the South Mid-Span

4.2.5 Residual Strength Test

After the fatigue test, the FRP bridge deck was subjected to static load up to failure. The deck specimen was loaded at the south mid-span (see Figure 4.6 (b)) at a constant rate of 0.25 kip/sec. The test was terminated after a significant load drop and acoustic noise. Further examination showed that the overlay portion failed by delamination (debonding oval pattern) which is shown in Figure 4.17. Figures 4.18 and 4.19 show the load-deflection responses at the south mid-span (where the load applied) and interior support, respectively. The deflection in D6 is not presented since the displacement transducers attached at this location was not working properly during this test. The FRP bridge deck failed at a load of 123 kip, which is three times the design ultimate load of 37.24 kip (including the load factor as well as the impact factor). Linear deflection responses are associated with the elastic behavior of FRP materials. At the ultimate load, the deflection in D7 (the south mid-span) was 1.1 in. The tensile strains at the south mid-span are shown in Figure 4.20. Strains in S1, S2, and S3 could not be measured due to wearing surface cracks, and other strain gauges which are shown in Figure 4.20 debonded before reaching the ultimate load. The maximum tensile strain was measured as 0.009 in S14.

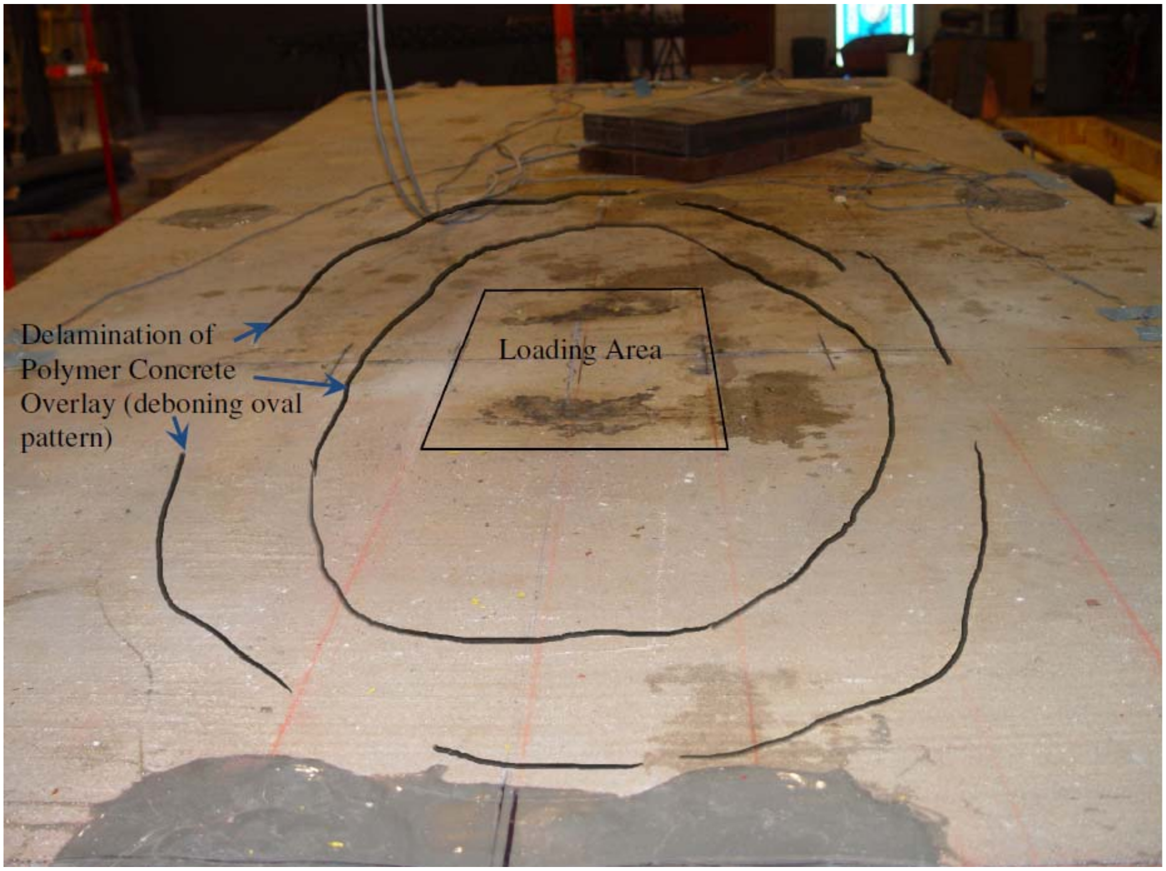

Figure 4.17 Oval Pattern of Polymer Concrete Overlay Delamination

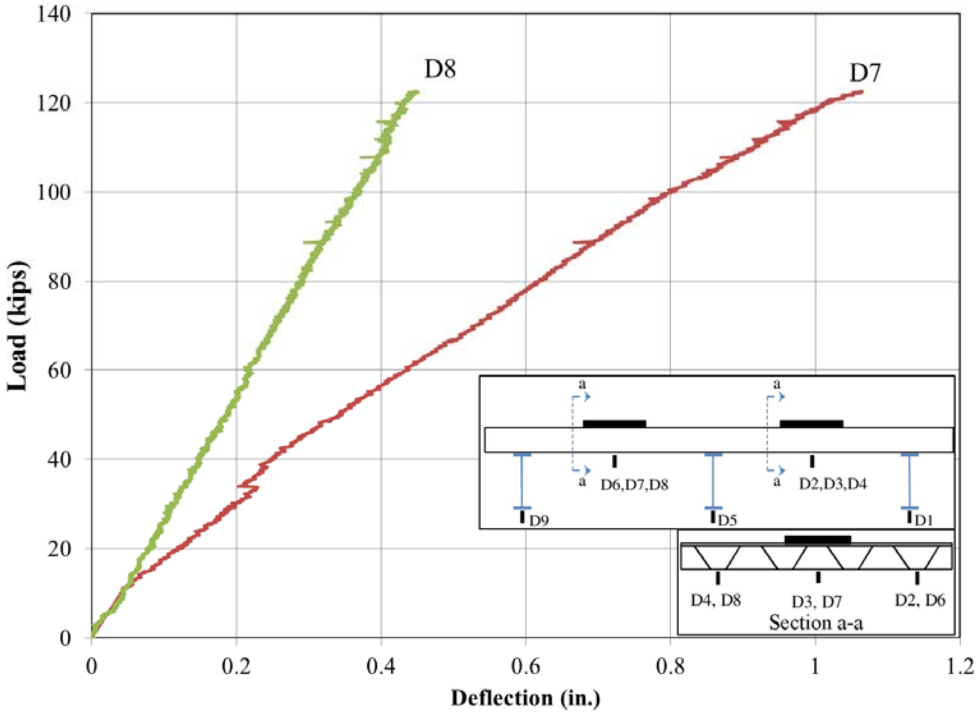

Figure 4.18 Load-Deflection Response at the South Mid-Span

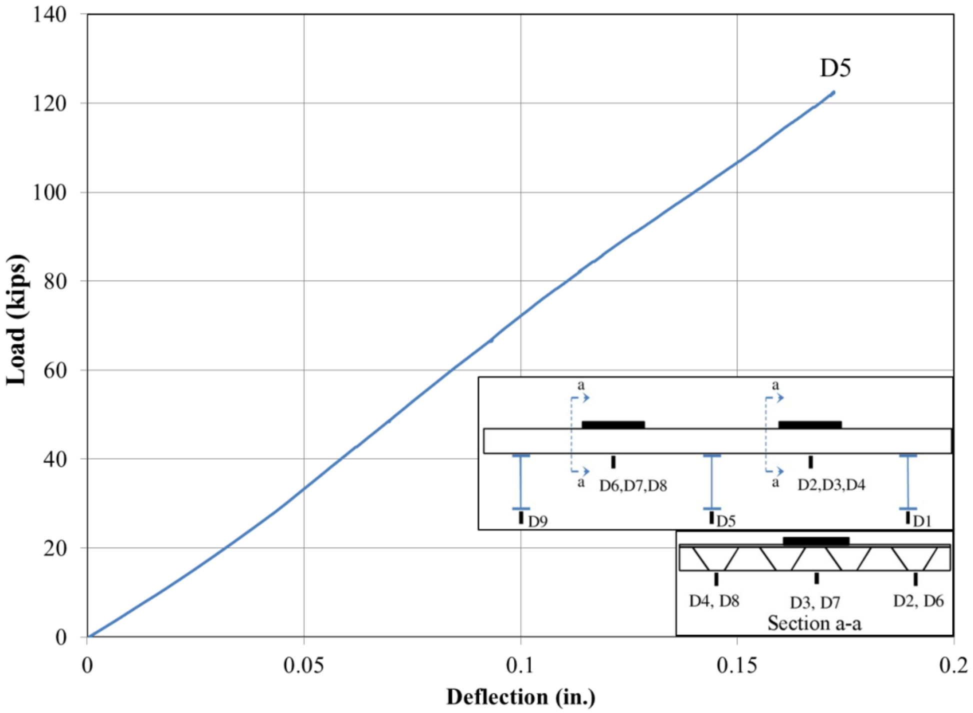

Figure 4.19 Load-Deflection Response at the Interior Support

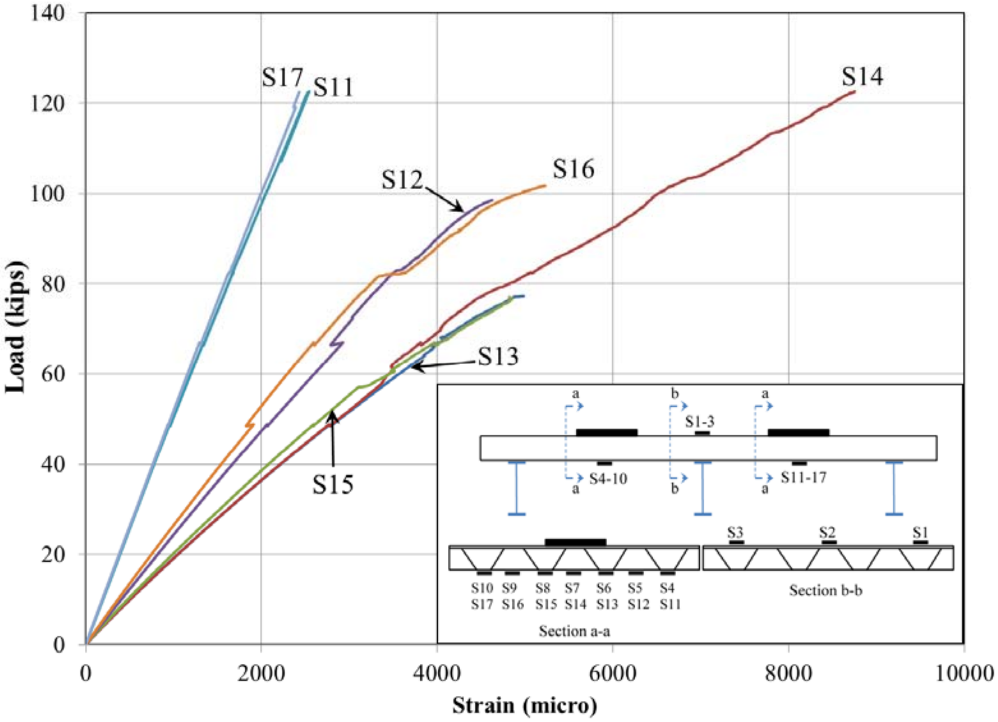

Figure 4.20 Tensile Strain at the South Mid-Span

4.3 Conclusions

In this part of the project, an FRP deck product made by Structural Composites Inc. of Melbourne, FL, was tested under static and fatigue loading. The following conclusions could be drawn from this study.

1. The FRP bridge deck showed linear deflection and strain responses under static loading, which is attributed to the linear elastic behavior of FRP materials.
2. The maximum deflections at service load were 0.17 in. (L/350) at the north mid-span and 0.18 in. (L/330) at the south mid-span. These maximum deflections are considerably higher than the deflection limit of L/1,200 recommended by AASHTO LRFD 9.5.2 (2005), which may be due to the low elastic modulus of GFRP.
3. The FRP bridge deck withstood two million cycles of AASHTO-specified fatigue loading with no sign of damage or failure, and the maximum fatigue deflections and strains remained similar to those measured during the initial static test.
4. The FRP deck showed residual strengths of at least three times the target design load.

The FRP bridge deck was studied under static and fatigue tests, and the results satisfy the AASHTO LRFD loading requirements. However, the deflection of the deck system under service load significantly exceeded the deflection limit suggested by AASHTO LRFD which necessitates the need to enhance the stiffness of the system, perhaps by adding a UHPC overlay on top of the GFRP system. The higher elastic modulus of UHPC (more than three times that of FRP), could potentially increase the stiffness of the deck significantly more than by increasing the thickness of FRP. Also, the UHPC overly could act as a wearing surface, which in turn would eliminate the debonding issues associated with the polymer concrete overlay. The panel to panel connections or mechanism is another issue in this bridge deck system which needs to be investigated.

Chapter-5

Summary and Conclusions

Two deck systems; the UHPC deck and an FRP deck, were studied in this research. Experiments were carried out at both the component and system levels to evaluate the connections, lateral load distribution, and fatigue and residual strength in the UHPC deck system. The development length of HSS rebars in UHPC was also experimentally estimated. Dowel action of longitudinal steel reinforcement in UHPC and uniaxial fatigue behavior of UHPC were further investigated through experimental and analytical studies. Finally, an FRP deck system was studied under static and fatigue loading. These experimental and analytical studies led to the following conclusions and recommendations.

5.1 UHPC Deck

- The deck-to-girder and the deck-to-deck connections both proved to be adequate for the loading conditions expected from the HS20 truck and wind forces.

- Tests for the live load distribution showed that most of the load is taken by the ribs under or immediately next to the load. The rib under the load, on average, takes 34% of the service load. This share increases with the load.

- The share of load calculated for ribs based on deflection is however approximate, especially in the nonlinear range and only provides an estimate about how the ribs share the load.

- The deck panels and connections successfully endured two million cycles of repeated loading and had a residual strength of 47% and 94% higher than the AASHTO (2005) factored load requirement.

- In the residual strength test, the deck system exhibited significant deflection beyond the peak load indicating substantial ductility and warning before failure.

- Differential deflection across the tongue and groove connection during the deck-to-deck connection test demonstrated the need for using epoxy grout at the tongue and groove joint. It is recommended to either use epoxy or have a match cast connection in the real bridge deck.

- Development length for #3 rebars embedded in UHPC was found as 12db, based on the pullout tests, and for #7 rebars as 18db, based on the beam tests. These values should be considered as an estimate and may require further verification.

- Development lengths calculated based on the equations provided by the ACI 408R-03 agree reasonably well with the values suggested by the present study. On the other hand, ACI 318-08 overestimated the development length for HSS rebars embedded in UHPC.

While the proposed system shows great promise, further studies are needed to optimize the design by decreasing the weight of the deck from its current 25 lb/ft^2 based on the lateral distribution of live load, assess the effectiveness of the UHPC as wearing surface, and field monitoring of the deck under ambient traffic and designated truck loading. It is also recommended to perform a set of pullout and beam tests with other rebar sizes and cover thicknesses to develop a database, which could then be used to propose an equation for calculating development length for HSS rebars embedded in UHPC. This database could also be used to propose modifications to the prevailing codes and specifications. Traditionally performed beam tests with spliced rebars may also provide helpful data for this purpose.

5.2 Dowel Action of Longitudinal Steel Reinforcement in UHPC and Uniaxial Fatigue Behavior of UHPC

- Dowel action contributes considerably to shear resistance that should not be ignored when applied to reinforced UHPC structures without web reinforcement. Parameters such as bottom cover thickness, side cover thickness, dowel bar size as well as the beam length also influence the dowel action performance.

- It can be concluded that the BEF theory is applicable to investigation of dowel action against UHPC cover, particularly in the initial elastic portion of the responses. Moreover, the BEF sub-grade moduli were calibrated based on the data obtained from the experiments.

- Most of the specimens tested under uniaxial fatigue loading showed tensile cracks earlier than expected due to the difficulty in controlling the load eccentricity. However, a well-balanced specimen was able to achieve 2.5e6 cycles without failure. After a monotonic strength test, it was estimated to have lost only approximately 20% of its static capacity. Using the variable amplitude strain data and assumptions regarding the form of the stain-life curve, it was possible to predict the material constants governing the Coffin-Manson relation for UHPC.

Although the dowel action proved to be an effective factor in the shear resistance of UHPC structures, additional testing is needed for developing an empirical expression taking into account this factor. To better capture the peak loading and behavior of the fibers bridging the cracks, a beam on nonlinear foundation model is needed. Once the concrete subgrade modulus calibrated, it can be used for simulation purposes in a FEM model, which can provide guidance on optimal design based on the observed shear failure mode of the UHPC-HSS specimens.

5.3 FRP Bridge Deck

- The FRP bridge deck showed linear deflection and strain responses under static loading, which is attributed to the linear elastic behavior of FRP materials.

- The maximum deflections at service load were 0.17 in. (L/350) at the north mid-span and 0.18 in. (L/330) at the south mid-span. These maximum deflections are considerably higher than the deflection limit of L/800 recommended by AASHTO LRFD (2005), which may be due to the low elastic modulus of GFRP.

- The FRP bridge deck withstood two million cycles of AASHTO-specified fatigue loading with no sign of damage or failure, and the maximum fatigue deflections and strains remained similar to those measured during the initial static test.

- The FRP deck system showed residual strengths of at least three times the target design load.

Although the FRP bridge deck system satisfied the AASHTO LRFD loading requirements, its deflection under service load significantly exceeded the deflection limit suggested by AASHTO LRFD. Therefore, it seems necessary to enhance the stiffness of the deck structure, perhaps by adding a UHPC overlay on top of the GFRP system. The higher elastic modulus of UHPC (more than three times that of FRP), could potentially increase the stiffness of the deck significantly more than by increasing the thickness of FRP. The UHPC overly could also act as a wearing surface eliminating the debonding issues associated with the polymer concrete overlay.

References

AASHTO LRFD Bridge Design Specifications, American Association of State Highway and Transportation Officials, Washington, D.C., 2005.

ACI 318-08, *Building Code Requirements for Structural Concrete*, American Concrete Institute, Farmington Hills, MI., 2008.

ACI 408-R03, *Bond and Development of Straight Reinforcing Bars in Tension*, American Concrete Institute, Farmington Hills, MI., 2003.

Alagusundaramoorthy, P., Harik, I.E., and Choo, C.C., "Structural Behavior of FRP Composite Bridge Deck Panels." *Journal of Bridge Engineering*, ASCE, Volume 11, Issue 4, 2006, pp. 384 – 393.

Alnahhal, W.I., Chiewanichakorn, M., Aref, A.J., and Alampalli, S. "Temporal Thermal Behavior and Damage Simulations of FRP Deck." *Journal of Bridge Engineering*, ASCE, Volume 11, Issue 4, 2006, pp. 452 – 464.

Azizinamini, A., Chisala, M., and Ghosh, S.K., "Tension Development Length of Reinforcing Bars Embedded in High-Strength Concrete." *Engineering Structures*, Volume 17, Issue 7, 1995, pp. 512 – 522.

Azizinamini, A., Stark, M., Roller, J.J., and Ghosh, S.K., "Bond Performance of Reinforcing Bars Embedded in High-Strength Concrete." *Structural Journal*, ACI, Volume 90, Issue 5, 1993, pp. 554 – 561.

Bakis, C.E., Bank, L.C., Brown, V.L., Cosenza, E., Davalos, J.F., Lesko, J.J., Machida, A., Rizkalla, S.H., and Triantafillou, T.C., "Fiber Reinforced Polymer Composites for Construction—State-of-the-Art Review." *Journal of Composites for Construction*, ASCE, Volume 6, Issue 2, 2001, pp. 73 – 187.

Behloul, M., Chanvillard, G., Pimienta, P., Pineaud, A. and Rivillonet, P., "Fatigue flexural behavior of pre-cracked specimens of special UHPFRC." *Special Publication*, Volume 228, 2005, pp. 1253 – 1268.

Blais, P.Y., and M. Couture, "Precast, Prestressed Pedestrian Bridge-World's First Reactive Powder Concrete Structure." *PCI Journal*, September-October 1999, pp. 60 – 71.

Carpinteri, A., Chiaia, B. and Ferro, G., "Size effect on nominal strength of concrete structures: Multifractality of material ligaments and dimensional transition from order to disorder." *Journal of Materials and Structures*, Volume 28, Issue 6, 1995, pp. 311 – 317.

Cole, T.A., Lopez, M., and Ziehl, P.H. "Fatigue Behavior and Nondestructive Evaluation of Full-Scale FRP Honeycomb Bridge Specimen." *Journal of Bridge Engineering*, ASCE, Volume 11, Issue 4, 2006, pp. 420 – 429.

Cornelissen, H. A. W., "Fatigue Failure of Concrete in Tension." Heron, Volume 29, Issue 4, 1984, pp. 68.

Darwin, D., Zuo, J., Tholen, M.L., and Idun, E.K., "Development Length Criteria for Conventional and High Relative Rib Area Reinforcing Bars." *Structural Journal*, ACI, Volume 93, Issue 3, 1996, pp. 347 – 359.

Davalos, J.F., and Chen, A., "Buckling Behavior of Honeycomb FRP Core with Partially Restrained Loaded Edges under Out-Of-Plane Compression." *Journal of Composite Materials*, ASCE, Volume 39, Issue 6, 2005, pp. 1465 – 1485.

Davalos, J.F., Chen, A., and Zou, B., “Stiffness and Strength Evaluations of a New Shear Connection System for FRP Bridge Decks to Steel Girders.” *Journal of Composites for Construction*, ASCE, Volume 15, Issue 3, 2011, pp. 441 – 450.

Davalos, J.F., Qiao, P., Xu, X.F., Robinson, J., and Barth, K.E., “Modeling and Characterization of Fiber-Reinforced Plastic Honeycomb Sandwich Panels for Highway Bridge Applications.” *Journal of Composites for Construction*, ASCE, Volume 52, Issues 3 – 4, 2001, pp. 441 – 452.

Ehlen, M.A., “Life-Cycle Costs of Fiber-Reinforced-Polymer Bridge Decks.” *Journal of Materials in Civil Engineering*, ASCE, Volume 11, Issue 3, 1999, pp. 224 – 230.

El-Ariss, B., “Behavior of Beams with Dowel Action.” Engineering Structures, Elsevier, Volume 29, Issue 6, 2007, pp. 899–903.

Fitik, B., Niedermeier, R., and Zilch, K., “Fatigue Behavior of Ultra High-Performance Concrete Under Cyclic Stress Reversal Loading.” Second International Symposium on Ultra High Performance Concrete, 2008. pp. 529-536.

Gao, L., and Hsu, D. T., “Fatigue of concrete under uniaxial compression cyclic loading.” *ACI Materials Journal*, Volume 95, Issue 5, 1998, pp. 575 – 581.

Graybeal, B. A., “Structural Behavior of Ultra-High Performance Concrete Prestressed I-Girders.” *Final Report*, Federal Highway Administration, McLean, VA., 2006, pp. 1, 90.

Graybeal, B. A., “Compressive Behavior of Ultra-High-Performance Fiber-Reinforced Concrete.” *ACI Materials Journal*, Volume 104, Issue 2, 2007a, pp. 146 – 152.

Graybeal, B. A., “Analysis of an Ultra-High Performance Concrete Two-Way Ribbed Bridge Deck Slab.” Federal Highway Administration, Washington D.C., 2007b.

Graybeal, B. A., and Hartmann, J.L., “Strength and Durability of Ultra-High Performance Concrete.” *Proceedings of the 2003 PCI National Bridge Conference*, Orlando, FL, 2003, 20 pp.

Habel, K., Denarié, E. and Brühwiler, E., “Experimental Investigation of Composite Ultra-High-Performance Fiber-Reinforced Concrete and Conventional Concrete Members.” *ACI Structural Journal*, Volume 104, Issue 1, 2007, pp. 93 – 101.

Habel, K., Viviani, M., Denarié, E. and Brühwiler, E., “Development of the mechanical properties of an Ultra-High Performance Fiber Reinforced Concrete (UHPFRC).” *Journal of Cement and Concrete Research*, Volume 36, Issue 7, 2006, pp. 1362 – 1370.

Hajar, Z., A. Simon, D. Lecointre, and Petitjean, J., “Construction of the First Road Bridges Made of Ultra-High-Performance Concrete.” *Proceedings of 2003 International Symposium on High Performance Concrete*, Orlando, FL, 2003, 18 pp.

Hamad, B.S., and Itani, M.S., “Bond Strength of Reinforcement in High-Performance Concrete: The Role of Silica Fume, Casting Position, and Superplasticizer Dosage.” *Materials Journal*, ACI, Volume 95, Issue 5, 1998, pp. 499 – 511.

Harajli, M. H., Hamad, B.S., and Rteil, A. A., “Effect of Confinement on Bond Strength between Steel Bars and Concrete.” *Structural Journal*, ACI, Volume 101, Issue 5, 2004, pp. 595 – 603.

Harajli, M.H., “Comparison of Bond Strength of Steel Bars in Normal and High-Strength Concrete.” *Journal of Materials in Civil Engineering*, ASCE, Volume 16, Issue 4, 2004, pp. 365 – 374.

Harajli, M.H., Hamad, B.S., and Karam, K., “Bond-Slip Response of Reinforcing Bars Embedded in Plain and Fiber Concrete.” *Journal of Materials in Civil Engineering*, ASCE, Volume 14, Issue 6, 2002, pp. 503 – 511.

Harris, D. K., and Roberts-Wollmann, C. L., "Characterization of the Punching Shear Capacity of Thin Ultra-High Performance Concrete Slabs." *Final Report*, Virginia Transportation Research Council, Charlottesville, VA., 2005, pp. 57.

Hordijk, D., "Local approach to fatigue of concrete." Delft University of Technology., 1991, pp. 210.

Horii, H., Shin, H. C., and Pallewatta, T. M., "Mechanism of fatigue crack growth in concrete." *Journal of Cement Concrete Composite*, Volume 14, Issue 2, 1992, pp. 83 – 89.

Ince, R., and Arici, E., "Size effect in bearing strength of concrete cubes." *Journal of Construction and Building Materials*, Volume 18, Issue 8, 2004, pp. 603 – 609.

Ince, R., Yalcin, E., and Arslan, A., "Size-dependent response of dowel action in R.C. members." *Journal of Engineering Structures*, Volume 29, Issue 6, 2007, pp. 955 – 961.

Johnston, C. D., and Zemp, R. W., "Flexural Fatigue Performance of Steel Fiber Reinforced Concrete-Influence of fiber content, aspect ratio and type." Material Journal, ACI. Volume 88, Issue 4, 1991, pp. 347-383.

Keller, T., and Gurtler, H., "Composite Action and Adhesive Bond between Fiber-Reinforced Polymer Bridge Decks and Main Girders." *Journal of Composites for Construction*, ASCE, Volume 9, Issue 4, 2005, pp. 360–368.

Khandaker, M., and Hossain, A., "Bond Characteristics of plain and deformed bars in lightweight pumice concrete." *Journal of Construction and Building Materials*, Elsevier, Volume 22, Issue 7, 2008, pp. 1491 – 1499.

Kumar, P., Chandrashekhara, K., and Nanni, A., "Structural Performance of a FRP Bridge Deck." *Journal of Construction and Building Materials*, Elsevier, Volume 18, Issue 1, 2004, pp. 35–47.

Kwan, A.K.H., Ng, P.L., and Lam, J.Y.K., "Modeling Dowel Action of Discrete Reinforcing Bars in Cracked Concrete Structures." Proceedings of the 2nd International ISCM and the 12th International EPMESC Conference, AIP Conference Proceedings, Volume 1233, Issue 1, 2010, pp. 701-706.

Lappa, E. S., Braam, C. R., and Walraven, J. C., "Static and Fatigue Bending Test of UHPC." International Symposium on Ultra High Performance Concrete, 2004. pp. 449-458.

Lenschow, R., "Long term random dynamic loading of concrete structures." *Journal of Materials and Structures*, Volume 17, Issue 1, 1984, pp. 1 – 28.

Mertz, D.R., Chajes, M.J., Gillespie, Jr., J.W., Kukich, D.S., Sabol, S.A., Hawkins, N.M., Aquino, W., and Deen, T.B., "Application of Fiber Reinforced Polymer Composites to the Highway Infrastructure." *NCHRP Report No. 503*, Transportation Research Board, National Academy of Sciences, Washington D.C., 2003.

Mirmiran, A., Saleem, M. A., Mackie, K., Xia, J., "Alternatives to Steel Grid Decks." Final Report, Florida Dept. of Transportation, Tallahassee, FL., 2009.

Mirmiran, A., Shahawy, M., Nanni, A., and Karbhari, V., "Bonded Repair and Retrofit of Concrete Structures Using FRP Composites: Recommended Construction Specifications and Process Control Manual." *NCHRP Report 514*, Transportation Research Board, National Academy of Sciences, Washington, D.C., 2004.

Mo, Y.L., and Chan, J., "Bond and Slip of Plain Rebars in Concrete." *Journal of Materials in Civil Engineering*, ASCE, Volume 8, Issue 4, 1996, pp. 208 – 211.

Mu, B., Wu, H., Yan, A., Warnemuende, K., Fu, G., Gibson, R.F., and Kim, D., "FEA of Complex Bridge System with FRP Composite Deck." *Journal of Composite for Construction*, ASCE, Volume 10, Issue 1, 2006, pp. 79 – 86.

Naaman, A. E., and Hammoud, H., "Fatigue Characteristics of High Performance Fiber-Reinforced Concrete." Cement and Concrete Composites, Elsevier, Volume 20, Issue 5, 1998, pp. 353-363.

Federal Highway Administration (FHWA). *National Bridge Inventory*. 2008.

O'Connor, J.S., and Hooks, J.M., "U.S.A.'s Experience Using Fiber Reinforced Polymer (FRP) Composite Bridge Decks to Extend Bridge Service Life." *Technical Memorandum of Public Works Research Institute*, Volume 3920, 2003, pp. 237 – 248.

Perry, V., "A Revolutionary New Material for New Solutions." *Technical Forum Presentation*, Lafarge North America, 2003, pp. 1 – 38.

Perry, V., "Innovative Field Cast UHPC Joints for Precast Deck Panel Bridge Superstructures—CN Overhead Bridge at Rainy Lake, Ontario." *CSCE 2007 Annual General Meeting & Conference*, Canada, 2007.

Perry, V.H., and Zakariasen, D., "Overview of UHPC Technology, Materials, Properties, Markets and Manufacturing." *Proceedings of the 2003 Concrete Bridge Conference*, Orlando, FL., 2003.

Reinhardt, H.W., Cornelissen, H.A.W. and Hordijk, D.A., "Tensile tests and failure analysis of concrete." *Journal of Structural Engineering*, Volume 112, Issue 11, 1986, pp. 77.

Righman, J., Barth, K.E., and Davalos, J.F., "Development of an Efficient Connector System for Fiber Reinforced Polymer Bridge Decks to Steel Girders." *Journal of Composites for Construction*, ASCE, Volume 8, Issue 4, 2004, pp. 279–288.

RILEM Committee 36-RDL, Long Term Random Dynamic Loading of Concrete Structures, Materials and Structures, Volume 17, Issue 1, 1984. pp. 1-28.

Saito, M., "Characteristics of microcracking in concrete under static and repeated tensile loading." *Journal of Cement Concrete Res*, Volume 17, Issue 2, 1987, pp. 211 – 218.

Saleem, M. A., Mirmiran, A., Xia, J. and Mackie, K., "Ultra-High-Performance Concrete Bridge Deck Reinforced with High-Strength Steel." *ACI Structural Journal*, Volume 108, Issue 5, 2011, pp. 601 – 609.

Scott, D. W., Lai, J. S., and Zureick, A., "Creep Behavior of Fiber Reinforced Polymeric Composites: A Review of the Technical Literature." *Journal of Reinforced Plastics and Composites*, Volume 14, Issue 6, 1995, pp. 588 – 617.

Seliem, H.M., Hosny, A., Rizkalla, S., Zia, P., Briggs, M., Miller, S., Darwin, D., Browning, J., Glass, G.M., Hoyt, K., Donnelly, K., and Jirsa, J.O., "Bond Characteristics of ASTM A1035 Steel Reinforcing Bars." *Structural Journal*, ACI, Volume 106, Issue 4, 2009, pp. 530 – 539.

Sendeckyj, G. P., "Constant life diagrams—a historical review." *International Journal of Fatigue*, Volume 23, Issue 4, 2001, pp. 347 – 353.

Soroushian, P., Obaseki, K., Baiyasi, M.I., El-Sweidan, B., and Choi, K.-B., "Inelastic Cyclic Behavior of Dowel Bars." Structural Journal, ACI, 1988. Volume 85, Issue 1, 1988, pp. 23-29.

Soroushian, P., Obaseki, K., and Rojas, M. C., "Bearing Strength and Stiffness of Concrete Under Reinforcing Bars." *ACI Materials Journal*, Volume 84, Issue 3, 1987, pp. 179 – 184.

Stephens, R.I., Fatemi, A., Stephens, R.R., and Fuchs, H.O., *Metal Fatigue in Engineering*, 2nd Edition, John Wiley and sons, New-York, 2001.

Su, E., and Hsu, T. C., "Biaxial compression fatigue and discontinuity of concrete." *ACI Materials Journal*, Volume 85, Issue 3, 1988, pp. 179 – 188.

Kolluru, S.V., O'Neil, E. F., Popovics, J. S., and Shah, S. P., "Crack Propagation in Flexural Fatigue of Concrete." *Journal of Engineering Mechanics*, Volume 126, Issue 9, 2000, pp. 891 – 898.

Swamy, R.N., and Bahia, H.M., "Influence of Fiber Reinforcement on the Dowel Resistance to Shear." Structural Journal, ACI, Volume 76, Issue 2, 2011, pp. 327-356.

Takkasila, M., and Reddy, H., "Structural modification of bascule bridges for noise mitigation." *Final Report*, Florida Dept. of Transportation, Tallahassee, FL., 1996.

Tanaka, Y., and Murakoshi, J., "Reexamination of Dowel Behavior of Steel Bars Embedded in Concrete." Structural Journal, ACI, Volume 108, Issue 6, 2011, pp. 659-668.

Tastani, S.P., and Pantazopoulou, S.J., "Direct Tension Pullout Bond Test: Experimental Results." *Journal of Structural Engineering*, ASCE, Volume 136, Issue 6, 2010, pp. 731 – 743.

Toutlemonde, F., Lauvin, L., Renaud, J., Kretz, T., and Brisard, S., "Fatigue Performance of UHPFRC Ribbed Slab Applied as a Road Bridge Deck Verified According to the Eurocodes." *Proceedings of 5th International Conference on Concrete under Severe Conditions*, Tours, France, 2007, pp. 1191 – 1200.

Vyas, J. S., Zhao, L., Ansley, M. H., and Xia, J., "Characterization of a Low-Profile Fiber-Reinforced Polymer Deck System for Movable Bridges." *Journal of Bridge Engineering*, ASCE, Volume 14, Issue 1, 2009, pp. 55 – 65.

Wu, H.C., Mu, B., and Warnemuende, K., "Failure Analysis of FRP Sandwich Bus Panels by Finite Element Method." *Composites Part B: Engineering*, Elsevier, Volume 34, Issue 1, 2003, pp. 51 – 58.

Wu, Z., Mirmiran, A., and Swanson, J., "Fatigue Behavior of Prestressed Tubular Bridge Deck of Fiber-Reinforced Polymer." *Transportation Research Records No. 1892*, Design of Structures, Part 8 – Structural Fiber-Reinforced Plastics, Transportation Research Board, National Research Council, Washington, D.C., 2004, pp. 246 – 255.

Xia, J., Mackie, K. R., Saleem, M. A., and Mirmiran, A., "Shear failure analysis on ultra-high performance concrete beams reinforced with high strength steel." *Journal of Engineering Structures*, Volume 33, Issue 12, 2011, pp. 3597 – 3609.

Yin, W., and Hsu, T. C., "Fatigue behavior of steel fiber reinforced concrete in uniaxial and biaxial compression." *ACI Materials Journal*, Volume 92, Issue 1, 1995 pp. 71 – 81.

Zhang, J., Stang, H., and Li, V. C., "Experimental study on crack bridging in FRC under uniaxial fatigue tension." *Journal of Materials in Civil Engineering*, Volume 12 Issue 1, 2000, pp. 66.

Zhang, Y., Cai, C.S., Shi, X., and Wang, C., "Vehicle-Induced Dynamic Performance of FRP versus Concrete Slab Bridge." Journal of Bridge Engineering, ASCE, Volume 11, Issue 4, 2006, pp. 410 – 418.